Study of Metal Nanoparticle Catalysts for High-Performance Hydrogen Generation from Chemical Hydrides

Wang, Qiuju

(Degree)
博士（工学）

(Date of Degree)
2019-09-25

(Date of Publication)
2023-09-25

(Resource Type)
doctoral thesis

(Report Number)
甲第7604号

(URL)
https://hdl.handle.net/20.500.14094/D1007604

博　士　論　文

Study of Metal Nanoparticle Catalysts for High-Performance Hydrogen Generation from Chemical Hydrides

金属ナノ粒子触媒による化学水素化物からの高効率水素発生に関する研究

July, 2019

Graduate School of Engineering

Kobe University

WANG QIUJU

Acknowledgements

This dissertation is dedicated to all the people who have helped me until now.

The work described in the present doctoral dissertation has been carried out in the Cooperative Division (located at Kansai Centre, National Institute of Advanced Industrial Science and Technology (AIST)) at the Department of Chemical Science and Engineering, Graduate School of Engineering, Kobe University during 2015.10-2019.09.

I would like to express my deepest gratitude to Professor Qiang Xu for his powerful guidance, inspiring ideas, constructive suggestions, valuable discussions, kind consideration, and for his carefully reading of this dissertation.

I sincerely thank Professor Minoru Mizuhata, Professor Satoru Nishiyama and Professor Hideshi Maki for valuable supports and critical reading of this dissertation.

I am grateful to Ms. Hitomi Fujii, Ms. Naoko Yamawaki and other members in our group for their valuable suggestions and supports.

I thank for financial supports from MEXT, AIST and Kobe University.

Finally, I appreciate my family for their constant supports and mental encouragements.

WANG QIUJU,

July, 2019

Osaka, Japan

Abstract

Faced with the ever-increasing energy demand, fuel cell technology depending on hydrogen source attracts lots of attention. For safe and efficient hydrogen storage and distribution, hydrogen evolution from liquid-phase chemical hydrogen storage materials at mild conditions with the help of catalysts becomes popular. In this doctor dissertation, we mainly focus on the syntheses of ultrafine metal nanoparticles (MNPs) immobilized on metal–organic framework (MOF) carbons or MOF-derived MNPs for catalytic hydrogen generation. In the introduction, we introduced the advantage of liquid-phase chemical hydrogen storage materials (such as formic acid and aqueous ammonia borane) and the recent development of MNPs for catalytic hydrogen generation. Our first work successfully prepared ultrafine Pd NPs immobilized on an activated hierarchically porous carbon derived from a nitrogen containing MOF for fast dehydrogenation of formic acid. In the second work, highly active AuPd NPs were immobilized on a N-doped carbon from MOF with a phosphate (P)-mediation approach for boosting hydrogen evolution from formic acid at room temperature. In the last work, Cu decorated CoOx NPs were prepared by a direct in-situ reduction from a bimetallic MOF-74 for hydrogen evolution from aqueous ammonia borane. The main findings of this dissertation are summarized as follows:

(i) Fast Dehydrogenation of Formic Acid over Palladium Nanoparticles Immobilized in Nitrogen-Doped Hierarchically Porous Carbon

A hierarchically porous carbon was prepared from carbonization of a nitrogen-containing metal–organic framework, followed by activation under ultrasonication in

aqueous potassium hydroxide (aq KOH). The activated carbon was applied as a support for immobilizing ultrafine palladium (Pd) nanoparticles (1.1 ± 0.2 nm). As a result, the as-prepared Pd nanoparticles on N-doped porous carbon with both micro- and mesoporosity exhibit an excellent activity for the dehydrogenation of formic acid, showing a high turnover frequency (TOF, 14400 h^{-1}) at 60 °C. This activation approach of carbon opens an avenue for the syntheses of highly active supported ultrafine metal NPs for catalysis.

(ii) Phosphate-Mediated Immobilization of High-Performance AuPd Nanoparticles for Dehydrogenation of Formic Acid at Room Temperature

We fabricated highly active aurum-palladium nanoparticles (AuPd NPs) immobilized on a nitrogen (N)-doped porous carbon through a phosphate (P)-mediation approach. Dehydrogenation of formic acid (FA) is a promising route to provide clean energy instead of fossil fuels for future energy economy. Synthesis of highly active catalysts for FA dehydrogenation at room temperature has attracted lots of attention. Herein, for the first time, highly active aurum-palladium nanoparticles (AuPd NPs) immobilized on a nitrogen (N)-doped porous carbon have been fabricated through a phosphate-mediation approach. The N-doped carbon anchored with phosphate, which can be removed in the alkaline solution during the reduction process of metal ions, shows an enhanced performance of absorbing and dispersion of both Au and Pd ions, which is a key to the synthesis of highly-dispersed ultrafine AuPd NPs. The as-prepared catalyst (designated as Au_2Pd_3@(P)N-C) exhibits an extraordinarily high turnover frequency (TOF) of 5400 h^{-1} and a 100% H_2 selectivity for FA dehydrogenation at 30 °C. This phosphate-mediation approach provides a new way to fabricate highly active metal NPs for catalytic application, pushing heterogeneous

catalysts forward the practical usage in energy storage and conversion.

(iii) Copper Decorated Cobalt Oxide Nanoparticles from Bimetallic MOF-74 for Dehydrogenation of Ammonia Borane

Copper decorated cobalt oxide nanoparticles have been successfully prepared from a Cu-Co-MOF-74 by in-situ reduction during hydrogen evolution from aqueous ammonia borane. This Cu-Co-MOF-74 displays a much better catalytic activity than their monometallic MOF counterparts and even than the Cu@Co-MOF-74 prepared by a typical double solvents method. The in-situ reduction strategy of bimetallic MOF takes advantage of uniform composites distribution of MOF, avoiding the aggregation during traditional thermolysis syntheses of MOF-derived metal/metal oxides. The Cu-Co-MOF-74 shows a TOF value of 18.5 min^{-1} and a good durability for 5 cycles of hydrogen evolution of ammonia borane at 25 °C. Considering the diversification of MOFs, this strategy gives a possibility of tailoring MOFs for specific functional metal/metal oxides in area of energy storage and conversion.

In summary, this dissertation focuses on the syntheses of active ultrafine MNPs by taking advantage of MOF derivatives, whose applications in hydrogen evolution from liquid-phase chemical hydrogen storage materials are promising for future fuel cell industry. The post-functionalization of MOF-derived carbons and the direct in-situ reduction strategy of MOFs to specific metal/metal oxides mentioned in this dissertation may inspire researchers to investigate the potential of MOFs in use of energy storage and conversion.

Content

Chapter 1

Introduction

The ever increasing energy consumption and environmental concerns challenge the traditional fossil-fuels-based economy, emphasizing the urgency of finding environmental-friendly substitutes with high energy capacities and safe distribution strategies. Hydrogen is considered as an efficient energy carrier due to its high energy density of 120 kJ g^{-1} (3 times as much as petroleum) and clean consumption product (H_2O).[1] Particularly, combined with fuel cell technology, hydrogen show great potential in on-board automotive applications.[2] However, for sustainable and safe energy providing, it is necessary to search ways for safe storage and distribution of hydrogen.[3] Generally, hydrogen storage including physical and chemical storage methods.

Physical storage[4] for hydrogen generally includes 3 strategies:

(1) CGH2 compressed gaseous hydrogen (35–70 MPa at room temperature).

(2) LH2 liquid hydrogen (0.5–1 MPa, at 20 to 30 K).

(3) Cryo-adsorption on high-surface-area materials (0.2–0.5 MPa, at 80 K)

(1) and (2) are viable for on-board automotive application. Especially 70 MPa CGH2 is believed to be the most mature technology used in fuel-cell-powered cars considering the thermodynamic and engineering issues. However, to achieve vehicles for general usage (driving range of 500 km), a 3-vessel-design is demanded to integrate into a car architecture, which will compromise the passengers or cargo space. LH2 technology needs low temperature to liquefy the hydrogen which is energy consuming and the boil-off gas which cannot be avoided during an idle or parking mode of the car will be a

significant loss, making the car manufactures neglect its advantages in volumetric storage density. (3) Cryo-adsorption adsorption in high-surface-area materials such as zeolites, carbon materials, metal–organic frameworks (MOFs) and polymers with intrinsic microporosity, needs to be operated at cryogenic temperatures and/or pressure systems, and none of the current absorbents can satisfy the practical volumetric (>82 $gH_2\ L^{-1}$) and gravimetric hydrogen capacities (>90 g $H_2\ kg^{-1}$).

On the contrary, chemical hydrogen storage materials including solid-state[5] and liquid-phase[6] materials exhibit high hydrogen contents stored in the form of chemical bonds. Solid-state materials such as light metal hydrides, are faced with drawbacks like high cost, high hydrogen release temperature, inefficient hydrogen generation, different loading/unloading logistics and refueling difficulty. While liquid-phase chemical hydrogen storage materials, such as formic acid, aqueous ammonia borane and hydrazine, overcome those defects and what's better, they are compatible with existing infrastructures using for gasolines and diesel, which will save abundant budget.

1.1 Liquid-phase chemical storage materials

1.1.1 Formic acid

Formic acid (FA, HCOOH)[7] is widely studied as an efficient hydrogen carrier due to its high hydrogen content (4.4 wt%). Under ambient conditions, FA is a liquid with finite toxicity, which can both be generated from CO_2 hydrogenation and biomass process. [8] Formic acid can be decomposed with the help of catalysts in two ways:

Dehydrogenation: $HCOOH\ (l) \rightarrow H_2\ (g) + CO_2\ (g)$, $\Delta G_{298K} = -35.0\ kJ\ mol^{-1}$ (1)

Dehydration: $HCOOH\ (l) \rightarrow H_2O\ (l) + CO\ (g)$, $\Delta G_{298K} = -14.9\ kJ\ mol^{-1}$ (2)

The dehydrogenation way is favored for fuel cell application since CO released during

dehydration will poison the fuel cell catalysts. The undesirable dehydration is usually caused by high catalytic temperature and acidity, making it urgent to find active catalysts under ambient temperature with appropriate catalytic promoters.

Both homogeneous[9] and heterogeneous catalysts[10] have been widely investigated for FA dehydrogenation. Dating back to 1967, the first homogeneous catalyst—iridium phosphine complex, was studied by Coffey[11] for FA decomposition with a turnover frequency (TOF) value of 1187 h^{-1} at elevated temperature between 100 and 117 °C. Since then, various noble metal complexes, containing iridium (Ir), rhodium (Rh) and ruthenium (Ru) complexes, have been developed for FA dehydrogenation. Recently, non-noble metal complex, such as iron (Fe) complex[12] has been also extensively studied to enhance the viability of homogeneous catalysts in practical catalytic application. However, despite their high turnover number (TON), homogeneous catalysts show limited catalytic activities at ambient conditions and the difficulty of separation during catalysis, driving scientists to look for alternative heterogeneous catalysts.

1.1.2 Ammonia borane

Ammonia borane (AB, $H_3N{\bullet}BH_3$)[13] with a high hydrogen content of 19.6 wt% and a low molecular weight of 30.7 g mol^{-1}, is a promising hydrogen carrier for fuel cells. AB can be handled in stable aqueous solution and dehydrogenated with catalysts at room temperature with a considerable hydrogen generation speed.

$$H_3N{\bullet}BH_3\ (aq) + 2H_2O\ (l) \rightarrow NH_4{\bullet}BO_2\ (aq) + 3H_2\ (g)$$

In last decades, noble metal catalysts,[14] including platinum (Pt), Rh, Ru, silver (Ag) and palladium (Pd), have boosted hydrogen evolution speed. However, the high cost limits their broad utilization in industry. Recently, monometallic or alloyed NPs consisting of first-row transition metals,[15] such as ion (Fe), cobalt (Co), nickel (Ni) and

copper (Cu), attract lots of attention due to their unexpected activities for aqueous AB dehydrogenation. Abundant researches about base metal catalysts sprung since then.

1.2 Metal nanoparticle catalysts for hydrogen evolution

Metal nanoparticles (MNPs) with high surface-to-volume ratio can provide enormous active sites for catalysis reaction.[16] However, their high surface energy may lead to severe aggregation during synthesis and catalysis process, which weakens the catalytic activity and durability in a large extent. In this respect, porous materials with high surface areas and pore volumes have been introduced to provide spatial confinement preventing MNPs from overgrowth and aggregation. The porous structures can not only provide space for ship-in-bottle reaction, but also facilitate the transferring of reactants and products during catalytic process.[17] Besides, porous materials with surface functionalization, can offer strong interactions with MNPs, which may change the surface electron distribution of MNPs, and therefore accelerate catalytic reaction.[18]

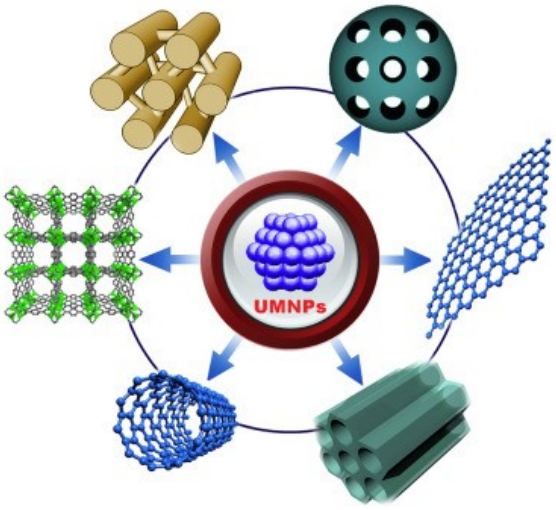

Figure 1.1 Immobilization of UMNPs to Various High-Surface-Area Materials (from Ref. 16e).

1.2 Supported metal nanoparticles

MNPs are widely used in catalytic hydrogen evolution from liquid-phase chemical hydrogen storage materials. Noble metals, such as Pd, Au, Ru and Pt in nanoscale are the most active species used for FA dehydrogenation.[19] Apart from the monometallic NPs, bimetallic NPs with surface electron redistribution, possess predominant stability and durability, and meantime can cut down the cost. AuPd[20] and AgPd[21] NPs are usually employed as catalysts for FA dehydrogenation and their activities are usually better than their monometallic counterparts.

For hydrogen evolution from aqueous AB, monometallic or alloyed NPs of noble metals such as Rh, Ru, Pt, Ag and Pd are the best choices. Recent reports about base metal NPs consisting of first-row transition metals, such as Fe, Co, Ni, and Cu, become more and more popular because of their low costs and unexpected activities for catalytic hydrogen generation from aqueous AB.

1.2.1 Support materials

Isolate MNPs with high surface energies turns to aggregate and result in a severe decline of activities. Therefore, different porous materials employed as supports have been intensively investigated and recently, metal–organic frameworks and their derivatives become a hot spot due to their special chemical and physical characteristics.

1.2.1.1 Metal–organic frameworks (MOFs)

Metal–organic frameworks (MOFs) consisting of metal ions and organic ligands, possess tunable large surface area and pore volume, have been intensively studied in last decades for energy applications. MOFs, can not only be directly used for hydrogen storage, but also employed as supports or precursors for heterogeneous catalysts used in chemical hydrogen storage.[22] MOFs have been participating in catalytic hydrogen generation as

supports since 2011. For the first time, AuPd NPs of small sizes were embedded inside the pores of ethylenedimine(ED)-MIL-101, resulting in an enhanced activity for dehydrogenation of FA.[23] Since then, lots of efforts have been made to immobilize MNPs inside pores of MOFs with controllable sizes and morphologies, such as the double solvents approach[24] and the liquid-phase concentration-controlled reduction strategy[25]. Regardless of the vulnerability of MOFs in harsh reaction conditions, they play an important role in precisely controllable syntheses of MNPs.

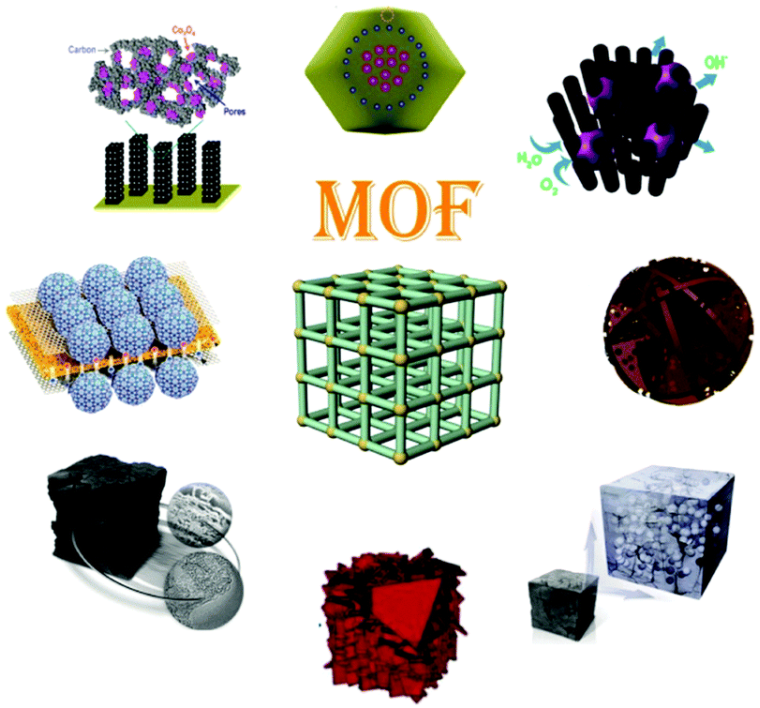

Figure 1.2. Metal–organic frameworks-based nanostructures (from Ref. 22b)

1.2.1.2 MOF-derived carbons

Even though simple thermal decomposition of organic precursors under controlled atmosphere can achieve porous carbons, the disordered and non-interconnected pore nature restrict their application in catalysis. Faced with this problem, templates including hard and soft ones have been introduced to the pyrolysis process. Unlike hard-templated method, soft-templated method can produce stable porous carbons without post removal

of template which usually includes toxic chemicals. However, the bottleneck of the soft-templated method is the limited templates. Therefore, in 2008, for the first time, our group employed MOF-5 as a sacrificial template with furfuryl alcohol (FA) as an additional carbon source for carbonization, achieving a nanoporous carbon with a very high surface area of 2872 m^2 g^{-1}.[26] Since then, various reports about MOF-derived carbons sprung up for energy storage and conversion.[27]

Considering the infinite combination of metal ions and organic ligands, MOFs present unlimited possibilities for porous carbon preparations. MOF-derived carbons can be extensively used in areas of hydrogen storage, catalysis, sensing and supercapacitors. By appropriate selection of MOFs and precise control of thermal treatment conditions, MOFs with desired properties, functions and compositions can been achieved.

Heteroatoms doping is an effective way to change the surface electronic property of carbons. Nitrogen (N), boron (B), sulphur (S) and phosphorus (P) are commonly used to modulate the surface electronic nature of carbons. In-situ doping and post doping can both realize the target while the former is preferred due to the uniform dispersion of heteroatoms in the whole carbon structure.[28] Among various heteroatom doping, N doping is the most effective strategy for catalyst syntheses since the doped N atoms can strongly cooperate with immobilized MNPs to prevent their aggregation, leading to the formation of MNPs of smaller particle size with narrow diameter distribution. On the other hand, doped N atoms also play as Lewis base sites, promoting the deprotonation of FA.[29] Fortunately, MOFs constructed with N-containing ligands, such as zeolitic imidazolate frameworks (ZIFs) and amino-MIL (Material Institute Lavoisier) series, can be used as precursors for directly pyrolysis to produce in-situ N-doped porous carbons.[30]

1.2.1.3 MOF-derived metal/metal oxides

MOFs with arrangement of metal ions as nodes and organic ligands as backbones, have tunable components. With thermolysis, different components, such as metal/metal oxides and carbon can be uniformly distributed. Porous transition metal oxides, for example, cupric oxide (CuO), cobalt oxide (Co_3O_4), iron oxide (Fe_2O_3), nickel oxide (NiO) and titanium dioxide (TiO_2) have been developed from MOFs for catalysis. Recently, bimetallic MOFs in which 2 types of metal ions share the same organic ligands become popular, which can tailor the components of metal/metal oxide for specific usage, such as $Co_3O_4/NiCo_2O_4$, CuO/Cu_2O, CuO/NiO, $Cr_2O_3@TiO_2$, and NiO/ZnO and so on.[31] Although thermolysis is the most general strategy used for metal/metal oxides preparation, the wet chemical route should also be considered since the thermolysis usually leads to aggregation and overgrowth of metal particles.

1.2.2 Syntheses of ultrafine MNPs

The ultrafine MNPs can be prepare by thermal reduction or wet chemical reduction. For recent catalytic applications, wet chemical route is preferred for its convenience, low cost, safety and simplicity. To decrease the particle sizes of MNPs, efforts have been put in enhancement of pore volume of supports, introduction of surfactants during syntheses and functionalization of MNPs or supports. Zhu et al. developed a sodium hydroxide-assisted method to prepare the uniform Pd NPs on a nanoporous carbon.[32] Song et al. introduced the diamine-functional groups on rGO to immobilize the sub-2 nm Pd NPs for FA dehydrogenation.[33] Similar reports about functionalized supports facilitating the formation of ultrafine MNPs emerged frequently in recent years.[34] The key point is the strong interaction between functional groups and metal ions which downsize MNPs.

1.3 Scope of the present work

(i) Fast Dehydrogenation of Formic Acid over Palladium Nanoparticles Immobilized in Nitrogen-Doped Hierarchically Porous Carbon

A hierarchically porous carbon was prepared from carbonization of a nitrogen-containing metal–organic framework, followed by activation under ultrasonication in aqueous potassium hydroxide (aq KOH). The activated carbon was applied as a support for immobilizing ultrafine palladium (Pd) nanoparticles (1.1 ± 0.2 nm). As a result, the as-prepared Pd nanoparticles on N-doped porous carbon with both micro- and mesoporosity exhibit an excellent activity for the dehydrogenation of formic acid, showing a high turnover frequency (TOF, 14400 h^{-1}) at 60 °C. This activation approach of carbon opens an avenue for the syntheses of highly active supported ultrafine MNPs for catalysis. This part was described in chapter 2.

(ii) Phosphate-Mediated Immobilization of High-Performance AuPd Nanoparticles for Dehydrogenation of Formic Acid at Room Temperature

For the first time, highly active aurum-palladium nanoparticles (AuPd NPs) immobilized on a nitrogen (N)-doped porous carbon has been fabricated through a phosphate-mediation approach. The N-doped carbon anchored with phosphate, which can be removed in the alkaline solution during the reduction process of metal ions, shows an enhanced performance of absorbing and dispersion of both Au and Pd ions, which is a key to the synthesis of highly-dispersed ultrafine AuPd NPs. The as-prepared catalyst (designated as Au_2Pd_3@(P)N-C) exhibits an extraordinarily high turnover frequency (TOF) of 5400 h^{-1} and a 100% H_2 selectivity for FA dehydrogenation at 30 °C. This phosphate-mediation approach provides a new way to fabricate highly active metal NPs for catalytic application, pushing heterogeneous

catalysts forward the practical usage in energy storage and conversion. This part was described in chapter 3.

(iii) Copper Decorated Cobalt Oxides Nanoparticles from Bimetallic MOF-74 for Dehydrogenation of Ammonia Borane

Copper decorated cobalt oxide nanoparticles were successfully prepared from a Cu-Co-MOF-74 by in-situ reduction during hydrogen evolution from aqueous ammonia borane. This Cu-Co-MOF-74 displays a much better catalytic activity than their monometallic MOF counterparts and even than the Cu@Co-MOF-74 prepared by a typical double solvents method. The in-situ reduction of bimetallic MOF strategy takes advantage of uniform metal distributions in MOF and meantime avoids the aggregation during traditional thermolysis synthesis of MOF-derived metal/metal oxides. The Cu-Co-MOF-74 shows a TOF value of 18.5 min^{-1} and a good durability for 5 cycles for hydrogen evolution from ammonia borane at 25 °C. Considering the diversification of MOFs, this strategy gives a possibility of tailoring MOFs for preparations of specific functional metal/metal oxides in energy storage and conversion. This part was described in chapter 4.

References

[1] a) S. Dunn, *Int. J. Hydrogen Energy* **2002**, *27*, 235; b) G. W. Crabtree, M. S. Dresselhaus, M. V. Buchanan, *Phys. Today* **2004**, *57*, 39; c) S. Satyapal, J. Petrovic, C. Read, G. Thomas, G. Ordaz, *Catal. Today* **2007**, *120*, 246; d) I. Jain, *Int. J. Hydrogen Energy* **2009**, *34*, 7368.

[2] a) D. L. Trimm, Z. I. Önsan, *Catal. Rev.* **2001**, *43*, 31; b) M. Z. Jacobson, W. Colella, D. Golden, *Science* **2005**, *308*, 1901; c) M. Momirlan, T. N. Veziroglu,

Int. J. Hydrogen Energy **2005**, *30*, 795; d) X. Cheng, Z. Shi, N. Glass, L. Zhang, J. Zhang, D. Song, Z.-S. Liu, H. Wang, J. Shen, *J. Power Sources* **2007**, *165*, 739.

[3] a) S. G. Chalk, J. F. Miller, *J. Power Sources* **2006**, *159*, 73; b) D. Ross, *Vacuum* **2006**, *80*, 1084; c) P. P. Edwards, V. L. Kuznetsov, W. I. David, N. P. Brandon, *Energy policy* **2008**, *36*, 4356; d) D. Mori, K. Hirose, *Int. J. Hydrogen Energy* **2009**, *34*, 4569.

[4] a) U. Eberle, M. Felderhoff, F. Schueth, *Angew. Chem., Int. Ed.* **2009**, *48*, 6608; b) R. K. Ahluwalia, T. Hua, J. Peng, *Int. J. Hydrogen Energy* **2012**, *37*, 2891; c) D. Durbin, C. Malardier-Jugroot, *Int. J. Hydrogen Energy* **2013**, *38*, 14595.

[5] a) G. Principi, F. Agresti, A. Maddalena, S. L. Russo, *Energy* **2009**, *34*, 2087; b) C. Weidenthaler, M. Felderhoff, *Energy Environ. Sci.* **2011**, *4*, 2495.

[6] a) H. L. Jiang, S. K. Singh, J. M. Yan, X. B. Zhang, Q. Xu, *ChemSusChem* **2010**, *3*, 541; b) M. Yadav, Q. Xu, *Energy Environ. Sci.* **2012**, *5*, 9698; c) Q.-L. Zhu, Q. Xu, *Energy Environ. Sci.***2015**, *8*, 478.

[7] a) F. Joó, *ChemSusChem* **2008**, *1*, 805; b) S. Enthaler, J. von Langermann, T. Schmidt, *Energy Environ. Sci.* **2010**, *3*, 1207; c) B. Loges, A. Boddien, F. Gärtner, H. Junge, M. Beller, *Top. Catal.* **2010**, *53*, 902; d) M. Grasemann, G. Laurenczy, *Energy Environ. Sci.* **2012**, *5*, 8171.

[8] a) D. Preti, C. Resta, S. Squarcialupi, G. Fachinetti, *Angew. Chem., Int. Ed.* **2011**, *50*, 12551; b) D. A. Bulushev, J. R. Ross, *Catal. Rev.* **2018**, *60*, 566.

[9] a) T. C. Johnson, D. J. Morris, M. Wills, *Chem. Soc. Rev.* **2010**, *39*, 81; b) P. J. Hausoul, C. Broicher, R. Vegliante, C. Goeb, R. Palkovits, *Angew. Chem., Int. Ed.* **2016**, *55*, 5597; c) D. Mellmann, P. Sponholz, H. Junge, M. Beller, *Chem. Soc. Rev.* **2016**, *45*, 3954; d) V. Henricks, I. Yuranov, N. Autissier, G. Laurenczy,

Catalysts **2017**, *7*, 348; e) K. Sordakis, C. Tang, L. K. Vogt, H. Junge, P. J. Dyson, M. Beller, G. Laurenczy, *Chem. Rev.* **2017**, *118*, 372.

[10] a) M. Ojeda, E. Iglesia, *Angew. Chem., Int. Ed.* **2009**, *48*, 4800; b) Q.-Y. Bi, X.-L. Du, Y.-M. Liu, Y. Cao, H.-Y. He, K.-N. Fan, *J. Am. Chem. Soc.* **2012**, *134*, 8926; c) Z. Li, Q. Xu, *Acc. Chem. Res.* **2017**, *50*, 1449; d) C. Tang, A. E. Surkus, F. Chen, M. M. Pohl, G. Agostini, M. Schneider, H. Junge, M. Beller, *Angew. Chem., Int. Ed.* **2017**, *56*, 16616.

[11] R. S. Coffey, *Chem. Commun. (London)* **1967**, 923b.

[12] a) A. Boddien, F. Gärtner, R. Jackstell, H. Junge, A. Spannenberg, W. Baumann, R. Ludwig, M. Beller, *Angew. Chem., Int. Ed.* **2010**, *49*, 8993; b) A. Boddien, B. r. Loges, F. Gärtner, C. Torborg, K. Fumino, H. Junge, R. Ludwig, M. Beller, *J. Am. Chem. Soc.* **2010**, *132*, 8924.

[13] a) A. Gutowska, L. Li, Y. Shin, C. M. Wang, X. S. Li, J. C. Linehan, R. S. Smith, B. D. Kay, B. Schmid, W. Shaw, *Angew. Chem., Int. Ed.* **2005**, *44*, 3578; b) A. Staubitz, A. P. Robertson, I. Manners, *Chem. Rev.* **2010**, *110*, 4079.

[14] a) P. Xi, F. Chen, G. Xie, C. Ma, H. Liu, C. Shao, J. Wang, Z. Xu, X. Xu, Z. Zeng, *Nanoscale* **2012**, *4*, 5597; b) W. Chen, J. Ji, X. Duan, G. Qian, P. Li, X. Zhou, D. Chen, W. Yuan, *Chem. Commun.* **2014**, *50*, 2142; c) J. Chen, Z.-H. Lu, Y. Wang, X. Chen, L. Zhang, *Int. J. Hydrogen Energy* **2015**, *40*, 4777; d) C. Du, Q. Ao, N. Cao, L. Yang, W. Luo, G. Cheng, *Int. J. Hydrogen Energy* **2015**, *40*, 6180; e) Q. Yao, Z.-H. Lu, Y. Jia, X. Chen, X. Liu, *Int. J. Hydrogen Energy* **2015**, *40*, 2207; f) S. Akbayrak, Y. Tonbul, S. Özkar, *Appl. Catal., B* **2016**, *198*, 162.

[15] a) J. M. Yan, X. B. Zhang, S. Han, H. Shioyama, Q. Xu, *Angew. Chem., Int. Ed.* **2008**, *47*, 2287; b) M. Kaya, M. Zahmakiran, S. Özkar, M. r. Volkan, *ACS Appl.*

Mater. Interfaces **2012**, *4*, 3866; c) P. Z. Li, A. Aijaz, Q. Xu, *Angew. Chem., Int. Ed.* **2012**, *51*, 6753; d) P.-Z. Li, K. Aranishi, Q. Xu, *Chem. Commun.* **2012**, *48*, 3173.

[16] a) R. M. Crooks, M. Zhao, L. Sun, V. Chechik, L. K. Yeung, *Acc. Chem. Res.* **2001**, *34*, 181; b) A. Moisala, A. G. Nasibulin, E. I. Kauppinen, *J. Phys.: Condens. Matter* **2003**, *15*, S3011; c) A. Cao, R. Lu, G. Veser, *Phys. Chem. Chem. Phys.* **2010**, *12*, 13499; d) B. R. Cuenya, *Thin Solid Films* **2010**, *518*, 3127; e) Q.-L. Zhu, Q. Xu, *Chem* **2016**, *1*, 220.

[17] a) K.-Y. Chan, J. Ding, J. Ren, S. Cheng, K. Y. Tsang, *J. Mater. Chem.* **2004**, *14*, 505; b) G. G. Wildgoose, C. E. Banks, R. G. Compton, *Small* **2006**, *2*, 182; c) J. M. Campelo, D. Luna, R. Luque, J. M. Marinas, A. A. Romero, *ChemSusChem* **2009**, *2*, 18.

[18] a) M. Martis, K. Mori, K. Fujiwara, W.-S. Ahn, H. Yamashita, *J. Phys. Chem. C* **2013**, *117*, 22805; b) M.-H. Jin, J.-H. Park, D. Oh, S.-W. Lee, J.-S. Park, K.-Y. Lee, D.-W. Lee, *Int. J. Hydrogen Energy* **2018**, *43*, 1451; c) J. M. Yan, S. J. Li, S. S. Yi, B. R. Wulan, W. T. Zheng, Q. Jiang, *Adv. Mater.* **2018**, *30*, 1703038.

[19] a) G. Jacobs, P. M. Patterson, U. M. Graham, A. C. Crawford, B. H. Davis, *Int. J. Hydrogen Energy* **2005**, *30*, 1265; b) D. A. Bulushev, S. Beloshapkin, J. R. Ross, *Catal. Today* **2010**, *154*, 7; c) M. Yadav, T. Akita, N. Tsumori, Q. Xu, *J. Mater. Chem.* **2012**, *22*, 12582.

[20] a) Y. Huang, X. Zhou, M. Yin, C. Liu, W. Xing, *Chem. Mater.* **2010**, *22*, 5122; b) J. M. Yan, Z. L. Wang, L. Gu, S. J. Li, H. L. Wang, W. T. Zheng, Q. Jiang, *Adv. Energy Mater.* **2015**, *5*, 1500107; c) Z. Zhang, S.-W. Cao, Y. Liao, C. Xue, *Appl. Catal., B* **2015**, *162*, 204.

[21] a) K. Mori, M. Dojo, H. Yamashita, *ACS Catal.* **2013**, *3*, 1114; b) S. Zhang, Ö. Metin, D. Su, S. Sun, *Angew. Chem., Int. Ed.* **2013**, *52*, 3681; c) Y. Jiang, X. Fan, X. Xiao, T. Qin, L. Zhang, F. Jiang, M. Li, S. Li, H. Ge, L. Chen, *J. Mater. Chem. A* **2016**, *4*, 657.

[22] a) A. Aijaz, Q. Xu, *J. Phys. Chem. Lett.* **2014**, *5*, 1400; b) W. Xia, A. Mahmood, R. Zou, Q. Xu, *Energy Environ. Sci.*, **2015**, *8*, 1837; c) G. Zhan, H. C. Zeng, *Coord. Chem. Rev.* **2016**, *320*, 181; d) L. Chen, R. Luque, Y. Li, *Chem. Soc. Rev.* **2017**, *46*, 4614.

[23] X. Gu, Z.-H. Lu, H.-L. Jiang, T. Akita, Q. Xu, *J. Am. Chem. Soc.* **2011**, *133*, 11822.

[24] A. Aijaz, A. Karkamkar, Y. J. Choi, N. Tsumori, E. Rönnebro, T. Autrey, H. Shioyama, Q. Xu, *J. Am. Chem. Soc.* **2012**, *134*, 13926.

[25] Q.-L. Zhu, J. Li, Q. Xu, *J. Am. Chem. Soc.* **2013**, *135*, 10210.

[26] B. Liu, H. Shioyama, T. Akita, Q. Xu, *J. Am. Chem. Soc.* **2008**, *130*, 5390.

[27] a) Q.-L. Zhu, Q. Xu, *Chem. Soc. Rev.* **2014**, *43*, 5468; b) J. Tang, Y. Yamauchi, *Nat. Chem.* **2016**, *8*, 638; c) H. Wang, Q.-L. Zhu, R. Zou, Q. Xu, *Chem* **2017**, *2*, 52; d) S. Dang, Q.-L. Zhu, Q. Xu, *Nat. Rev. Mater.* **2018**, *3*, 17075.

[28] a) N. Sreekanth, M. A. Nazrulla, T. V. Vineesh, K. Sailaja, K. L. Phani, *Chem. Commun.* **2015**, *51*, 16061; b) Q. Y. Bi, J. D. Lin, Y. M. Liu, H. Y. He, F. Q. Huang, Y. Cao, *Angew. Chem., Int. Ed.* **2016**, *55*, 11849; c) J. Li, Q. Tian, S. Jiang, Y. Zhang, Y. Wu, *Electrochim. Acta* **2016**, *213*, 21; d) M. Lou, R. Wang, J. Zhang, X. Tang, L. Wang, Y. Guo, D. Jia, H. Shi, L. Yang, X. Wang, *ACS Appl. Mater. Interfaces* **2019**, *11*, 6431.

[29] a) D. A. Bulushev, M. Zacharska, E. V. Shlyakhova, A. L. Chuvilin, Y. Guo, S. Beloshapkin, A. V. Okotrub, L. G. Bulusheva, *ACS Catal.* **2015**, *6*, 681; b) Z. Li,

X. Yang, N. Tsumori, Z. Liu, Y. Himeda, T. Autrey, Q. Xu, *ACS Catal.* **2017**, *7*, 2720; c) Y. Chen, X. Li, Z. Wei, S. Mao, J. Deng, Y. Cao, Y. Wang, *Catal. Commun.* **2018**, *108*, 55.

[30] a) A. J. Amali, J.-K. Sun, Q. Xu, *Chem. Commun.* **2014**, *50*, 1519; b) Q. L. Zhu, W. Xia, T. Akita, R. Zou, Q. Xu, *Adv. Mater.* **2016**, *28*, 6391.

[31] a) M. Gong, W. Zhou, M. J. Kenney, R. Kapusta, S. Cowley, Y. Wu, B. Lu, M. C. Lin, D. Y. Wang, J. Yang, *Angew. Chem., Int. Ed.* **2015**, *54*, 11989; b) G.-C. Li, P.-F. Liu, R. Liu, M. Liu, K. Tao, S.-R. Zhu, M.-K. Wu, F.-Y. Yi, L. Han, *Dalton Trans.* **2016**, *45*, 13311; c) D. Ji, H. Zhou, Y. Tong, J. Wang, M. Zhu, T. Chen, A. Yuan, *Chem. Eng. J.* **2017**, *313*, 1623; d) F. Qu, H. Jiang, M. Yang, *Mater. Lett.* **2017**, *190*, 75.

[32] Q.-L. Zhu, N. Tsumori, Q. Xu, *Chem. Sci.* **2014**, *5*, 195.

[33] F.-Z. Song, Q.-L. Zhu, N. Tsumori, Q. Xu, *ACS Catal.* **2015**, *5*, 5141.

[34] a) D. R. Dreyer, C. W. Bielawski, *Chem. Sci.* **2011**, *2*, 1233; b) S. Murugesan, K. Myers, V. R. Subramanian, *Appl. Catal., B* **2011**, *103*, 266; c) J. L. Figueiredo, *J. Mater. Chem. A* **2013**, *1*, 9351.

Chapter 2

Fast Dehydrogenation of Formic Acid over Palladium Nanoparticles Immobilized in Nitrogen-Doped Hierarchically Porous Carbon

In this work, a hierarchically porous carbon was prepared from carbonization of a nitrogen-containing metal–organic framework, followed by activation under ultrasonication in aqueous potassium hydroxide (aq KOH). The activated carbon was applied as a support for immobilizing ultrafine palladium (Pd) nanoparticles (1.1 ± 0.2 nm). As a result, the as-prepared Pd nanoparticles on N-doped porous carbon with both micro- and mesoporosity exhibit an excellent activity for the dehydrogenation of formic acid, showing a high turnover frequency (TOF, 14400 h^{-1}) at 60 °C. This activation approach of carbon opens an avenue for the syntheses of highly active supported ultrafine metal NPs for catalysis.

2.1 Introduction

Metal nanoparticles (MNPs) with a high surface to volume ratio offering abundant available active sites have been used widely as heterogeneous catalysts in hydrogenation, oxidation, and coupling reactions. However, MNPs are thermodynamically unstable because of their high surface energy, which may lead to an aggregation during preparation and catalytic reaction, resulting in a dynamic decay of catalytic performance and durability.[1] Consequently, supports have been introduced to ensure the uniform dispersions of MNPs during preparation and reaction. Preeminent supports are supposed

to have large surface areas, strong metal-support interactions, and abundant anchor sites for active species that participate in the catalytic process, leading to an extensive study of porous supports like silica, graphene oxides, and carbons with modified surfaces rather than crude ones.[2]

Hydrogen is a promising energy carrier in future energy society, and hydrogen generation from chemical hydrides has attracted lots of attention.[3] Formic acid (FA), a major product of biomass processing,[4] with a 4.4 wt % hydrogen content is a promising liquid carrier for hydrogen.[5] As we know, Pd is one of the most active noble metal catalysts for dehydrogenation of FA.[6] Newly emerging nitrogen-doped carbons (NCs) can stabilize and provide Pd NPs with a uniform dispersion and a strong electronic effect, causing an enhanced catalytic performance for FA dehydrogenation.[7] However, compared with the homogeneous catalysts for FA dehydrogenation, heterogeneous catalysts still suffer from low activities.[8]

To our knowledge, hierarchically porous carbons, especially those having a meso-/micro-pore size distribution, have been widely used in catalysis, as microporosity can provide numerous anchor sites for MNPs which serve as active sites during catalytic process, and mesoporosity is favored for the efficient mass transport in the carbon structure.[9] Considering this, metal−organic frameworks (MOFs), with tunable porous structures constructed by metal (clusters) and organic ligands with huge diversity, have become a class of ideal precursors for carbonization, while precise control of the pore structures remains challenging.[10] To this end, learning from universal activation process for hierarchically porous carbons, post-treatment applying calcination with active agents such as KOH has been taken into consideration.[11]

Herein, we employ an Al-based MOF, Al-MIL-101-NH_2, built up of N-containing

ligands (2-aminoterephthalic acid) and Al clusters with large hydrophilic zeotypic pores (2−3 nm) and windows (d ≈ 1.2 and 1.6 nm), as a sacrificial template to synthesize in situ N-doped carbon composite through carbonization. Followed by the activation approach employing ultrasonication in aq KOH, a hierarchically porous carbon including micro- and mesopores was obtained and used as the support to immobilize Pd NPs. As a result, the ultrafine Pd NPs (Pd@CN900K) with a mean size of 1.1 ± 0.2 nm show a TOF value of 14400 h^{-1} at 60 °C for the dehydrogenation of aqueous solution of FA and sodium formate (SF).

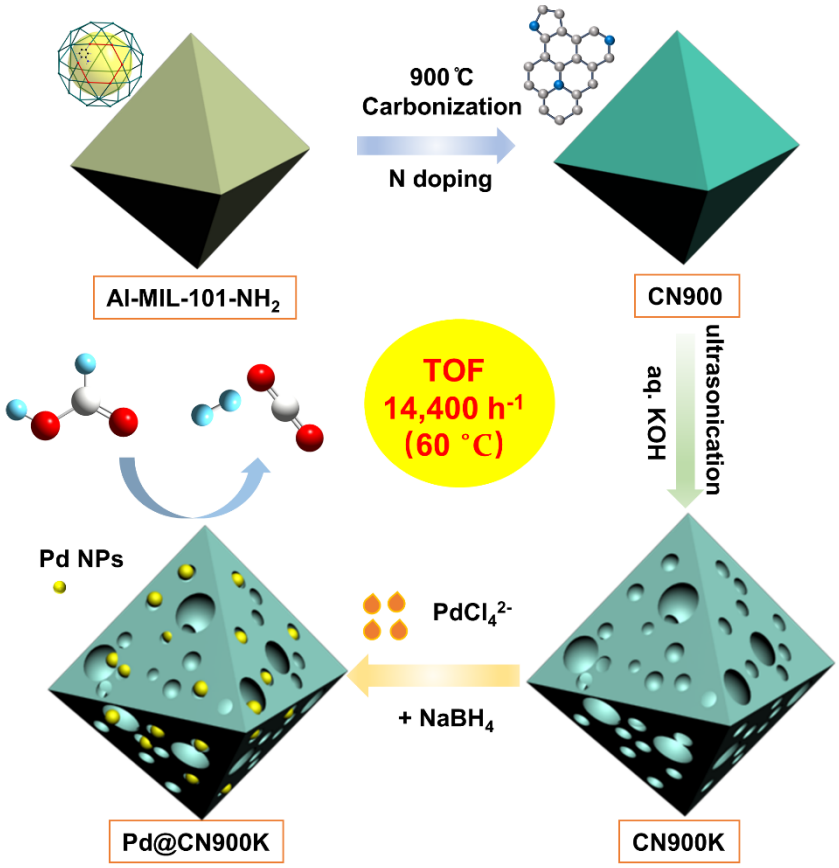

Figure 2.1. Schematic Representation for the Synthesis of Pd@CN900K.

The synthetic strategy of Pd nanocatalyst is illustrated in Figure 2.1. Briefly, Al-MIL-101-NH_2 was synthesized as reported previously,[12] and the resulting product was used as a sacrificial template to synthesize N-doped carbon/Al_2O_3 composite (designated as

CN900) via carbonization at 900 °C in an argon flow. The subsequent ultrasonication in aq KOH, followed by washing with deionized (DI) water, resulted in a hierarchically porous carbon including micro- and mesopores without Al_2O_3 (designated as CN900K, K for KOH etching), which was used as a support to immobilize Pd NPs by a typical wet chemical reduction process using sodium borohydride ($NaBH_4$) as the reducing agent. The as-synthesized catalyst (designated as Pd@CN900K) was used for FA dehydrogenation.

2.2 Experimental section

2.2.1 Materials and general methods

All chemicals were commercially available and used without further purification. Aluminum chloride hexahydrate ($AlCl_3 \cdot 6H_2O$, Wako Pure Chemical Industries, 97.0%), 2-aminoterephthalic acid (Tokyo Chemical Industry Co., Ltd., ≥98.0%), N, N-dimethylformamide (DMF, Tokyo Chemical Industry Co., Ltd., 99%), ethanol (C_2H_5OH, Kishida Chem. Co., >99.8%), potassium hydroxide (KOH, Kishida Chem. Co., >85%), potassium tetrachloropalladate (K_2PdCl_4, Wako Pure Chemical Industries, >97%), sodium borohyride ($NaBH_4$, Tokyo Chemical Industry Co., Ltd., 99%), formic acid (FA, HCOOH, Kishida Chem. Co., >98%) and sodium formate dehydrate (SF, HCOONa, Sigma-Aldrich, >99.5%) were used as received. De-ionized (DI) water with a specific resistance of 18.2 MΩ·cm was obtained by reverse osmosis followed by ion-exchange and filtration (RFD 250NB, Toyo Seisakusho Kaisha, Ltd., Japan).

Laboratory powder X-ray diffraction (XRD) patterns were collected for the samples on a Rigaku Ultima IV X-ray diffractometer with Cu Kα source (40 kV, 40 mA). The N_2 adsorption/desorption isotherms were obtained at 77 K using automatic volumetric

adsorption equipment (Belsorp-max). The metal contents of the catalysts were analyzed by inductively coupled plasma-optical emission spectroscopy (ICP-OES) on Thermo Scientific iCAP6300. The X-ray photoelectron spectroscopy (XPS) analyses were recorded on a Shimadzu ESCA-3400 using an Mg Kα source. The transmission electron microscopic (TEM) and high-annular dark-field scanning TEM (HAADF-STEM) images were collected on TECNAI G^2 F20 transmission electron microscope with operating voltage at 200 kV and elemental mapping analyses were recorded on a Titan3 G2 60-300 (FEI) with a Super-X EDS system (Bruker) under operating voltages of 300 kV. Elemental analyses were performed on CE EA1110 and Perkinelmer 2400II instruments. After purging the reactor with nitrogen for three times, the dehydrogenation of formic acid was carried out, and the generated gas was collected, which was analyzed by GC-8A (molecular sieve 5A, Ar as carrier gas) and GC-8A (Porapack N, He as carrier gas) analyzers (Shimadzu). Ultrasonication was performed in ASU cleaner (ASU-10) (40 kHz, 500 W).

2.2.2 Synthesis of Al-MIL-101-NH_2

Al-MIL-101-NH_2 was synthesized according to the reported method.[12] Typically, 2-aminoterephthalic acid (2.77 g, 15 mmol) was dissolved in N, N -dimethylformamide (DMF, 600 mL) in a 1000 mL two-neck round-bottom flask and heated to 110 °C in an oil bath. $AlCl_3 \cdot 6H_2O$ (7.24 g, 30 mmol) was added in 7 equal portions with a time delay of 15 min between each two additions. After the complete addition of $AlCl_3 \cdot 6H_2O$, the mixture was kept at 110 °C with stirring for another 3 h and an additional 16 h in the oven at 110 °C without stirring. The yellow product was centrifuged from the mixture and washed by fresh DMF and ethanol for three times and then further purified by reflux at 90 °C in ethanol (500 mL) for 24 h without stirring. After reflux, the product was washed

by ethanol again and finally dried in the vacuum oven at 90 °C for 24 h for future use.

2.2.3 Syntheses of Al-MIL-101-NH_2-derived carbons

About 0.8 g of Al-MIL-101-NH_2 was transferred into a ceramic boat and placed into a temperature-programed furnace under an argon atmosphere. Subsequently, carbonization was performed at 900 °C (or 600, 700, 800, and 1000 °C) for 2 h with a heating speed of 3 °C/min (designated as CN*T*, *T* for the carbonization temperature (°C)). Samples were cooled down to room temperature naturally. Carbon composites were then activated with ultrasonication (40 kHz, 500 W) in aqueous KOH (2 M, 100 mL) for 24 h, washed by DI water for 3 times, and finally dried at 60 °C overnight (designated as CN*T*K, K for ultrasonication activation in aq. KOH).

2.2.4 Syntheses of Pd nanocatalysts

As-synthesized carbons were applied as supports for the preparation of Pd nanocatalysts. In a typical procedure, 50 mg CN900K was dispersed into 50 mL DI water with subsequent addition of K_2PdCl_4 solution (0.1 M, 0.5 mL) with stirring. After 1 h, fresh $NaBH_4$ solution (50 mg $NaBH_4$ dissolved in 1 mL H_2O) was injected into the mixture rapidly with a continuous stirring for 1 h. Finally, the catalysts were washed by DI water for 3 times and centrifuged for catalysis use without further treatment (designated as Pd@CN900K). For comparison, by the same procedure, Pd@CN*T*K catalysts were also synthesized.

2.2.5 Procedure for the dehydrogenation of formic acid

Reaction apparatus for measuring the H_2/CO_2 evolution from the FA/SF system are the same as previously reported.[13] In general, a 2.0 mL dispersion of as-synthesized catalyst in water was placed in a two-necked round-bottom flask (30 mL) which was placed in a water bath at a preset temperature. A gas burette filled with water was connected to the

reaction flask to measure the volume of released gas (the temperature was kept constant at 298 K during measurements). The reaction started when 1.0 mL of the mixed aqueous solution containing FA and SF was injected into the mixture. The volume of the generated gas was monitored by recording the displacement of water in the gas burette.

2.2.6 Determination of activation parameters and kinetic orders

a. Determination of activation parameters

In a typical procedure of FA dehydrogenation, 3.0 mL aqueous dispersion ([Pd] = 0.017 M, [FA] = 1.0 M and [SF] = 3.0 M) in a two-necked round-bottom flask (30 mL) was placed in a water bath at different preset temperatures (25, 30, 40, 50 and 60 °C) and the released gas was recorded by the displacement of water in the gas burette.

b. Determination of kinetic orders

We controlled the initial concentrations of Pd, SF and FA to study the kinetic orders of FA dehydrogenation over Pd@CN900K (the gas generation rate (k_{obs}) was calculated based on the initial linear portion of each plot). The experimental details were as follows:

(1) Dependence on Pd concentration

3.0 mL aqueous dispersion ([FA] = 1.0 M and [SF] = 3.0 M) starting with different Pd concentrations (3.3, 6.7, 10.0, 13.3 and 16.7 mM) in a two-necked round-bottom flask (30 mL) was placed in a water bath at 30 °C and the released gas was recorded by the displacement of water in the gas burette.

(2) Dependence on SF concentration

3.0 mL aqueous dispersion ([Pd] = 0.017 M and [FA] = 1.0 M) starting with different SF concentrations (0, 1.0, 2.0, 2.5 and 3.0 M) in a two-necked round-bottom flask (30 mL) was placed in a water bath at 60 ℃ and the released gas was recorded by the displacement of water in the gas burette.

(3) Dependence on FA concentration

3.0 mL aqueous dispersion ([Pd] = 0.017 M and [SF] = 3.0 M) starting with different FA concentrations (0.25, 0.50, 0.75 and 1.0 M) in a two-necked round-bottom flask (30 mL) was placed in a water bath at 30 ℃ and the released gas was recorded by the displacement of water in the gas burette.

2.2.7 Durability testing of Pd@CN900K

a. For testing the durability of Pd@CN900K, the catalyst was recollected from the reaction mixture by centrifugation after the completion of previous catalytic reaction cycle and washed with DI water for 3 times. Then the catalyst was used in the FA dehydrogenation for the next cycle ([Pd] = 0.017 M, [FA] = 1.0 M and [SF] = 3.0 M in 3.0 mL aqueous dispersion). Such test cycles of the catalyst for FA dehydrogenation were carried out for 5 runs at 60 °C.

b. For testing the TON value of Pd@CN900K, the catalyst was reused for 15 times for FA dehydrogenation at 60 °C. Pd@CN900K was used as the catalyst for each run ([Pd] = 0.01 M, [FA] = 1.8 M and [SF] = 5.4 M in 5.0 mL aqueous dispersion). After the completion of each run, the catalyst was centrifuged and washed by DI water, and then used for the next run.

2.2.8 Control experiments

For comparison, Pd@CN*T*K catalysts (*T* = 600, 700, 800 and 1000 °C) were also used for FA dehydrogenation ([Pd] = 0.017 M, [FA] = 1.0 M and [SF] = 3.0 M in 3.0 mL aqueous dispersion) at 30 ℃.

2.2.9 Calculation methods

The turnover frequency (TOF) reported here is an apparent TOF value based on the number of Pd atoms in catalysts, which is calculated from the equation as follow:

$$TOF = P_0V/(2RTn_{Pd}t)$$

Where P_0 is the atmospheric pressure (101325 Pa), V is the final generated volume of (H_2 + CO_2) gas, R is the universal gas constant (8.3145 m^3 Pa mol^{-1} K^{-1}), T is the room temperature (298 K), n_{Pd} is the total mole number of Pd atoms in catalyst and t is the completion time of the reaction in hour.

2.3 Results and discussion

2.3.1 Characterization

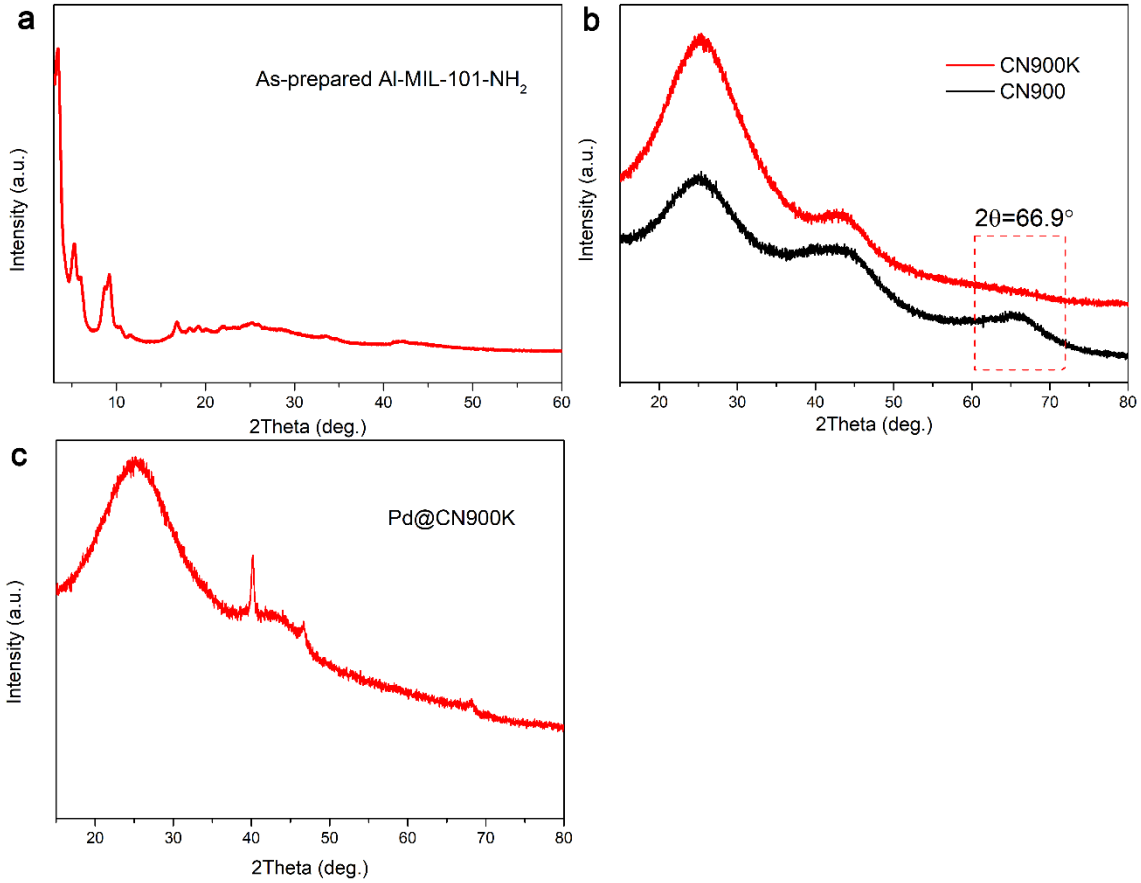

Figure 2.2. The XRD patterns of (a) as-prepared Al-MIL-101-NH_2, (b) carbons before (CN900) and after (CN900K) ultrasonication in aq. KOH and (c) Pd@CN900K.

Based on the results of powder X-ray diffraction (PXRD) analysis, Al-MIL-101-NH_2 was

successfully synthesized (Figure 2.2a). For CN900, two broad diffraction peaks corresponding to carbon were observed at 24.7 and 44°, and a broad peak corresponding to Al_2O_3 was observed at 66.9°, which disappeared after ultrasonication in aq. KOH (Figure 2.2b). Inductively coupled plasma-optical emission spectroscopy (ICP-OES) analysis further confirmed that the Al content decreases from 27.0 wt% of CN900 to 1.4 wt% of CN900K. Three peaks at 40.1, 46.7 and 68.1° for Pd were observed in Pd@CN900K, attributed to the (111), (200) and (220) diffractions (JCPDS: 46-1043), respectively, indicating the formation of Pd^0 on carbon (Figure 2.2c).

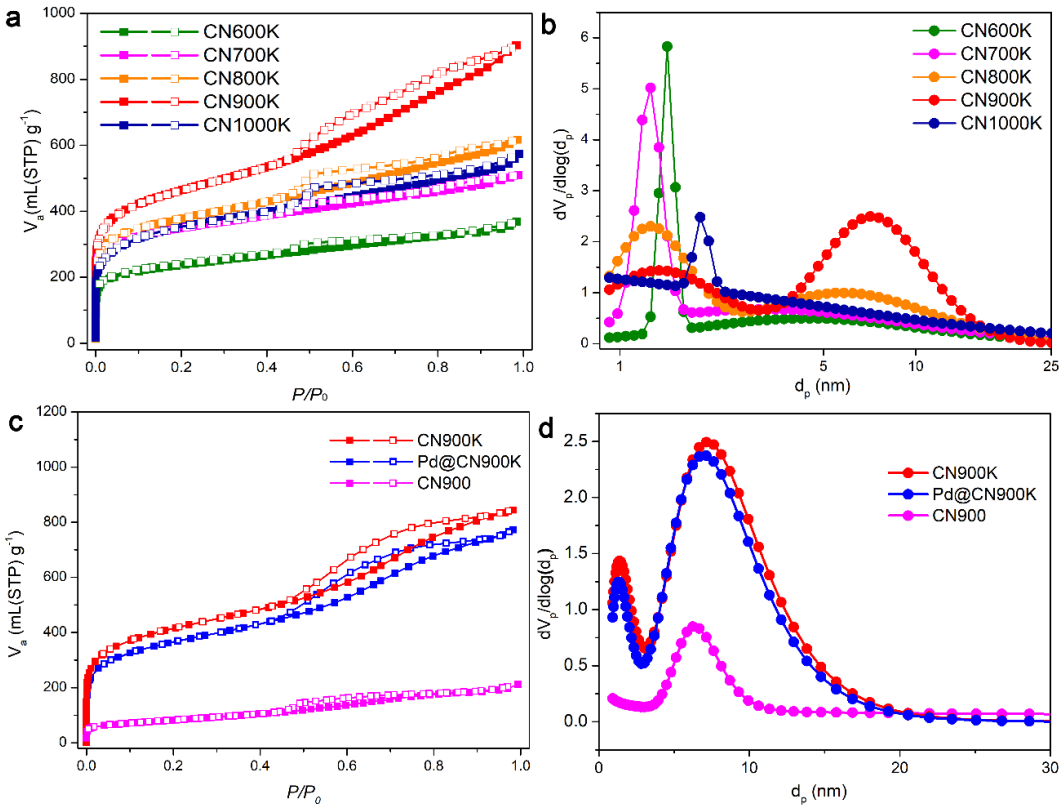

Figure 2.3. N_2 sorption isotherms (77 K) and the corresponding pore size distributions calculated using NL-DFT method of (a, b) CN600K, CN700K, CN800K, CN900K and CN1000K, and (c, d) CN900, CN900K and Pd@CN900K (filled and open symbols represent adsorption and desorption branches, respectively).

Table 2.1. BET specific surface areas and pore volumes of the as-synthesized carbons and Pd@CN900K.

Sample	BET surface area (m^2 g^{-1})	Total pore volume (cm^3 g^{-1})
CN900	287	0.32
CN900K	1382	1.31
Pd@CN900K	1220	1.20
CN600K	762	0.57
CN700K	1115	0.79
CN800K	1228	0.95
CN1000K	1143	0.89

Nitrogen (N_2) sorption measurements were used to study the pore structures of the carbons prepared at different carbonization temperatures from 600 to 1000 °C followed by the subsequent ultrasonication in aq. KOH (designated as CN*T*K, *T* for the carbonization temperature (°C)). Based on N_2 sorption isotherms, the BET specific surface area (S_{BET}) of CN*T*K increases from 762 to 1382 m^2 g^{-1} with increasing the carbonization temperature from 600 to 900 °C, but then turns to decrease to 1143 m^2 g^{-1} at 1000 °C (Figure 2.3a and Table 2.1). Pore size distribution analyses reveal that with increasing the carbonization temperature from 600 to 900 °C, the volume ratio of mesopores to micropores increases and reaches the highest value at 900 °C, but decreases dramatically at 1000 °C. CN900K possesses a hierarchical pore structure including micropores with a diameter centered at 1.4 nm and mesopores with a diameter centered at 7.1 nm. (Figure 2.3b). Compared to CN900 with a S_{BET} of 287 m^2 g^{-1} and a pore volume

of 0.32 cm^3 g^{-1}, CN900K shows a much higher S_{BET} of 1382 m^2 g^{-1} and pore volume of 1.31 cm^3 g^{-1}. Pd@CN900K shows a lower S_{BET} of 1220 m^2 g^{-1} and pore volume of 1.20 cm^3 g^{-1} than CN900K, indicating the successful immobilization of Pd NPs in the pores of the carbon (Figure 2.3c-d and Table 2.1).

Scanning electron microscopy (SEM) measurements show that CN900K keeps a similar size and morphology as Al-MIL-101-NH_2 (Figure 2.4). Transmission electron microscopy (TEM) and high-angle annular dark-field scanning TEM (HAADF-STEM) measurements (Figure 2.5 and 2.6) reveal that Pd@CN900K possesses well-dispersed ultrafine Pd NPs (1.1 ± 0.2 nm), which is in accordance with the size of micropores (1.4 nm) of CN900K, implying that Pd NPs may be partially immobilized in micropores. Elemental mapping images display the uniform distribution of N and Pd on the carbon (Figure 2.7). ICP-OES analysis shows that Pd@CN900K has a Pd content of 9.3 wt%, which is very close to the theoretical Pd content (9.6 wt%).

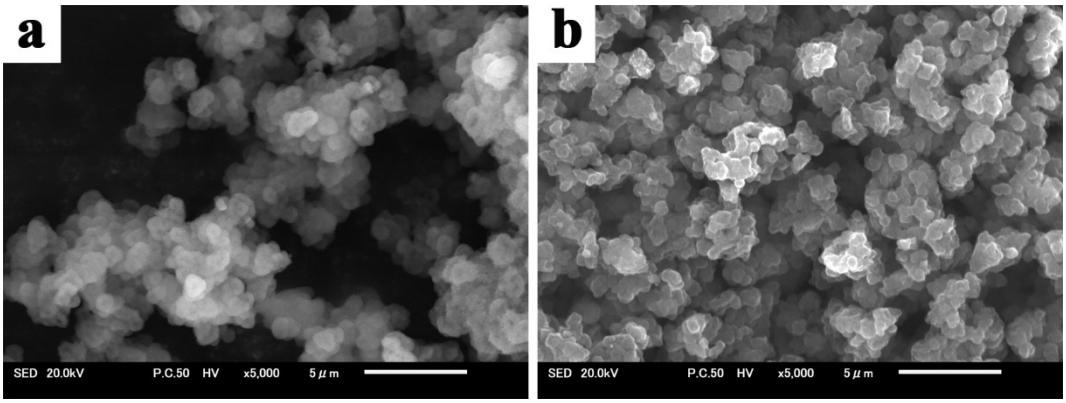

Figure 2.4. The SEM images of (a) Al-MIL-101-NH_2 and (b) CN900K.

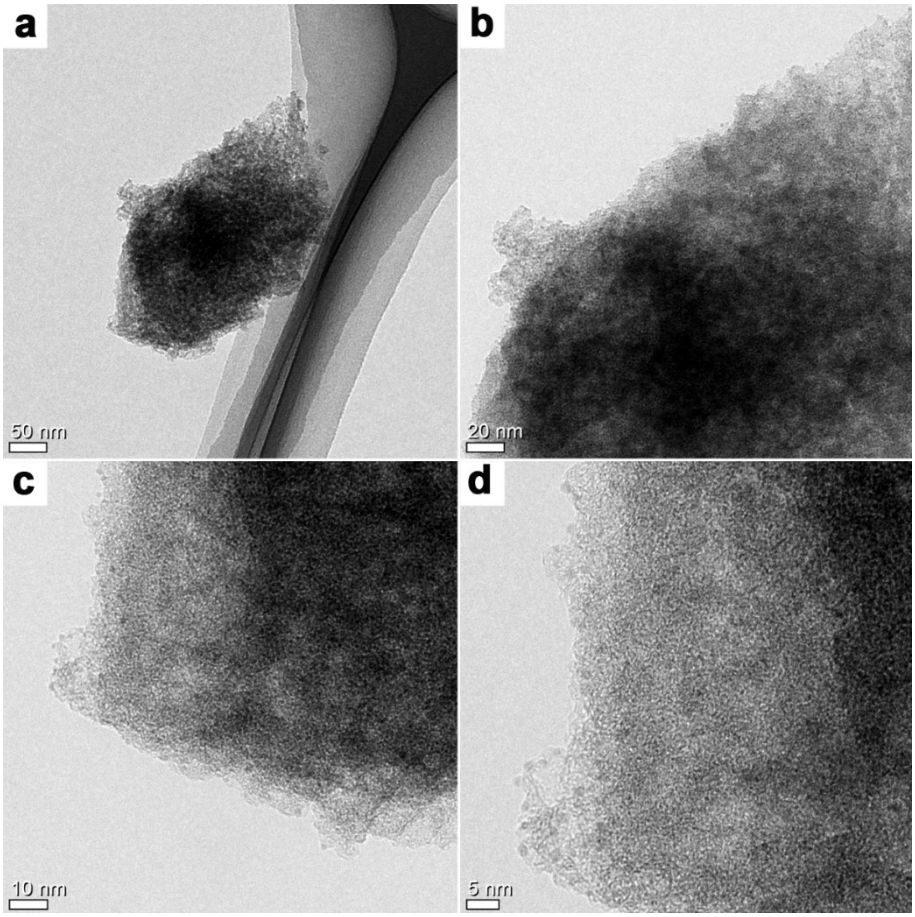

Figure 2.5. TEM images of Pd@CN900K.

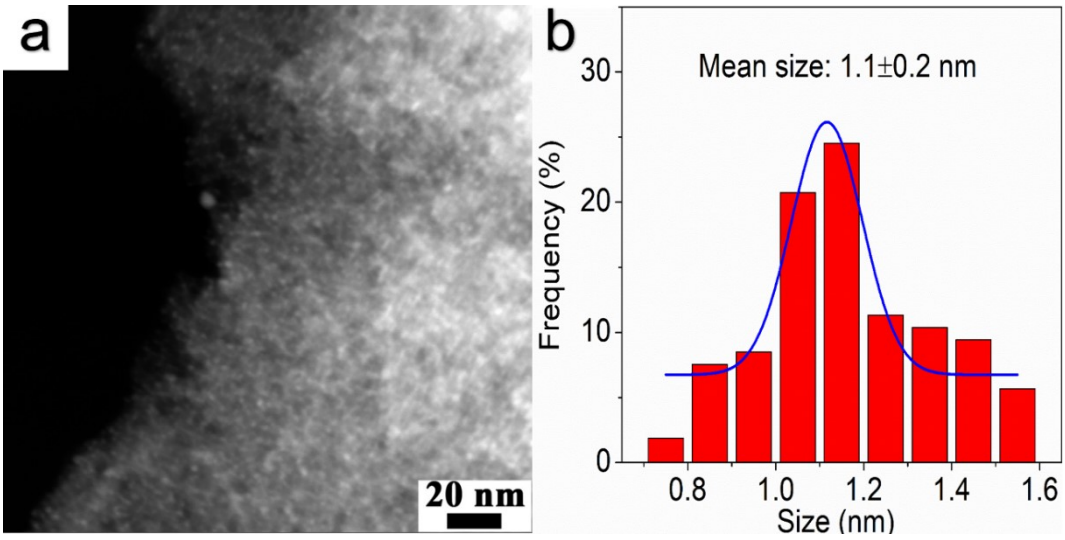

Figure 2.6. (a) HAADF-STEM image and (b) the corresponding particle size distribution of Pd NPs of Pd@CN900K catalyst.

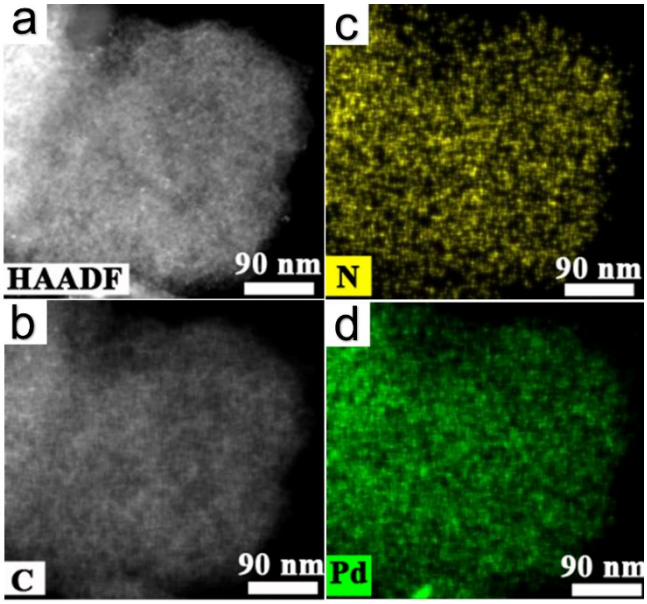

Figure 2.7. (a) HAADF-STEM image and (b, c, d) the corresponding elemental mapping images of Pd@CN900K.

The X-ray photoelectron spectroscopy (XPS) analyses of CN900K reveal the existence of abundant N and oxygen (O) species. Three types of nitrogen species, with deconvoluted peaks located at 398.7, 400.1 and 401 eV, were detected, which are assigned to pyridinic, pyrrolic and graphitic N, respectively (Figure 2.8a). Elemental analysis shows CN900K has a N content of 4.86 wt% (Table 2.2). The O 1s spectrum exhibits two peaks at 531.8 and 533.3 eV, which are attributed to C=O and C–OH groups, respectively (Figure 2.8b). For Pd@CN900K, a doublet corresponding to Pd $3d_{5/2}$ and Pd $3d_{3/2}$ were observed. The Pd $3d_{5/2}$ peaks at 337.5 eV and 335.9 eV are assigned to Pd^{2+} and Pd^{0}, respectively (Figure 2.8c). The presence of Pd^{2+} may be attributed to the oxidation of the surface Pd NPs in air, due to its high activity and the strong interactions between the Pd^{2+} precursors and the doped N, making it difficult to reduce the Pd^{2+}.

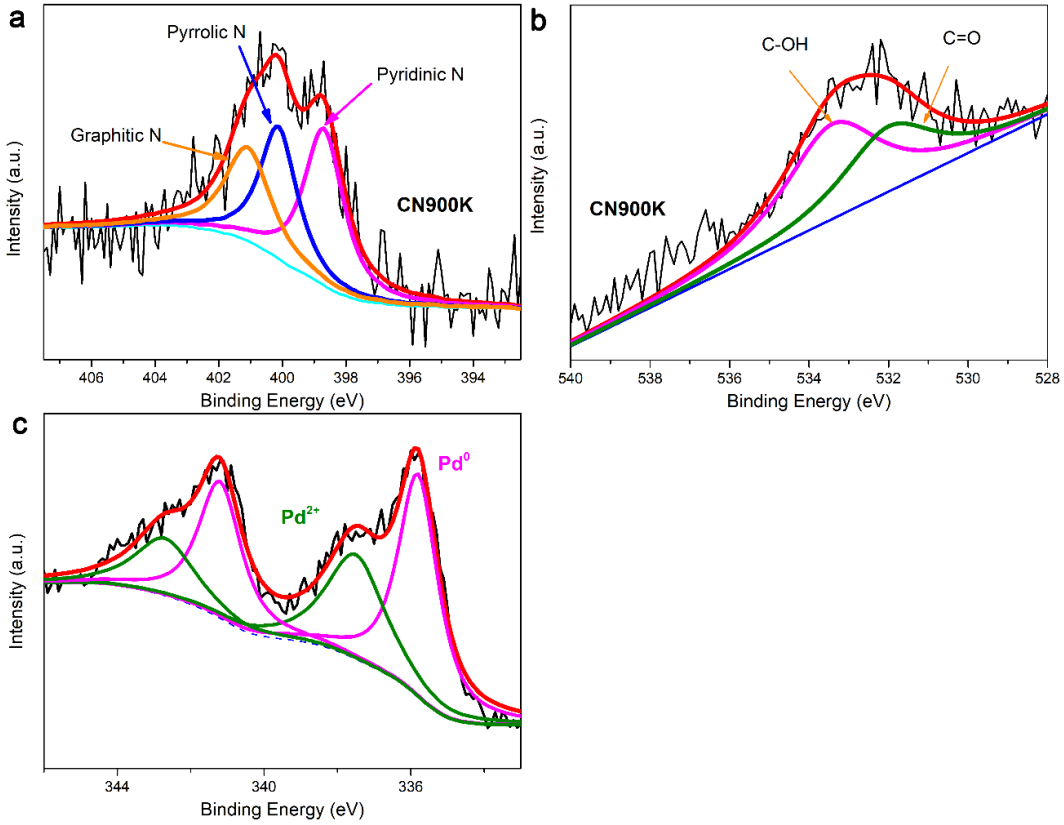

Figure 2.8. XPS spectra of (a) N 1s and (b) O 1s of CN900K, and (c) Pd 3d of Pd@CN9000K.

Table 2.2. Nitrogen (N) contents of as-prepared samples

Sample	N content
CN900	3.62%
CN900K	4.86%
Pd@CN900K	4.76%

2.3.2 Catalytic activity and durability

The catalytic ability of Pd nanocatalyst was studied by hydrogen evolution from FA/SF solution. In a typical process, 1.0 mL aqueous solution of FA/SF was injected to a 2.0 mL dispersion of the catalyst (Pd@CN900K) in water at a certain temperature and the

released gas was measured volumetrically by a water burette. Gas of 144 mL can be released from FA/SF solution in 15 seconds at 60 °C ([Pd] = 0.017 M, [FA] = 1.0 M and [SF] = 3.0 M in 3.0 mL aqueous dispersion) and a TOF value of 14400 h^{-1} was calculated on the basis of total Pd amount (Table 2.3 and Figure 2.9). Gas chromatography (GC) shows that the generated gas contains H_2 and CO_2, and no CO was detected at the level of detection limit of 10 ppm, indicating a complete dehydrogenation of FA (Figure 2.10). Pd@CN900K is highly active with a 100 % H_2 selectivity for the dehydrogenation of FA, showing a great potential for practice use in energy storage. Generally, the gas generation rate over a catalyst greatly depends on the reaction temperature. TOF values of Pd@CN900K obtained at different temperatures (25, 30, 40, 50 and 60 °C) were collected to fit the Arrhenius plot and the gas generation rates were used to give Eyring plot (Figure 2.9). Activation parameters are calculated and shown as follows: activation energy E_a = 46.9 kJ mol^{-1}, activation enthalpy $\Delta H^{\neq}$ = 44.4 kJ mol^{-1} and activation entropy $\Delta S^{\neq}$ = -60.1 J mol^{-1} K. Obviously, the catalytic property of Pd@CN900K can be improved dramatically by increasing the reaction temperature.

Table 2.3. Catalytic activities of latest heterogeneous catalysts for dehydrogenation of formic acid

Catalyst	Temp. (°C)	Additive	TOF (h^{-1})	Ref.
Pd/C_m	60	HCOONa	7256[a, #]	2e
Pd-MnO_x/SiO_2-NH_2	50	None	1300[a, #]	14
Pd/CN0.25	25	None	5530[b, #]	7a
Pd/N-MSC-30-two-	60	HCOONa	8414[a, *]	7d
Pd^0/CeO_2	25	HCOONa	1400[a, #]	15
$Pd_{60}Au_{40}$/ZrSBA-15-	25	None	1185[a, #]	16
0.8Pd-	60	None	5803[a, #]	17

Pd/NH_2-KIE-6	25	None	8185[b, #]	18
PdO/C	30	HCOONa	3172[b, #]	19
PdAg@ZrO_2/C/rGO	60	HCOONa	4500[a, *]	20
Pd@CN900K	25	HCOONa	**1963** [a, *]	**This work**

[a] *TOF values calculated on total metal atoms.*

[b] *TOF values calculated on surface metal sites or active sites.*

[#] *Initial TOF values calculated on initial time or initial conversion of FA.*

[*] *TOF values calculated on the complete time of gas releasing.*

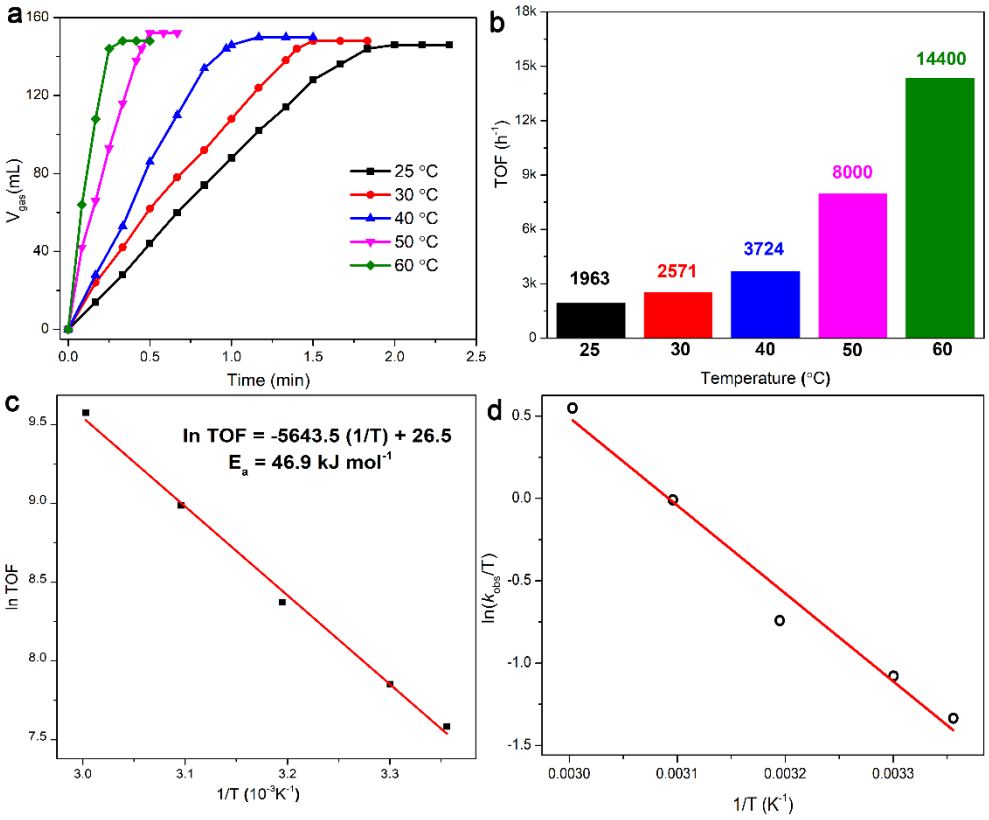

Figure 2.9. (a) The temperature dependence of gas evolution from aqueous FA/SF solution over Pd@CN900K catalyst ([Pd] = 0.017 M, [FA] = 1.0 M and [SF] = 3.0 M in 3.0 mL aqueous dispersion), and the corresponding (b) TOF values, (c) Arrhenius plot (lnTOF) vs. 1/*T*) and (d) Eyring plot (y = -5340x + 16.5 and R^2 = 0.97).

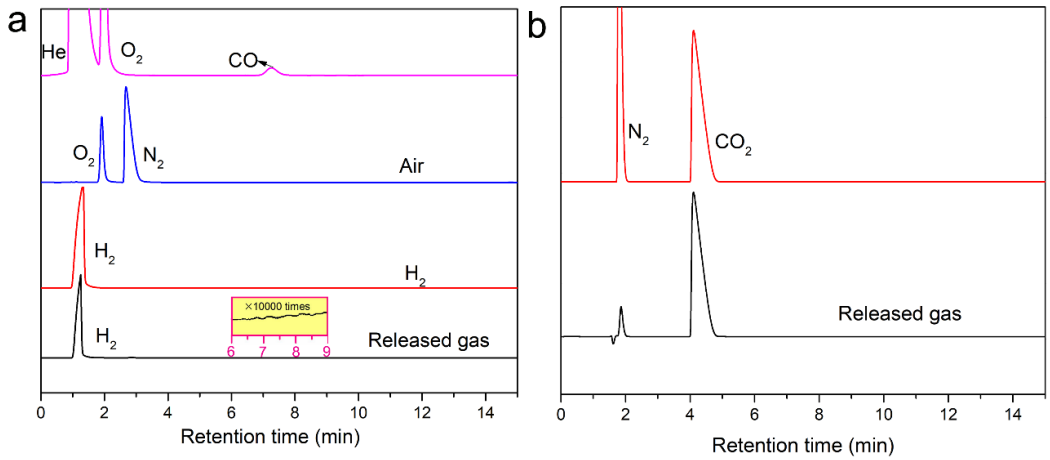

Figure 2.10. Gas chromatograms of (a) CO, air and H_2 as reference gases and (b) CO_2 as reference gas from the decomposition of FA/SF in the presence of Pd@CN900K ([Pd] = 0.017 M, [FA] = 1.0 M and [SF] = 3.0 M in 3.0 mL aqueous dispersion at 60 °C), showing the presence of H_2 and CO_2 and the absence of CO at the detection limit of 10 ppm in the released gas.

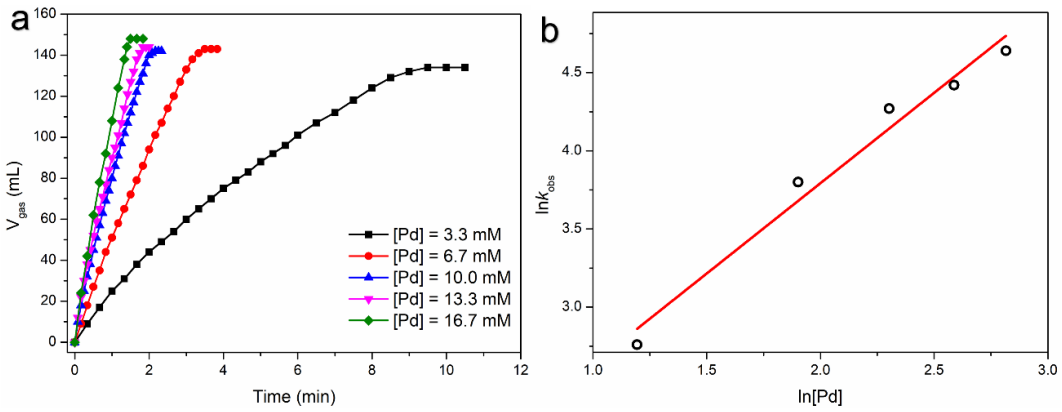

Figure 2.11. (a) The volume of the generated gas (CO_2 + H_2) *versus* time and (b) plot of the gas generation rate *versus* the Pd concentration (both in logarithmic scale; y = 1.16x + 1.48 and R^2 = 0.97) for the dehydrogenation of FA over Pd@CN900K ([FA] = 1.0 M and [SF] = 3.0 M in 3.0 mL aqueous dispersion) starting with different Pd concentrations at 30 °C.

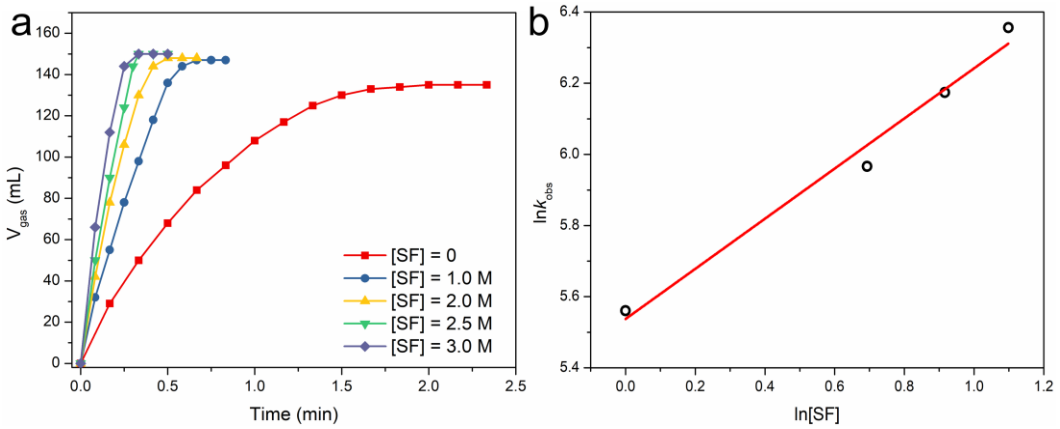

Figure 2.12. (a) The volume of the generated gas (CO_2 + H_2) *versus* time and (b) plot of the gas generation rate *versus* the SF concentration (both in logarithmic scale; y = 0.70x + 5.54 and R^2 = 0.97) for the dehydrogenation of FA over Pd@CN900K ([Pd] = 0.017 M and [FA] = 1.0 M in 3.0 mL aqueous dispersion) starting with different SF concentrations at 60 °C.

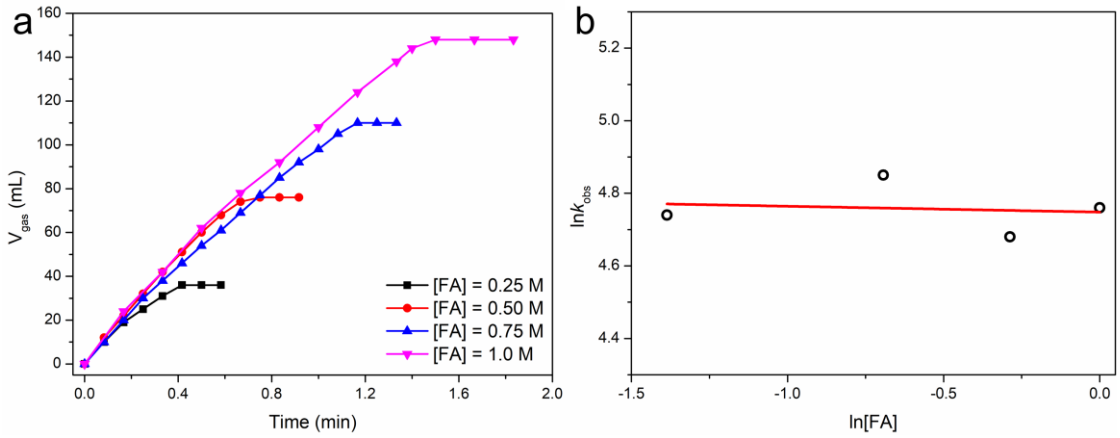

Figure 2.13. (a) The volume of the generated gas (CO_2 + H_2) *versus* time and (b) plot of the gas generation rate *versus* the FA concentration (both in logarithmic scale) for the dehydrogenation of FA over Pd@CN900K ([Pd] = 0.017 M and [SF] = 3.0 M in 3.0 mL aqueous dispersion) starting with different FA concentrations at 30 °C.

In addition, kinetic studies about the dependence of FA dehydrogenation rate on Pd, SF and FA concentrations over Pd@CN900K were carried out. The results show that the

reaction is close to the first-order dependence on Pd concentration, half-order dependence on SF concentration and zero-order dependence on FA concentration, respectively (Figure 2.11, 2.12 and 2.13). It is noteworthy that even without SF addition, Pd@CN900K shows a TOF value as high as 1800 h^{-1} at 60 °C, which is among the best heterogeneous catalysts for dehydrogenation of FA without SF (Figure 2.12 and Table2.3).

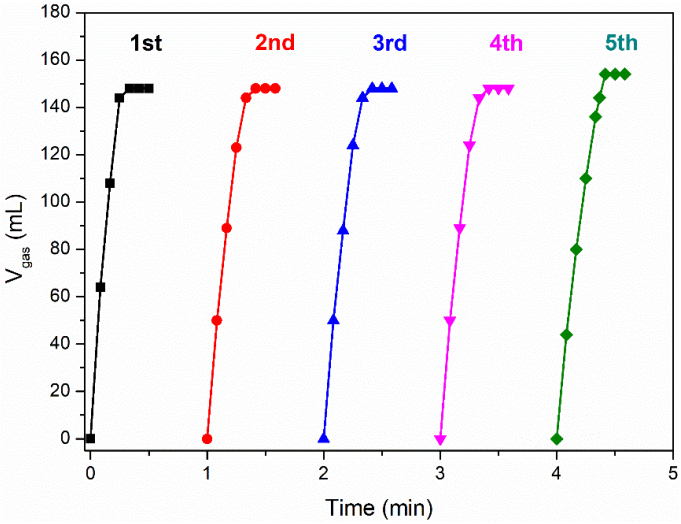

Figure 2.14. Durability test (5 cycles) of Pd@CN900K for the dehydrogenation of FA/SF ([Pd] = 0.017 M, [FA] = 1.0 M and [SF] = 3.0 M in 3.0 mL aqueous dispersion at 60 °C).

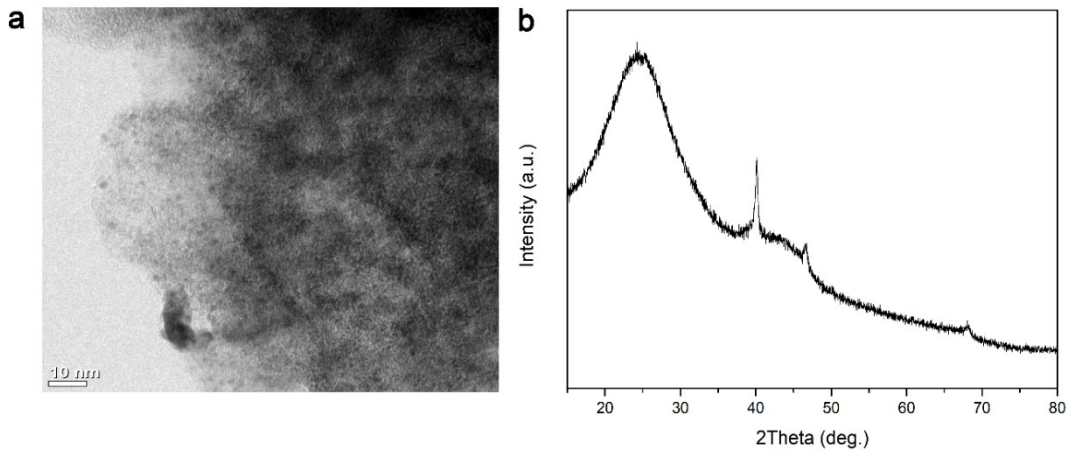

Figure 2.15. (a) TEM image and (b) XRD pattern of Pd@CN900K after dehydrogenation for 5 cycles ([Pd] = 0.017 M, [FA] = 1.0 M and [SF] = 3.0 M in 3.0 mL aqueous dispersion at 60 °C).

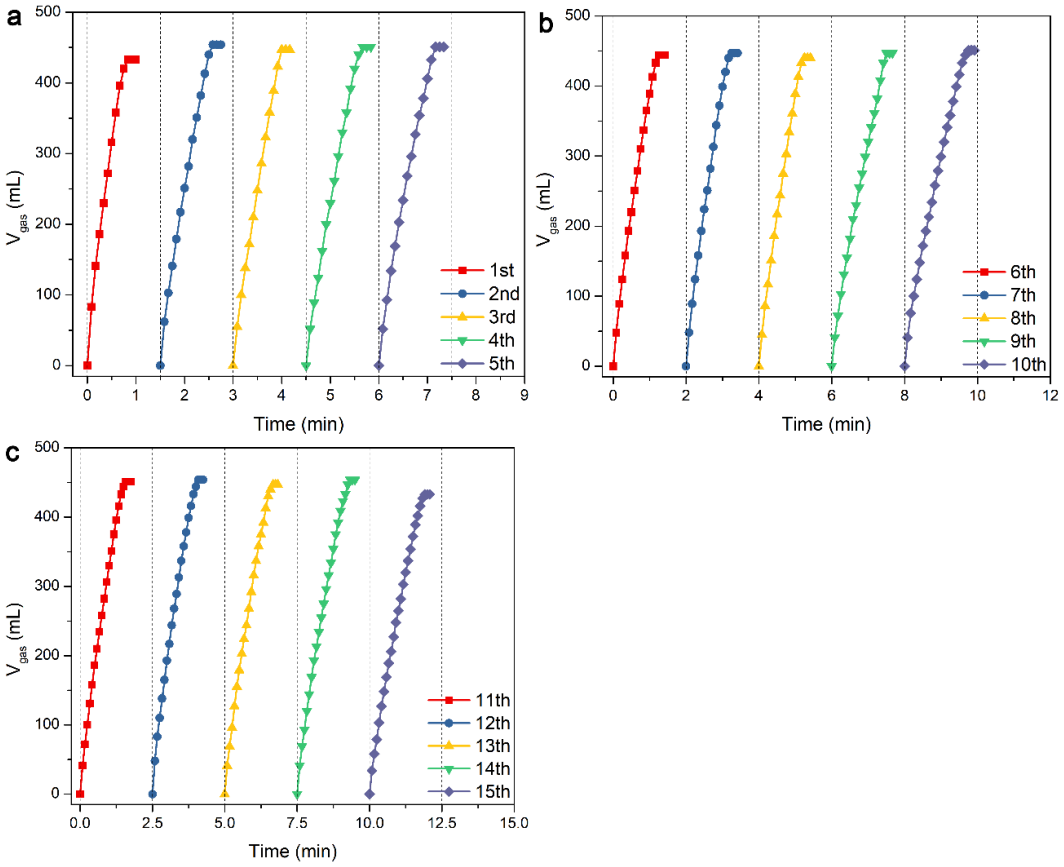

Figure 2.16. Tolerance test for FA dehydrogenation over Pd@CN900K ([Pd] = 0.01 M, [FA] = 1.8 M and [SF] = 5.4 M in 5.0 mL aqueous dispersion at 60 °C).

Since the stability/durability of a catalyst is vital for the practice application, the cycle experiment of dehydrogenation of FA over Pd@CN900K ([Pd] = 0.017 M, [FA] = 1.0 M and [SF] = 3.0 M in 3.0 mL aqueous dispersion) at 60 °C was investigated. After each cycle, the catalyst was centrifuged from the reactants and washed by DI water. 1.0 mL aqueous solution of FA/SF of the same concentration was injected to the 2.0 mL dispersion of catalyst for each run. No significant loss in activity was observed over 5 cycles (Figure 2.14). Furthermore, after catalysis for 5 cycles, Pd@CN900K was examined by TEM and XRD measurements and no significant changes of Pd particle sizes and morphologies were observed (Figure 2.15). In addition, Pd@CN900K was reused for 15 times at 60 °C ([Pd] = 0.01 M, [FA] = 1.8 M and [SF] = 5.4 M in 5.0 mL

aqueous dispersion) to test its tolerance and 135 mmol FA was completely dehydrogenated, corresponding to a TON value of 2700 (Figure 2.16). In conclusion, Pd@CN900K catalyst possesses a high stability/durability under the current FA dehydrogenation conditions.

For comparison, Pd NPs immobilized to the porous carbons prepared at different temperatures were also synthesized. Pd@CN600K, Pd@CN700K, Pd@CN800K and Pd@CN1000K exhibit TOF values of 1080, 1565, 1963 and 2204 h^{-1} for dehydrogenation of FA at 30 °C, respectively, which are lower than that of Pd@CN900K (TOF, 2571 h^{-1})(Figure 2.17). This might be attributed to the smaller Pd NPs of Pd@CN900K than the other samples (Figure 2.6 and 2.18), which can provide more accessible active sites for catalytic reaction, leading to a higher catalytic activity for FA dehydrogenation. Besides, the rich mesoporisity of Pd@CN900K is favored for effective mass transport during catalysis, which facilitates the catalytic process.

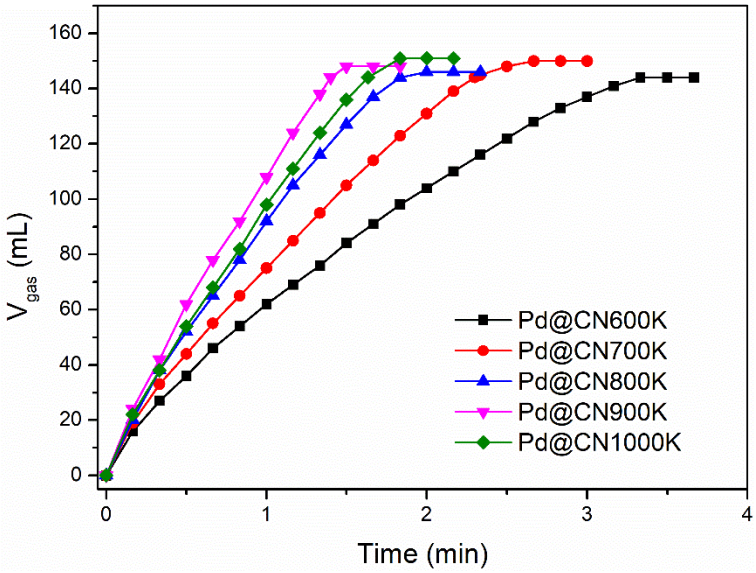

Figure 2.17. Volume of the generated gas (CO_2 + H_2) *versus* time for the dehydrogenation of FA/SF over Pd@CN*T*K (*T* is the carbonization temperature (°C); [Pd] = 0.017 M, [FA] = 1.0 M and [SF] = 3.0 M in 3.0 mL aqueous dispersion at 30 °C).

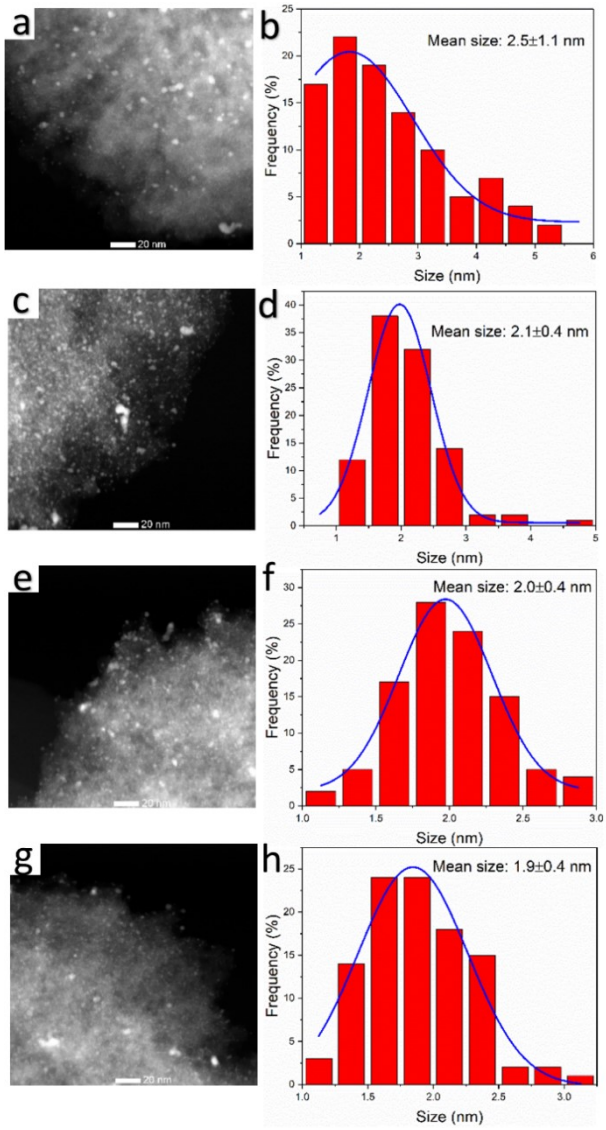

Figure 2.18. The HAADF-STEM images and the corresponding Pd particle size distributions of (a, b) Pd@CN600K, (c, d) Pd@CN700K, (e, f) Pd@CN800K and (g, h) Pd@CN1000K.

Homogeneous in-situ N doping also plays an important role for FA dehydrogenation. N species can stabilize Pd^{2+} precursors on the carbon and protect them from aggregation during synthetic and catalytic process (Figure 2.6 and 2.15). Meanwhile, the electronic effect between N atoms and Pd NPs could facilitate the cleavage of the C–H bonds in H–COOH, which is the rate determining step of the reaction.[7]

2.4 Conclusion

In summary, a hierarchically porous carbon was prepared from Al-MIL-101-NH_2 via carbonization, followed by activation under ultrasonication in aq. KOH. Highly dispersed ultrafine Pd NPs (1.1 ± 0.2 nm) have been successfully synthesized. By virtue of ultrafine Pd NPs, efficient mass transport brought by rich mesoporosity and the synergistic effect between the doped N in the support and the Pd NPs, the catalyst (Pd@CN900K) exhibits an extremely high catalytic activity with a TOF value of 14400 h^{-1} (60 °C), a good durability and a 100 % H_2 selectivity for dehydrogenation of FA. This activation approach of carbon opens an avenue for the syntheses of highly active supported ultrafine MNPs for catalysis.

References

(1) (a) Zahmakıran, M.; Özkar, S. *Nanosacale* **2011**, *3*, 3462-3481. (b) Dhakshinamoorthy, A.; Garcia, H. *Chem. Soc. Rev.* **2012**, *41*, 5262-5284. (c) Schauermann, S.; Nilius, N.; Shaikhutdinov, S.; Freund, H.-J. *Acc. Chem. Res.* **2013**, *46*, 1673-1681. (d) Zhang, W.; Lu, G.; Cui, C.; Liu, Y.; Li, S.; Yan, W.; Xing, C.; Chi, Y. R.; Yang, Y.; Huo, F. *Adv. Mater*. **2014**, *26*, 4056-4060. (e) Zhu, Q.-L.; Xu, Q. *Chem* **2016**, *1*, 220–245. (f) Yang, X.; Sun, J.-K.; Kitta, M.; Pang, H.; Xu, Q. *Nat. Catal.* **2018**, *1*, 214-220.

(2) (a) Yin, H.; Tang, H.; Wang, D.; Gao, Y.; Tang, Z. *ACS Nano* **2012**, *6*, 8288-8297. (b) Yadav, M.; Singh, A. K.; Tsumori, N.; Xu, Q. *J. Mater. Chem.* **2012**, *22*, 19146-19150. (c) Tan, C.; Huang, X.; Zhang, H. *Mater. Today* **2013**, *16*, 29-36. (d) Chen, Y.; Zhu, Q.-L.; Tsumori, N.; Xu, Q. *J. Am. Chem. Soc.* **2015**, *137*, 106-109. (e) Zhu, Q.-L.; Tsumori, N.; Xu, Q. *J. Am. Chem. Soc.* **2015**, *137*, 11743-11748.

(3) (a) Schlapbach, L.; Züttel, A. *Nature* **2001**, *414*, 353-358. (b) Graetz, J. *Chem. Soc.*

Rev. **2009**, *38*, 73-82. (c) Zhu, Q.-L.; Xu, Q. *Energy Environ. Sci*. **2015**, *8*, 478-512.

(4) (a) Jin, F.; Yun, J.; Li, G.; Kishita, A.; Tohji, K.; Enomoto, H. *Green Chem.* **2008**, *10*, 612-615. (b) Wang, W.; Niu, M.; Hou, Y.; Wu, W.; Liu, Z.; Liu, Q.; Ren, S.; Marsh, K. N. *Green Chem*. **2014**, *16*, 2614-2618.

(5) (a) Fellay, C.; Dyson, P. J.; Laurenczy, G. *Angew. Chem. Int. Ed.* **2008**, *47*, 3966-3968. (b) Boddien, A.; Mellmann, D.; Gärtner, F.; Jackstell, R.; Junge, H.; Dyson, P. J.; Laurenczy, G.; Ludwig, R.; Beller, M. *Science* **2011**, *333*, 1733-1736. (c) Hull, J. F.; Himeda, Y.; Wang, W.-H.; Hashiguchi, B.; Periana, R.; Szalda. D. J.; Muckerman, J. T.; Fujita, E. *Nat. Chem.* **2012**, *4*, 383-388. (d) Mellmann, D.; Sponholz, P.; Junge, H.; Beller, M. *Chem. Soc. Rev*. **2016**, *45*, 3954-3988.

(6) (a) Gu, X.; Lu, Z.-H.; Jiang, H.-L.; Akita, T.; Xu, Q. *J. Am. Chem. Soc.* **2011**, *133*, 11822-11825. (b) Jiang, K.; Xu, K.; Zou, S.; Cai, W.-B. *J. Am. Chem. Soc.* **2014**, *136*, 4861-4864. (c) Wang, N.; Sun, Q.; Bai, R.; Li, X.; Guo, G.; Yu, J. *J. Am. Chem. Soc*. **2016**, *138*, 7484-7487. (d) Li, Z.; Xu, Q. *Acc. Chem. Res.* **2017**, *50*, 1449-1458.

(7) (a) He, L.; Weniger, F.; Neumann, H.; Beller, M. *Angew. Chem. Int. Ed.* **2016**, *55*, 12582-12594. (b) Liu, B; Yao, H.; Song, W.; Jin, L.; Mosa, I. M.; Rusling, J. F.; Suib, S. L.; He, J. *J. Am. Chem. Soc*. **2016**, *138*, 4718-4721. (c) Bi, Q.-Y.; Lin, J.-D.; Liu, Y.-M.; He, H.-Y.; Huang, F.-Q.; Cao, Y. *Angew. Chem. Int. Ed.* **2016**, *55*, 11849-11853. (d) Li, Z.; Yang, X.; Tsumori, N.; Liu, Z.; Himeda, Y.; Autrey, T.; Xu, Q. *ACS Catal*. **2017**, *7*, 2720-2724.

(8) (a) Eppinger, J.; Huang, K.-W. *ACS Energy Lett.* **2017**, *2*, 118-195. (b) Sordakis, K.; Tang, C.; Vogt, L. K.; Junge, H.; Dyson, P. J.; Beller, M.; Laurenczy, G. *Chem. Rev.* **2018**, *118*, 372-433. (c) Onishi, N.; Laurenczy, G.; Beller, M.; Himeda, Y. *Coord. Chem. Rev*. **2018**, *373*, 317-332. (d) Iglesias, M.; Oro, L. A. *Eur. J. Inorg. Chem*. **2018**, *20-21*, 2125-

2138.

(9) (a) Parlett, C. M. A.; Wilson, K.; Lee, A. F. *Chem. Soc. Rev.* **2013**, *42*, 3876-3893. (b) Chen, S.; Qiao, S.-Z. *ACS Nano* **2013**, *7*, 10190-10196. (c) Sun, L.-B.; Liu, X.-Q.; Zhou, H.-C. *Chem. Soc. Rev.* **2015**, *44*, 5092-5147. (d) Sun, M.-H.; Huang, S.-Z.; Chen, L.-H.; Li, Y.; Yang, X.-Y.; Yuan, Z.-Y.; Su, B.-L. *Chem. Soc. Rev*. **2016**, *45*, 3479-3563.

(10) (a) Liu, B.; Shioyama, H.; Akita, T.; Xu, Q. *J. Am. Chem. Soc.* **2008**, *130*, 5390-5391. (b) Chaikittisilp, W.; Ariga, K.; Yamauchi, Y. *J. Mater. Chem. A* **2013**, *1*, 14-19. (c) Shen, K.; Chen, X.; Chen, J.; Li, Y. *ACS Catal.* **2016**, *6*, 5887-5903. (d) Chen, Y.-Z.; Cai, G.; Wang, Y.; Xu, Q.; Yu, S.-H.; Jiang, H.-L. *Green Chem.* **2016**, *18*, 1212-1217.

(11) (a) Zhai, Y.; Dou, Y.; Zhao, D.; Fulvio, P. F.; Mayes, R. T.; Dai, S. *Adv. Mater.* **2011**, *23*, 4828-4850. (b) Wang, J.; Kaskel, S. *J. Mater. Chem.* **2012**, *22*, 23710-23725. (c) Amali, A. J.; Sun, J.-K.; Xu, Q. *Chem. Commun.* **2014**, *50*, 1519-1522.

(12) Hartmann, M.; Fischer, M. *Micropor. Mesopor. Mater*. **2012**, *164*, 38-43.

(13) Chen, Y.; Zhu, Q.-L.; Tsumori, N.; Xu, Q. *J. Am. Chem. Soc.* **2015**, *137*, 106-109.

(14) Bulut, A.; Yurderi, M.; Karatas, Y.; Zahmakiran, M.; Kivrak, H.; Gulcan, M.; Kaya, M. *Appl. Catal. B: Environ.* **2015**, *164*, 324-333.

(15) Akbayrak, S.; Tonbul, Y.; Özkar, S. *Appl. Catal. B: Environ.* **2017**, *206*, 384-392.

(16) Wang, Z.; Hao, X.; Hu, D.; Li, L.; Song, X.; Zhang, W.; Jia, M. *Catal. Sci. Technol.* **2017**, *7*, 2213-2220.

(17) Sun, Q.; Wang, N.; Bing, Q.; Si, R.; Liu, J.; Bai, R.; Zhang, P.; Jia, M.; Yu, J. *Chem* **2017**, *3*, 477-493.

(18) Jin, M.-H.; Park, J.-H.; Oh, D.; Lee, S.-W.; Park, J.-S.; Lee, K.-Y.; Lee, D.-W. *Int. J. Hydrogen Energy* **2018**, *43*, 1451-1458.

(19) Lv, Q.; Meng, Q.; Liu, W.; Sun, N.; Jiang, K.; Ma, L.; Peng, Z.; Cai, W.; Liu, C.; Ge,

J.; Liu, L.; Xing, W. *J. Phys. Chem. C* **2018**, *122*, 2081-2088.

(20) Song, F.-Z.; Zhu, Q.-L.; Yang, X.; Zhan, W.-W.; Pachfule, P.; Tsumori, N.; Xu, Q. *Adv. Energy Mater*. **2018**, *8*, 1701416.

Chapter 3

Phosphate-Mediated Immobilization of High-Performance AuPd Nanoparticles for Dehydrogenation of Formic Acid at Room Temperature

Dehydrogenation of formic acid (FA) is a promising route to provide clean energy instead of fossil fuels for future energy economy. Synthesis of highly active catalysts for FA dehydrogenation at room temperature has attracted lots of attention. Herein, for the first time, highly active aurum-palladium nanoparticles (AuPd NPs) immobilized on a nitrogen (N)-doped porous carbon are fabricated through a phosphate-mediation approach. The N-doped carbon anchored with phosphate, which can be removed in the alkaline solution during the reduction process of metal ions, shows an enhanced performance of absorbing and dispersion of both Au and Pd ions, which is a key to the synthesis of highly-dispersed ultrafine AuPd NPs. The as-prepared catalyst (designated as Au_2Pd_3@(P)N-C) exhibits an extraordinarily high turnover frequency (TOF) of 5400 h^{-1} and a 100% H_2 selectivity for FA dehydrogenation at 30 °C. This phosphate-mediation approach provides a new way to fabricate highly active metal NPs for catalytic application, pushing heterogeneous catalysts forward the practical usage in energy storage and conversion.

3.1 introduction

Formic acid (FA) with a high volumetric capacity of 53 g H_2/L, showing a great potential as a safe and efficient carrier for hydrogen, can be completely decomposed into hydrogen

and carbon dioxide ($HCOOH \rightarrow H_2 + CO_2$, $\Delta G_{298\ K}$ = -48.8 kJ mol^{-1}),[1] while the production of H_2 from FA at mild conditions requires efficient catalysts.[2] Although homogeneous catalysts show a remarkable catalytic performance, the difficulty of separation from reactants drives researchers to seek efficient heterogeneous catalysts.[3] Among them, metal NPs have been studied extensively due to their high catalytic activities in abundant reactions caused by their high surface-to-volume ratio.[4]

Pd[5] and Au[6] are the most active noble metal catalysts used for FA dehydrogenation. Compared with the monometallic NPs, bimetallic AuPd NPs with surface electronic charge redistributions in nanoscale are demonstrated to be more efficient and stable during reactions.[7] However, isolated metal NPs in small sizes turn to aggregate during catalysis, leading to a deterioration of catalytic performance. To solve this problem, various supports, including metal oxides, metal-organic composites, graphene and porous carbons, have been introduced to disperse metal NPs, decrease their particle sizes, and prevent their aggregation during synthesis and catalysis.[8] Among them, porous carbon nanostructures, especially those derived from metal-organic frameworks (MOFs), have been studied extensively owing to their tunable porous structures, high specific surface areas and feasibilities of compositions tailoring.[9] It is proved that the doped heteroatomic species on carbon supports can enhance the dispersibility of metal NPs.[10] However, heteroatoms have different affinities to different metal ions.[11] For example, nitrogen (N)-doped carbons have been widely used for optimizing the immobilization of Pd NPs,[12] while we have found that it is not sufficient for the uniform dispersion of Au during synthesis of AuPd NPs (*vide infra*). The synthesis of bimetallic AuPd NPs with a uniform dispersion and nanoscale precision on supports is a challenge.

Herein, we develop a phosphate-mediation approach to prepare a highly active AuPd nanocatalyst for FA dehydrogenation. The hydrothermal reaction of N-doped carbon with phosphoric acid (H_3PO_4) produces a carbon support anchored with phosphate, which shows an enhanced performance for absorbing and dispersing both Au and Pd ions. The reduction of metal ions in the alkaline solution leads to the removal of phosphate and the formation of uniformly dispersed ultrafine bimetallic AuPd NPs with a close contact with carbon. The as-prepared catalyst (Au_2Pd_3@(P)N-C) exhibits an extraordinarily high catalytic activity for FA dehydrogenation at low temperatures, showing a TOF value as high as 5400 h^{-1} at 30 °C and even a high TOF value of 1964 h^{-1} at 10 °C.

The synthesis process of Au_2Pd_3@(P)N-C is illustrated in Figure 3.1. Firstly, zeolitic imidazolate framework-8 (ZIF-8)[13] was prepared by mixing methanol solutions of 2-methylimidazole (2-Melm) and zinc nitrate hexahydrate ($Zn(NO_3)_2 \cdot 6H_2O$) together with stirring for 24 h (Figure 3.2a). With a carbonization at 1000 °C for 2 h under argon (Ar) flow and a subsequent acid etching, a N-doped porous carbon was obtained (designated as N-C). The hydrothermal process of N-C with H_3PO_4 at 130 °C for 12 hours resulted in a phosphate-anchored carbon (designated as PN-C), on which Au and Pd ion precursors are highly dispersed and uniformly anchored. The subsequent reduction process for metal ions in the alkaline solution removed the phosphate as well, achieving the highly dispersed ultrafine AuPd NPs on the carbon support (Au_2Pd_3@(P)N-C). The obtained catalyst was used for FA dehydrogenation.

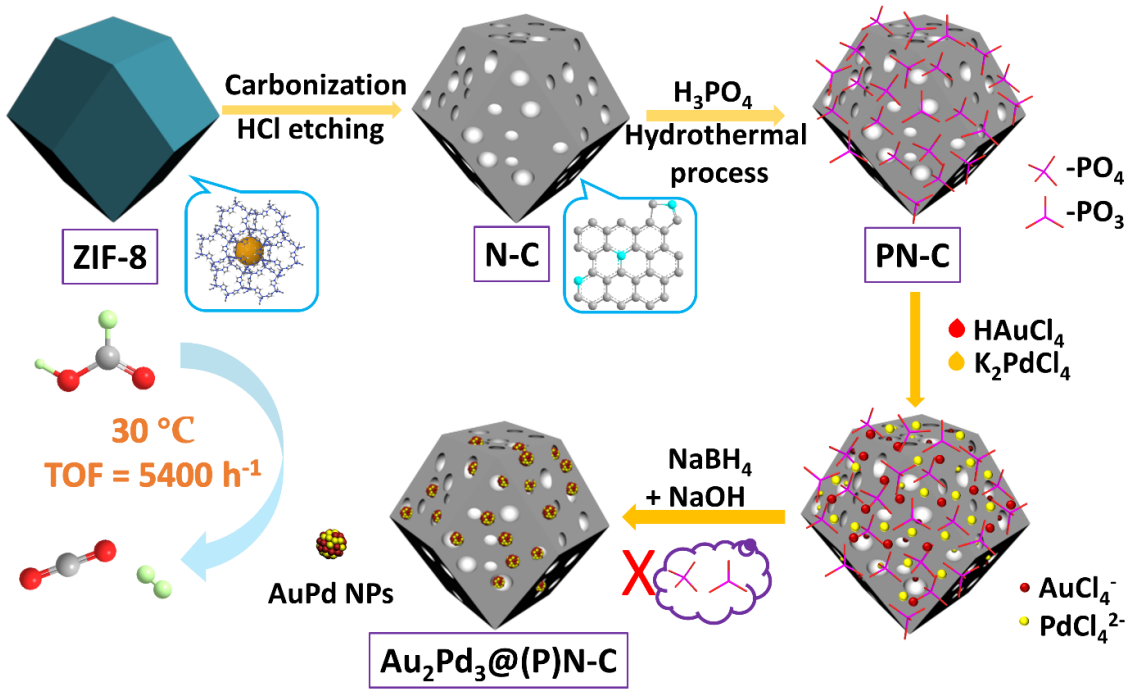

Figure 3.1. Schematic illustration of preparation of Au_2Pd_3@(P)N-C nanocatalyst.

3.2 Experimental section

3.2.1 Chemicals

All chemicals were commercially available and used without further purification. Zinc nitrate hexahydrate ($Zn(NO_3)_2 \cdot 6H_2O$, Wako Pure Chemical Industries, ≥99.0%), 2-methylimidazole (Tokyo Chemical Industry Co., >97%), methanol (Kishida Chem. Co., 99.8%), hydrochloric acid (HCl, Wako Pure Chemical Industries, 35-37%), phosphoric acid (H_3PO_4, Tokyo Chemical Industry Co., Ltd., 89.0%), sodium metaphosphate ($(NaPO_3)_n$, Wako Pure Chemical Industries, 65-70% (as P_2O_5)), ammonium phosphate dibasic ($(NH_4)_2HPO_4$, Kishida Chem. Co., 99%), ammonium phosphate monobasic ($NH_4H_2PO_4$, Kishida Chem. Co., 99%), potassium tetrachloropalladate (K_2PdCl_4, Wako Pure Chemical Industries, 95%), hydrogen tetrachloroaurate tetrahydrate ($HAuCl_4 \cdot 4H_2O$, Wako Pure Chemical Industries, >95%), sodium hydroxide (NaOH, Kishida Chem. Co.,

97%), sodium borohyride ($NaBH_4$, Sigma-Aldrich, 99%), formic acid (FA, HCOOH, Kishida Chem. Co., >98.0%), sodium formate dehydrate (SF, HCOONa, Tokyo Chemical Industry Co., Ltd., >95.0%), Maxsorb MSP-20X (Nanoporous Carbon, Kansai Coke and Chemicals Co. Ltd.), urea (Tokyo Chemical Industry Co., Ltd., >99.0%), tetrabutylammonium dihydrogenphosphate solution (Tokyo Chemical Industry Co., Ltd., 0.5 mol/L) and dimethylamine-borane (DMAB, Wako Pure Chemical Industries, >97.0%) were used as received. De-ionized (DI) water with a specific resistance of 18.2 MΩ·cm was obtained by reverse osmosis followed by ion-exchange and filtration (RFD 250NB, Toyo Seisakusho Kaisha, Ltd., Japan).

3.2.2 Instrumentation and methods

Laboratory powder X-ray diffraction (XRD) patterns were collected for the samples on a Rigaku Ultima IV X-ray diffractometer with Cu Kα source (40 kV, 40 mA). The N_2 adsorption/desorption isotherms were obtained at 77 K using automatic volumetric adsorption equipment (Belsorp-max). The metal contents of the catalyst were analyzed using inductively coupled plasma optical emission spectroscopy (ICP-OES) on Thermo Scientific iCAP6300. XPS spectra were recorded on a Shimadzu ESCA-3400 using an Mg Kα source. The transmission electron microscopic (TEM) and high-annular dark-field scanning TEM (HAADF-STEM) images were collected on TECNAI G^2 F20 transmission electron microscope with operating voltage at 200 kV. EDS mapping analyses of the carbon were recorded on a Titan3 G2 60-300 (FEI) with a Super-X EDS system (Bruker) under operating voltages of 300 kV. HAADF images and EDS mappings of catalysts were taken at room temperature by using a JEM-ARM200F ACCELARM (cold FEG) equipped with a CEOS ASCOR corrector and SDD (100 mm^2) operated at 120 kV. Elemental analyses were performed on CE EA1110 and Perkinelmer 2400II instruments.

After purging the reactor with nitrogen for three times, the decomposition of formic acid was carried out, and the generated gas was collected, which was analyzed by GC-8A (molecular sieve 5A, Ar as carrier gas) and GC-8A (Porapack N, He as carrier gas) analyzers (Shimadzu). UV-Vis spectra were collected on Shimazu UV-2550 spectrophotometer.

3.2.3 Syntheses of materials

3.2.3.1 Syntheses of supports

(1) Synthesis of ZIF-8

ZIF-8 was prepared at room temperature via mixing 500 mL methanol solution of $Zn(NO_3)_2 \cdot 6H_2O$ (10.50 g, 35 mmol) with 500 mL methanol solution of 2-methylimidazole (23.078 g, 290 mmol) and stirring for 24 h. The product was then centrifuged from the mixture and immersed into fresh methanol for solvent exchange for 3 days. Fresh methanol was changed for everyday and the final product was dried in the vacuum oven at 80 °C overnight.

(2) Synthesis of N-C

As-prepared ZIF-8 (0.8 g) was transferred into a ceramic boat and placed in a temperature-programed furnace under an argon (Ar) atmosphere. Temperature was raised to 1000 °C in 5 h and kept at the temperature for another 2 h. After cooling down to room temperature naturally, the composite was immersed into 10 vol% HCl solution with stirring for 3 days to remove the residual Zn or/and ZnO. The sample was then washed by DI water for 3 times and dried at 60 °C in the oven (designated as N-C).

(3) Synthesis of PN-C

PN-C was prepared by the following procedure: 100 mg as-prepared N-C was mixed with 5 mL H_2O and 1 mL concentrated H_3PO_4 with sonication for 0.5 h. Then the mixture was

transferred into a 15 mL autoclave and placed into a programming oven with heating at 130 °C for 12 h. After cooling down to room temperature, the sample was centrifuged from the mixture and washed 3 times by DI water. The obtained material (designated as PN-C) was used as a support for the preparation of metal nanocatalyst without drying.

(4) Syntheses of PN-C1 and PN-C2

PN-C1 and PN-C2 were prepared by the same hydrothermal procedure as PN-C except for using $NH_4H_2PO_4$ and $(NH_4)_2HPO_4$ (keep the same amount of P as H_3PO_4) instead of H_3PO_4, respectively. After the hydrothermal process, PN-C1 and PN-C2 were washed by DI water for 3 times and used as supports without drying.

(5) Syntheses of N-MSP, P-MSP, and PN-MSP

a. 0.5 g MSP-20X (designated as MSP) and 0.3 g urea were mixed together with grinding until a homogeneous mixture was achieved. The mixture was transferred to a ceramic crucible and heated in a muffle furnace at 300 °C for 2 h. After cooling to room temperature, the mixture was washed with DI water for 3 times and dried at 60 ° C overnight. The sample was denoted as N-MSP.

b. 100 mg as-prepared N-MSP was used for P grafting by the same procedure as PN-C. The sample was denoted as PN-MSP.

c. 100 mg MSP was used for P grafting by the same procedure as PN-C. The sample was denoted as P-MSP.

3.2.3.2 Syntheses of catalysts

(1) Syntheses of Au_xPd_y@(P)N-C catalysts

PN-C (~100 mg) was dispersed into DI water to form a 5 mL dispersion and then the aqueous solutions of x mmol $HAuCl_4$ (x = 0, 0.01, 0.02, 0.03, 0.04 and 0.05 mmol, C_{Au} = 0.05 M) and y mmol K_2PdCl_4 (y = 0.05-x mmol; C_{Pd} = 0.1 M) were added with shaking

for 1 h. A subsequent addition of 50 mg $NaBH_4$ dissolved in 1 mL NaOH (3 M) aqueous solution was followed and the mixture was continued to shake for another 1 h. After the metal ions were reduced completely, the catalyst was washed by DI water for 3 times and used for FA dehydrogenation.

(2) Syntheses of control samples (Au_2Pd_3@N-C, Au_2Pd_3@(P)N-C1, Au_2Pd_3@(P)N-C2, Au_2Pd_3@MSP, Au_2Pd_3@N-MSP, Au_2Pd_3@(P)-MSP and Au_2Pd_3@(P)N-MSP).

100 mg N-C, PN-C1, PN-C2, MSP, N-MSP, P-MSP and PN-MSP were used as supports to prepare the catalysts via the same procedure as Au_2Pd_3@(P)N-C. The as-prepared catalysts were used as the control samples for FA dehydrogenation.

(3) Synthesis of Au_2Pd_3/N-C-hydrogenphosphate catalyst.

Au_2Pd_3/N-C-hydrogenphosphate catalyst was prepared according to Ref. 16. The process is as follows: 0.02 mmol $HAuCl_4$ (0.05 M×0.4 mL), 0.03 mmol K_2PdCl_4 (0.1 M×0.3 mL) and 1 mmol tetrabutylammonium dihydrogenphosphate (0.5 M×2 mL) were added into 15 mL H_2O with stirring for 0.5 h. Then 100 mg N-C was added into the mixture with stirring for another 0.5 h. 7.5 mL of dimethylamine-borane solution (n_{DMAB} = 2.5 mmol) was added continuously into the reactants and stirred until no more gas was released. Finally, the catalyst was centrifuged and washed by DI water for 3 times, and then used for FA dehydrogenation.

(4) Synthesis of AuPd/ZIF-8 catalyst.

AuPd/ZIF-8 catalyst was prepared by the following process: ZIF-8 (100 mg) was dispersed into 5 mL of methanol and then the aqueous solutions of $HAuCl_4$ (0.05 M×0.4 mL) and K_2PdCl_4 (0.1 M×0.3 mL) were added with shaking for 1 h. Then 50 mg $NaBH_4$ dissolved in 1 mL of NaOH solution (3 M) was added and the mixture was shaken for another 1 h. After the metal ions were reduced completely, the catalyst was washed by

fresh methanol for 3 times and used for FA dehydrogenation.

3.2.4 UV-Vis measurements

3.2.4.1 UV-Vis measurements for aqueous solution of $HAuCl_4$, K_2PdCl_4, and the mixture of $HAuCl_4$ and K_2PdCl_4 with different additions.

Solution a: H_3PO_4 solution was prepared by adding 1 mL H_3PO_4 into 5 mL H_2O.

Solution b: H_3PO_4-130 solution was prepared by adding 1 mL H_3PO_4 into 5 mL H_2O and heated at 130 °C for 12 h in the autoclave.

Solution c: $(NaPO_3)_n$ solution was prepared by adding $(NaPO_3)_n$ (with the same P content as Solution *a* and *b*) into 5 mL H_2O.

Solution d: blank sample is the DI water.

Solution e: $HAuCl_4$ (0.4 mL × 0.05 M) was added into the 5 mL H_2O.

Solution f: K_2PdCl_4 (0.3 mL × 0.1 M) was added into the 5 mL H_2O.

Solution g: the mixture of $HAuCl_4$ (0.4 mL × 0.05 M) and K_2PdCl_4 (0.3 mL × 0.1 M) was added into the 5 mL H_2O.

0.2 mL solution *a* (*b*, *c* and *d*) was added into solution *e*, *f* and g, respectively, to form 12 samples. After being mixed completely, 0.1 mL above solutions were diluted with 3 mL H_2O and used for the UV-Vis measurements.

3.2.4.2 The absorbance ability measurements of N-C and PN-C for $HAuCl_4$ and K_2PdCl_4

10 mg sample (N-C and PN-C) was dispersed into 5 mL H_2O and added with aqueous solution of $HAuCl_4$ and K_2PdCl_4 ($n_{Au}/n_{Pd} = 2/3$, $n_{Au+Pd} = 0.02$ mmol). After shaken for 0.5 h, the mixtures were centrifuged, and the supernatants were diluted to 30 times for the UV-Vis measurements.

3.2.5 Catalytic activity characterization

3.2.5.1 Procedure for FA dehydrogenation

Reaction apparatus for measuring the H_2+CO_2 evolution form FA/SF system is as the same as previously reported.[2c] In general, a 2 mL dispersion of as-prepared catalyst and water was placed in 30 mL two-necked round-bottom flask which was placed in a water bath at a preset temperature (10, 20, 30, 40 and 50 °C). A gas burette filled with water was connected to the reaction flask to measure the volume of released gas (temperature kept constant at 298 K during measurement). The reaction started when 1.0 mL of mixed aqueous solution containing FA (3 M) and SF of different molar ratios (0, 3, 6, 7.5 and 9 M) was injected into the mixture using a syringe. The molar ratio of n_{Au+Pd}/n_{FA} was theoretically fixed at 0.017 for all the catalytic reactions. The volume of the evolved gas was monitored by recording the displacement of water in the gas burette.

3.2.5.2 Durability testing of Au_2Pd_3@(P)N-C

The durability testing of Au_2Pd_3@(P)N-C was performed at 30 °C. The procedure was the same as described in 3.2.5.1. After each run, the catalyst was seperated from the system and washed 3 times by DI water. Then the catalyst was reused for next cycle. For each cycle, 1.0 mL of FA/SF solution (3M/7.5 M) was injected to the catalysis system. The experiment was repeated for 10 times.

3.2.5.3 Control experiments

Control samples (Au_2Pd_3@N-C, Au_2Pd_3@(P)N-C1, Au_2Pd_3@(P)N-C2, Au_2Pd_3@MSP, Au_2Pd_3@N-MSP, Au_2Pd_3@(P)-MSP and Au_2Pd_3@(P)N-MSP) were employed as catalysts for the decomposition of 1 mL of FA/SF solution (3M/7.5M) at 30 °C for comparison.

3.2.6 Calculation methods

The turnover frequency (TOF) reported here is an apparent TOF value based on the

number of metal atoms in catalyst, which is calculated from the equation as follow:

$$TOF = P_0V/(2RTn_Mt)$$

Where P_0 is the atmospheric pressure (101325 Pa), V is the final generated volume of (H_2+CO_2) gas, R is the universal gas constant (8.3145 m^3 Pa mol^{-1} K^{-1}), T is the room temperature (298 K), n_M is the total mole number of Au and Pd atoms in catalysts and t is the completion time of the reaction in hour.

3.3 Result and discussion

3.3.1 Characterization

Powder X-ray diffraction (PXRD) patterns in Figure 3.2a show the successful preparation of ZIF-8. XRD patterns of N-C and PN-C (Figure 3.2b) show two typical diffraction peaks at 24.7 and 44° for carbon. Au_2Pd_3@(P)N-C displays a wide diffraction peak with a low intensity between 36 and 40°, which belongs to AuPd NPs of small sizes.

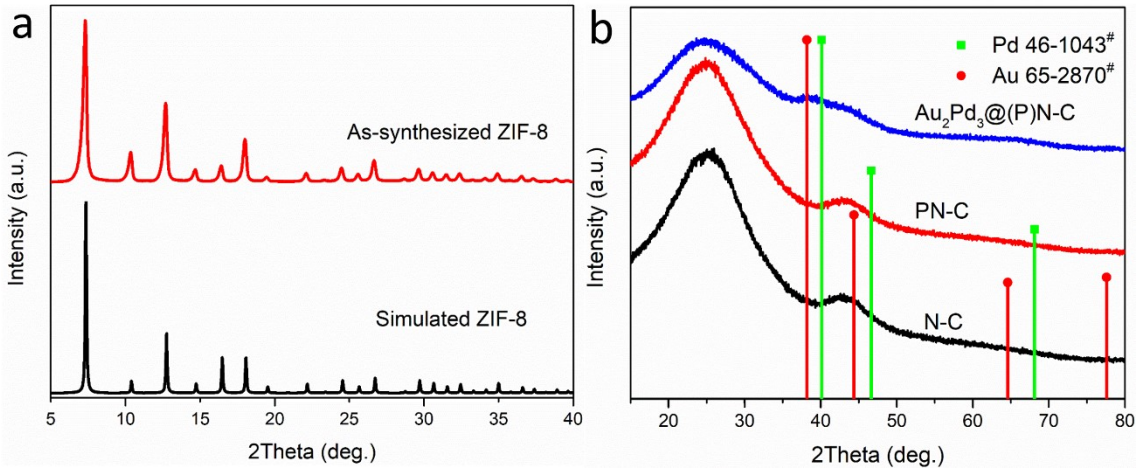

Figure 3.2. XRD patterns of (a) as-prepared and the simulated ZIF-8, and (b) N-C, PN-C and Au_2Pd_3@(P)N-C.

According to the N_2 sorption isotherms, ZIF-8 (S_{BET} = 1382 m^2 g^{-1}, V_{pore} = 0.84 cm^3 g^{-1}) is transferred into a hierarchically porous carbon N-C (S_{BET} = 1024 m^2 g^{-1}, V_{pore} = 1.01

cm^3 g^{-1}) with micropores centered at 1.5 nm and mesopores centered at ~30 nm (calculated based on the NLDFT method). The hierarchical pores are retained after P species anchoring (S_{BET} = 1098 m^2 g^{-1}, V_{pore} = 1.04 cm^3 g^{-1}). Au_2Pd_3@(P)N-C (S_{BET} = 779 m^2 g^{-1}, V_{pore} = 0.78 cm^3 g^{-1}) shows a decrease in the BET specific surface area and pore volume due to the immobilization of AuPd NPs (Figure 3.3 and Table 3.1). The hierarchically porous structure of the catalysts facilitates the diffusion of reactants and products during the reaction, which improves the catalytic performance.

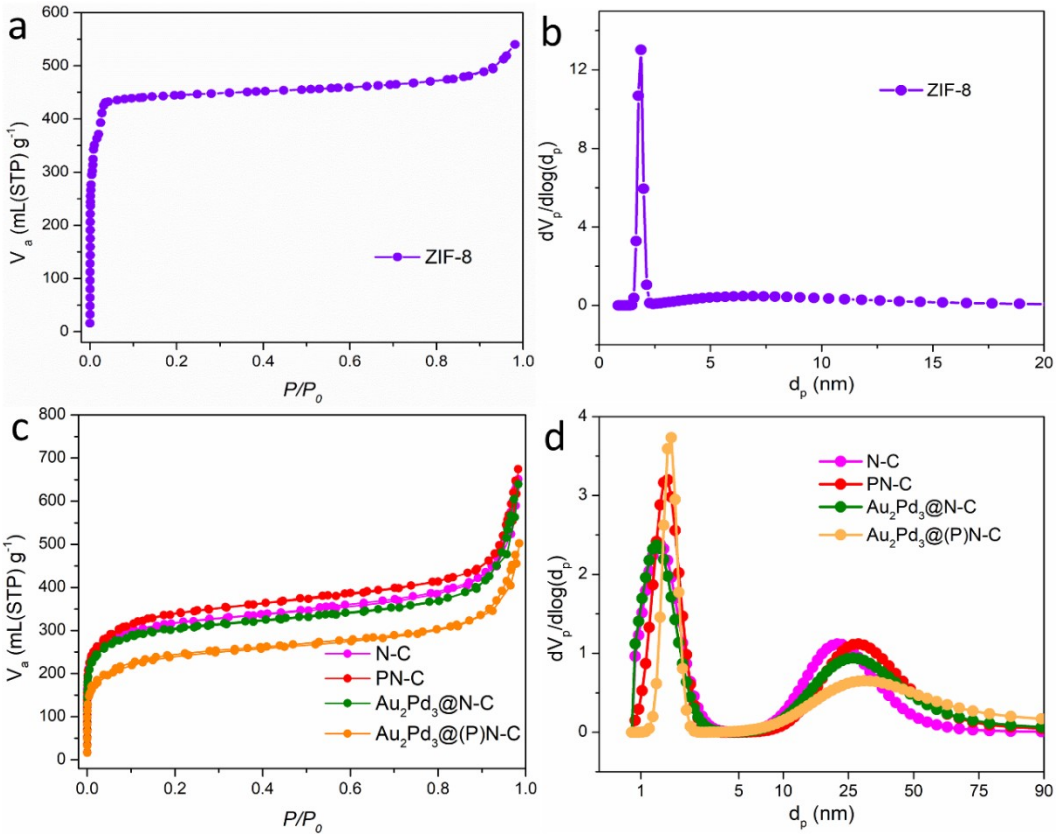

Figure 3.3. N_2 sorption isotherms (77 K) and the corresponding pore size distributions calculated using NLDFT method of (a, b) ZIF-8, and (c, d) N-C, PN-C, Au_2Pd_3@N-C and Au_2Pd_3@(P)N-C.

Table 3.1. BET specific surface areas and pore volumes of the as-synthesized carbons and catalysts.

Sample	BET surface area ($m^2 g^{-1}$)	Total pore volume ($cm^3 g^{-1}$)
ZIF-8	1382	0.84
N-C	1024	1.01
PN-C	1098	1.14
Au_2Pd_3@N-C	974	0.99
Au_2Pd_3@(P)N-C	779	0.78

Table 3.2. Content of N and P of as-prepared samples

Sample	N content (wt%)	P content (wt%)
N-C	4.03	-
PN-C	4.38	1.4
Au_2Pd_3@(P)N-C	4.34	0.055
PN-C1	-	1.1
PN-C2	-	0.52

Elemental analysis confirms the existence of N in N-C, PN-C and Au_2Pd_3@(P)N-C (Table 3.2). The P species was successfully anchored on PN-C with a P content of 1.4 wt%, which is detected by the inductively coupled plasma-optical emission spectroscopy (ICP-OES) analysis (Table 3.2). However, the P content decreased to 0.055 wt% after the immobilization of AuPd NPs, suggesting the removal of P species during the reduction of metal ions in the alkaline solution. Au_2Pd_3@(P)N-C has a Au content of 3.4 wt% and Pd content of 2.8 wt %, consistent with the theoretical metal contents (Au 3.7 wt%; Pd 3.0 wt%).

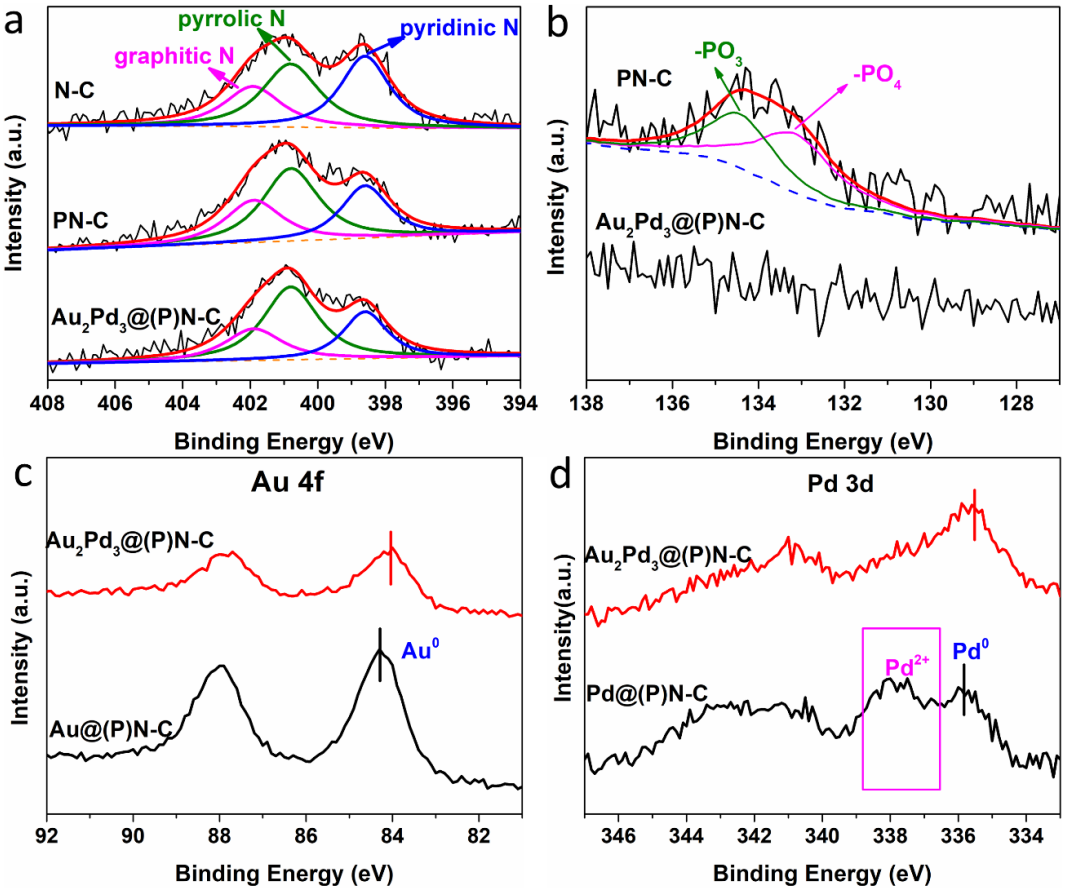

Figure 3.4. (a) N 1s XPS spectra of N-C, PN-C and Au_2Pd_3@(P)N-C; (b) P 2p XPS spectra of PN-C and Au_2Pd_3@(P)N-C; (c) Au 4f XPS spectra of Au_2Pd_3@(P)N-C and Au@(P)N-C; (d) Pd 3d XPS spectra of Au_2Pd_3@(P)N-C and Pd@(P)N-C.

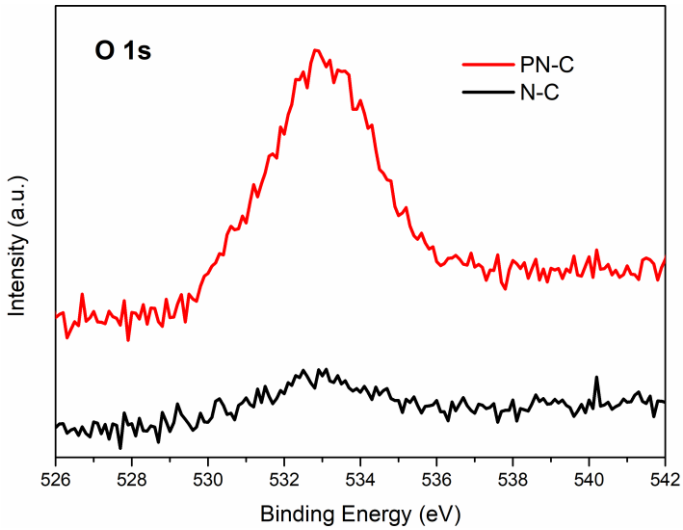

Figure 3.5. O1s XPS spectra of PN-C and N-C.

X-ray photoelectron spectroscopic (XPS) analysis further confirms the chemical status and elemental compositions on the surface of samples. The N 1s spectra of N-C, PN-C and Au_2Pd_3@(P)N-C can be deconvoluted into three peaks at binding energies of 398.6, 400.8, and 401.9 eV, which are assigned to pyridinic, pyrrolic, and graphitic N, respectively (Figure 3.4a). An obvious P 2p peak appears at binding energy of ~134 eV in PN-C, which can be deconvoluted into two peaks assigned to phosphate (-PO_4, 133.2 eV) and metaphosphate (-PO_3, 134.5 eV) (Figure 3.4b). Generally, phosphoric acid can turn to pyrophosphoric acid and metaphosphoric acid at high temperatures (~300 °C).[14] During the hydrothermal process in our work, parts of phosphoric acid can turn to metaphosphoric acid and both of them attack the defects on the carbon, leaving the –PO_3 and –PO_4 on the surface.[15] This can be further confirmed by the XPS spectra of O 1s of carbons before and after the hydrothermal process with phosphoric acid as the intensity of O 1s peak increased dramatically after phosphate anchoring (Figure 3.5). Consistent with the ICP result, the P signal disappeared after the reduction of metal ions (Figure 3.4b). Compared to the monometallic catalysts of Au@(P)N-C and Pd@(P)N-C, the location of Au 4f and Pd 3d doublets of Au_2Pd_3@(P)N-C shift to a slightly lower binding energies, verifying the formation of AuPd alloy (Figure 3.4c and 3.4d). It is worth to mention that the addition of Au decreases the oxidation of Pd dramatically, confirming the stability of bimetallic AuPd NPs.

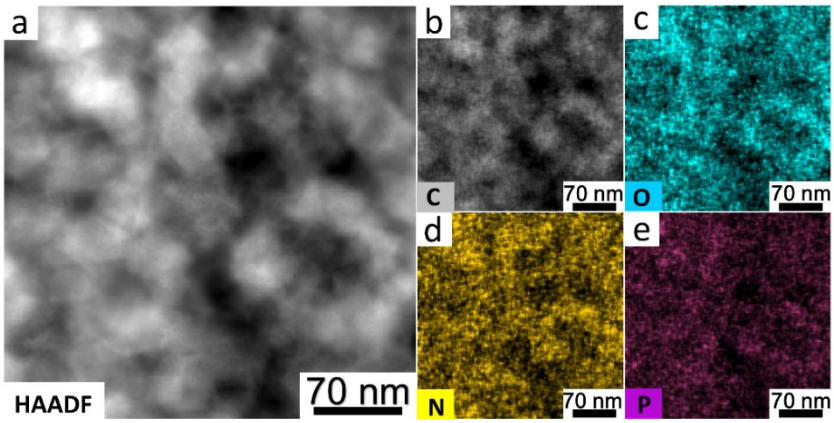

Figure 3.6. (a) HAADF-STEM and (b) the corresponding elemental mapping images of PN-C.

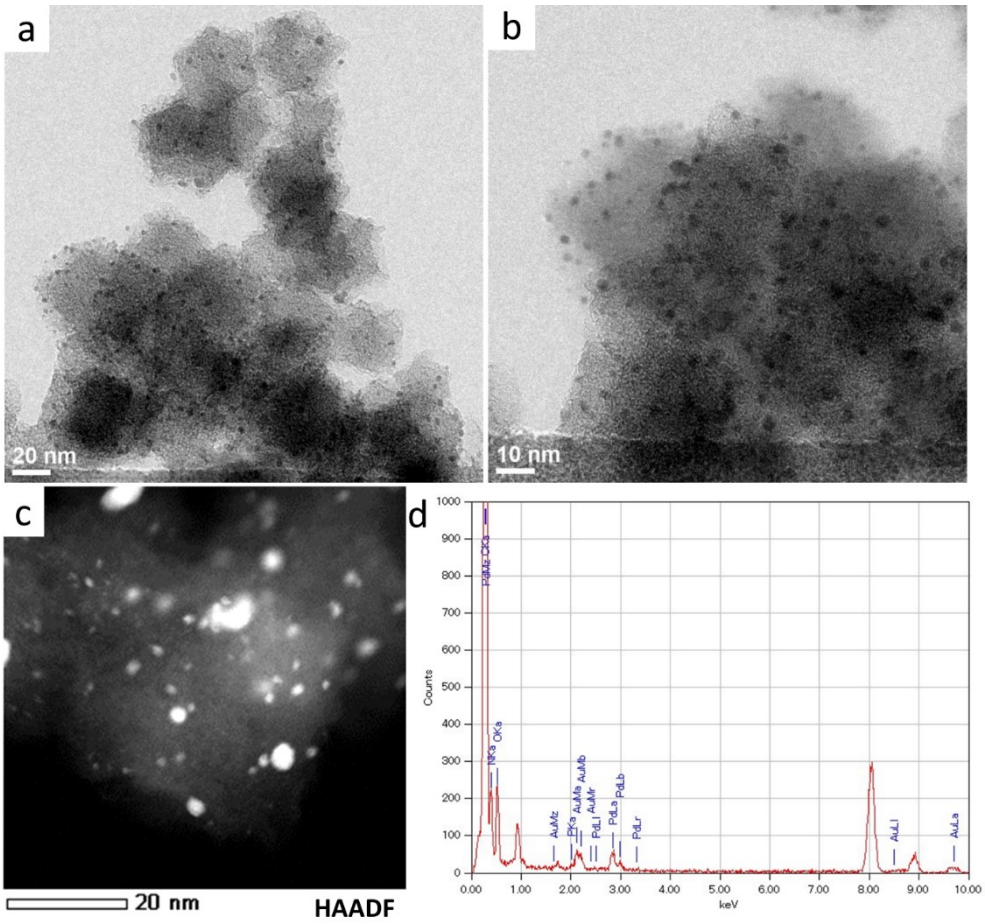

Figure 3.7. (a, b) TEM and (c) HAADF-STEM images, and (d) the corresponding EDS spectrum of Au_2Pd_3@(P)N-C.

High-angle annular dark-field scanning transmission electron microscopy (HAADF-STEM) and elemental mapping analyses reveal the uniform doping of N and P in PN-C (Figure 3.6). As shown in Figure 3.7 and Figure 3.8, Au_2Pd_3@(P)N-C possesses ultrafine AuPd NPs with a mean diameter of 1.5 ± 0.4 nm, which are uniformly dispersed on the carbon support.

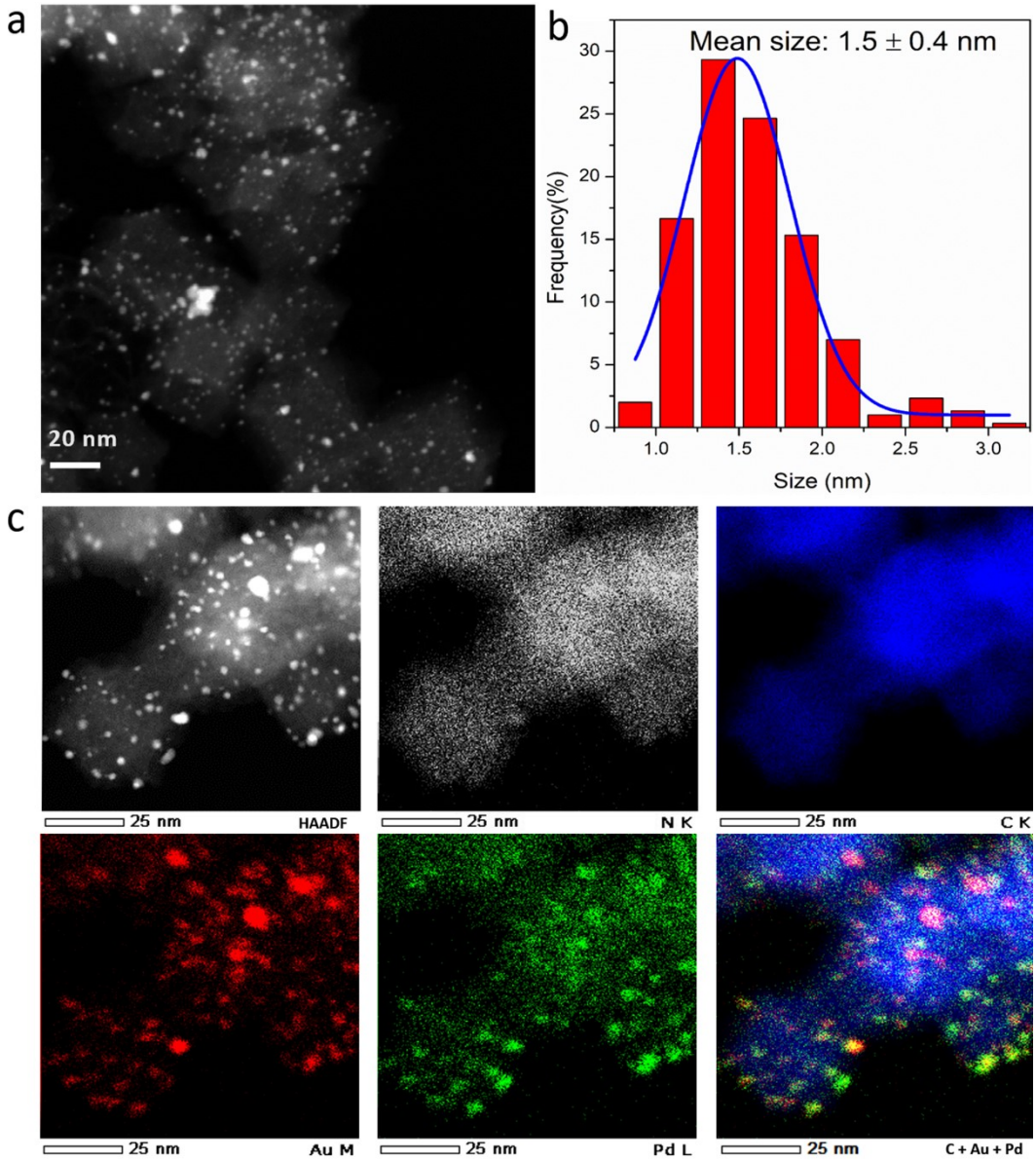

Figure 3.8. (a) HAADF-STEM image, (b) the corresponding particle size distribution of AuPd NPs, and (c) the elemental mapping images of Au_2Pd_3@(P)N-C.

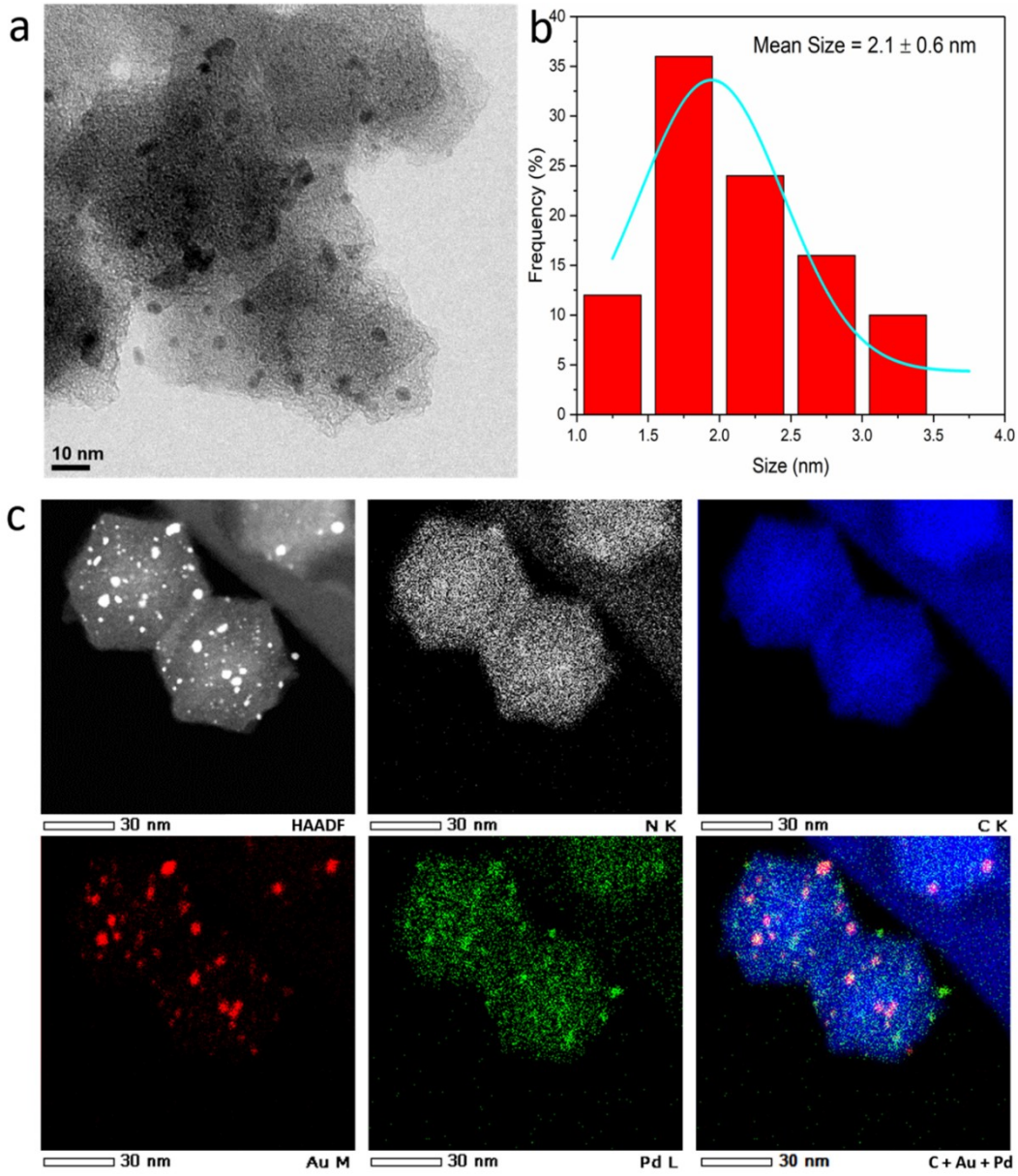

Figure 3.9. (a) TEM image, (b) the corresponding particle size distribution of AuPd NPs and (c) the elemental mapping images of Au_2Pd_3@N-C.

In contrast, without the P-mediation approach, the as-prepared Au_2Pd_3@N-C catalyst shows a larger particle size of 2.1 ± 0.6 nm with a poor dispersion of Au element on the carbon support (Figure 3.9). The better distribution of Au element in Au_2Pd_3@(P)N-C might be caused by the anchored phosphate on the carbon support, which provides a strong interaction with metal ions improving their dispersion. It is noted that the uniform

dispersion of both Pd and Au elements cannot be achieved on the carbon doped with only nitrogen (N). The phosphate were removed after reduction of metal ions in the alkaline solution according to energy dispersive X-ray spectrometry (EDS) analysis (Figure 3.7d), confirming that phosphate are intermediates for the dispersion of metal ions.

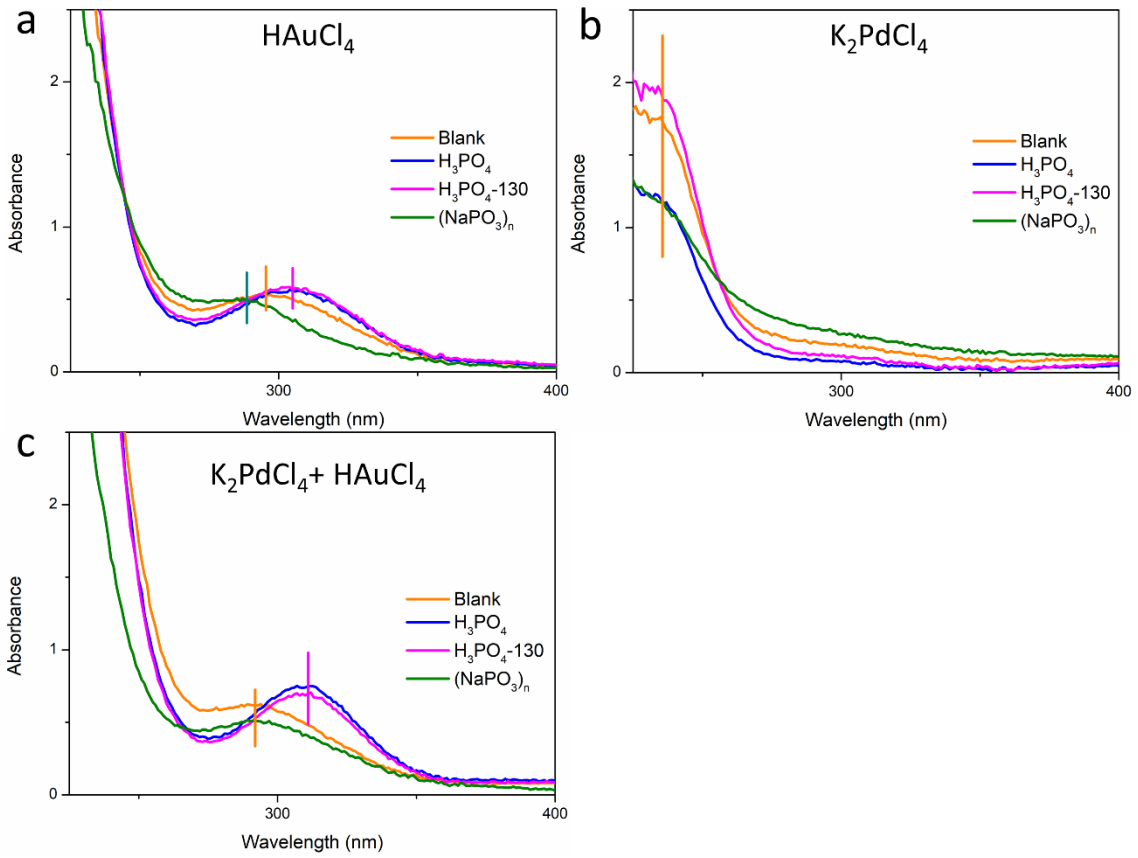

Figure 3.10. UV spectra of aqueous (a) $HAuCl_4$, (b) K_2PdCl_4 and (c) $HAuCl_4$ and K_2PdCl_4 solutions with addtion of DI water (Blank), H_3PO_4 solution (H_3PO_4), the reactant of hydrothermal process of H_3PO_4 solution at 130 °C (H_3PO_4-130) and $(NaPO_3)_n$ solution.

The interaction between phosphate and metal ions was further investigated by UV-Vis analysis. The H_3PO_4 solution, the H_3PO_4 solution after hydrothermal process at 130 °C, the $(NaPO_3)_n$ solution, and de-ionized (DI) water (designated as blank) were respectively added into the aqueous solutions of $HAuCl_4$, K_2PdCl_4 and the mixture of $HAuCl_4$ and

K_2PdCl_4. The UV-Vis spectra in Figure 3.10 shows that the addition of H_3PO_4, H_3PO_4-130 and $(NaPO_3)_n$ changed the original position absorbance peaks of $HAuCl_4$, implying an interaction between Au ions precursor and P groups (such as $-PO_4$ and $-PO_3$). Besides, PN-C shows a stronger absorbance ability for the mixture of $HAuCl_4$ and K_2PdCl_4 solution compared with N-C, further confirming the interaction between phosphate and metal ions (Figure 3.11).

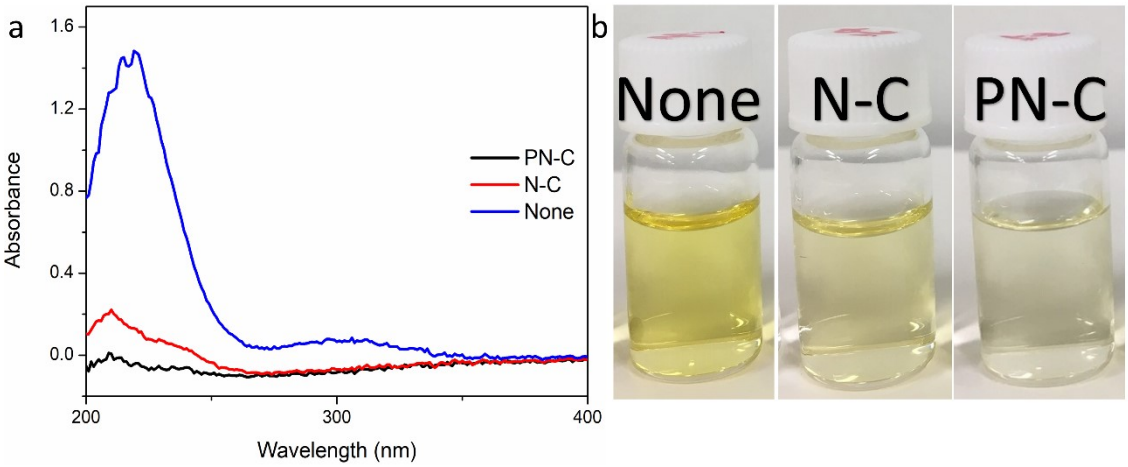

Figure 3.11. (a) Absorbance performances of different adsorbents for aqueous solution of $HAuCl_4$ and K_2PdCl_4 (n_{Au}/n_{Pd} = 2/3, n_{Au+Pd} = 2 mmol, m_{abs} = 10 mg) and (b) the corresponding photos of supernatants after absorbance.

3.3.2 Catalytic activity and durability

The catalytic activities of the as-prepared catalysts were evaluated by the hydrogen evolution from FA/SF solution. The performances of AuPd nanocatalysts with different n_{Au}/n_{Pd} ratios were firstly studied at a fixed condition (n_{Au+Pd}/n_{FA} = 0.017, n_{FA}/n_{SF} = 1/2.5, n_{FA} = 3 mmol; Figure 3.12). Au_2Pd_3@(P)N-C shows the best catalytic performance with a TOF value of 5400 h^{-1} at 30 °C, much better than those of present reported results (Table 3.3).

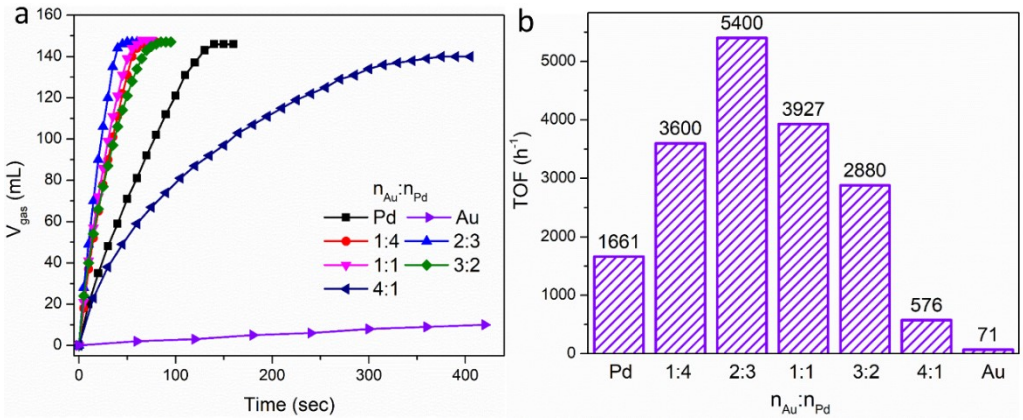

Figure 3.12. (a) Volume of the generated gas (CO_2 + H_2) *versus* time for FA dehydrogenation over Au_xPd_y@(P)N-C with different n_{Au}/n_{Pd} ratios and (b) the corresponding TOF values (n_{Au+Pd}/n_{FA} = 0.017, n_{FA}/n_{SF} = 1/2.5, n_{FA} = 3 mmol, 30 °C).

Table 3.3. Catalytic activities of the latest heterogeneous catalysts for dehydrogenation of formic acid.

Catalyst	Temp. (°C)	Additive	TOF (h^{-1})[a,*]	Ref.
Pd@CN900K	50	HCOONa	8000	[5c]
In situ-Pd@MSC	60	HCOONa	9110	[5d]
Au@Schiff-SiO_2	50	None	4368[b]	[6c]
AuPd–MnO_x/ZIF-8–rGO	25	None	382.1[b]	[7c]
$Pd_{0.5}Au_{0.3}Mn_{0.2}$/N-SiO_2	25	None	785[b]	[7e]
PdAg@ZrO_2/C/rGO	60	HCOONa	4500	[8e]
Pd-B/C	30	HCOONa	1184[b, #]	[10a]
Pd/CN0.25	25	None	5530[b,#]	[12d]
			275[b]	
NiPd/NH_2-N-rGO	25	None	954.3[b]	[12e]
Au_2Pd_3@(P)N-C	10	HCOONa	1964	This work
	20		3086	
	30		5400	
	40		8000	
	50		12000	
Au_2Pd_3@(P)N-C	30	None	358.3	This work

[a]*TOF values calculated on the completion time of gas releasing.*

[b]*Initial TOF values calculated on initial time or initial conversion of FA.*

[*]*TOF values calculated on total metal atoms.*

[#]*TOF values calculated on surface metal sites or active sites.*

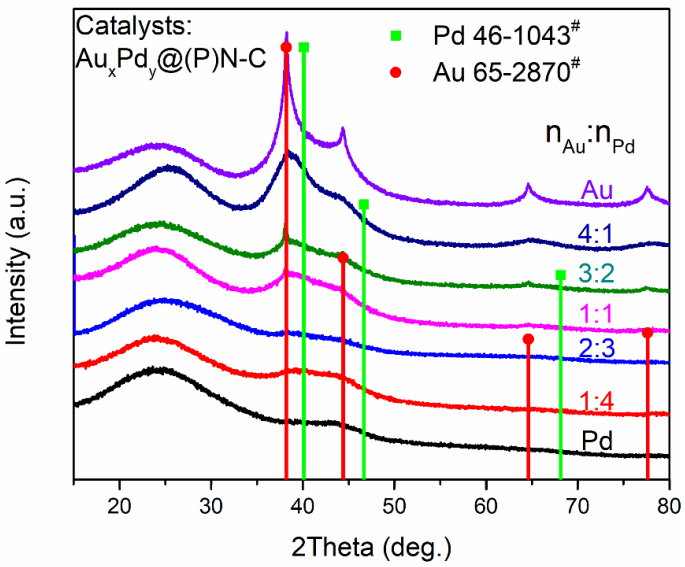

Figure 3.13. XRD patterns of as-synthesized Au_xPd_y@(P)N-C catalysts with different n_{Au}/n_{Pd} ratios.

The corresponding XRD patterns show that with the increase of Au content in AuPd nanocatalyst, diffraction peaks of Au become more intensive, which may be caused by the enrichment of monometallic particles (Figure 3.13).

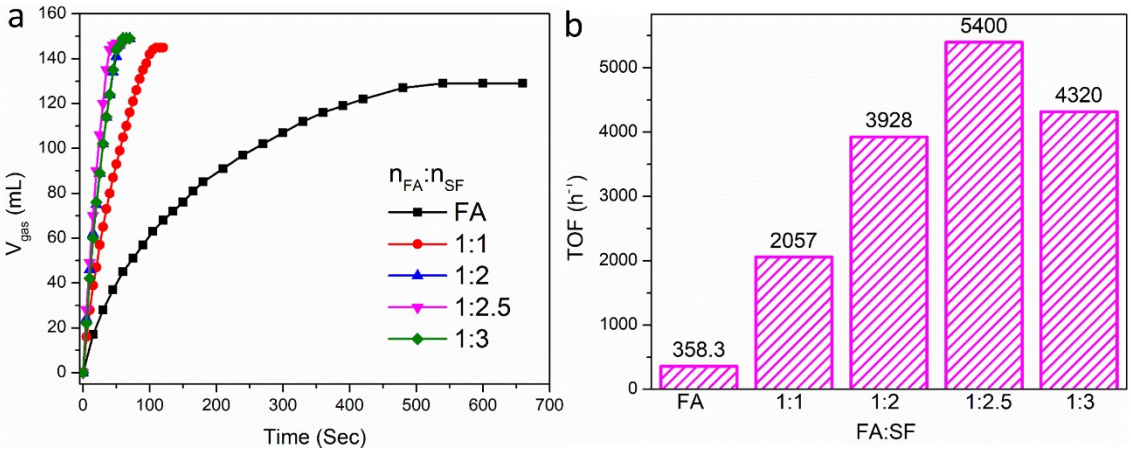

Figure 3.14. (a) Volume of the generated gas (CO_2 + H_2) *versus* time for FA dehydrogenation with different n_{FA}/n_{SF} molar ratios over Au_2Pd_3@(P)N-C and (b) the corresponding TOF values (n_{Au+Pd}/n_{FA} = 0.017, n_{FA} = 3 mmol, 30 °C).

SF is a well-known promoter for FA dehydrogenation and the optimal ratio of FA to SF for this work is determined to be 1/2.5 (30 °C, n_{Au+Pd}/n_{FA} = 0.017, n_{FA} = 3 mmol; Figure 3.14). It is worth noting that even without the addition of SF, Au_2Pd_3@(P)N-C displays an excellent catalytic activity with a TOF value of 358.3 h^{-1} at 30 °C (n_{FA} = 3 mmol).

Further to investigate the catalytic performance of Au_2Pd_3@(P)N-C, FA dehydrogenations were carried out at different reaction temperatures of 10–50 °C (n_{Au+Pd}/n_{FA} = 0.017, n_{FA}/n_{SF} = 1/2.5, n_{FA} = 3 mmol). The catalytic activity is enhanced with increasing the reaction temperature. Even at a temperature as low as 10 °C, the catalyst exhibits a TOF value as high as 1964 h^{-1}. The corresponding activation energy (E_a) was estimated to be 34.8 kJ mol^{-1} based on the Arrhenius plot, which is in accordance with its high catalytic activity at the low temperatures (Figure 3.15). The released gas mixture was measured by gas chromatography (GC), and only CO_2 and H_2 were detected. CO was not detected at the level of detection limit of 10 ppm (Figure 3.16).

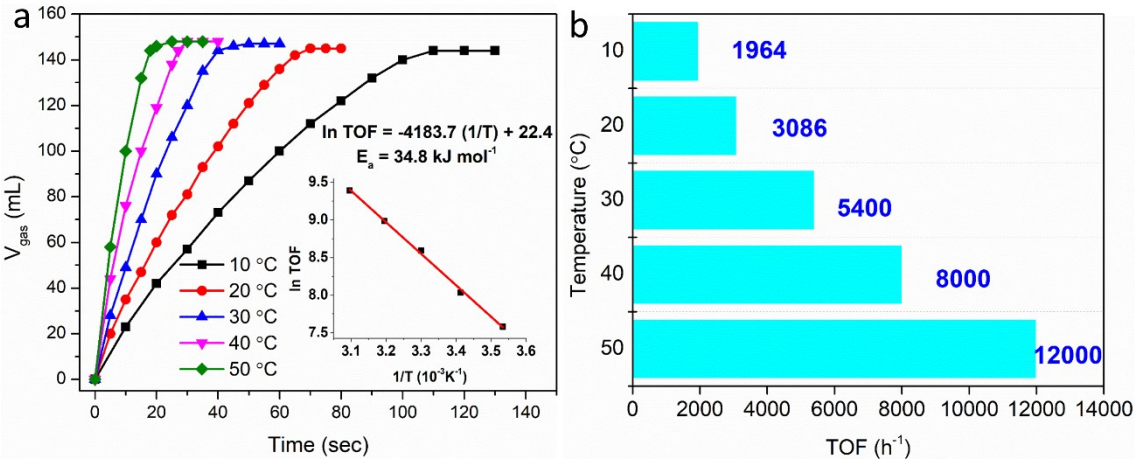

Figure 3.15. (a) Temperature dependence of gas evolution from FA over Au_2Pd_3@(P)N-C, and (b) the corresponding TOF values (Inset in (a) is Arrhenius plot (lnTOF) *vs.* 1/T)) (n_{Au+Pd}/n_{FA} = 0.017, n_{FA}/n_{SF} = 1/2.5, n_{FA} = 3 mmol).

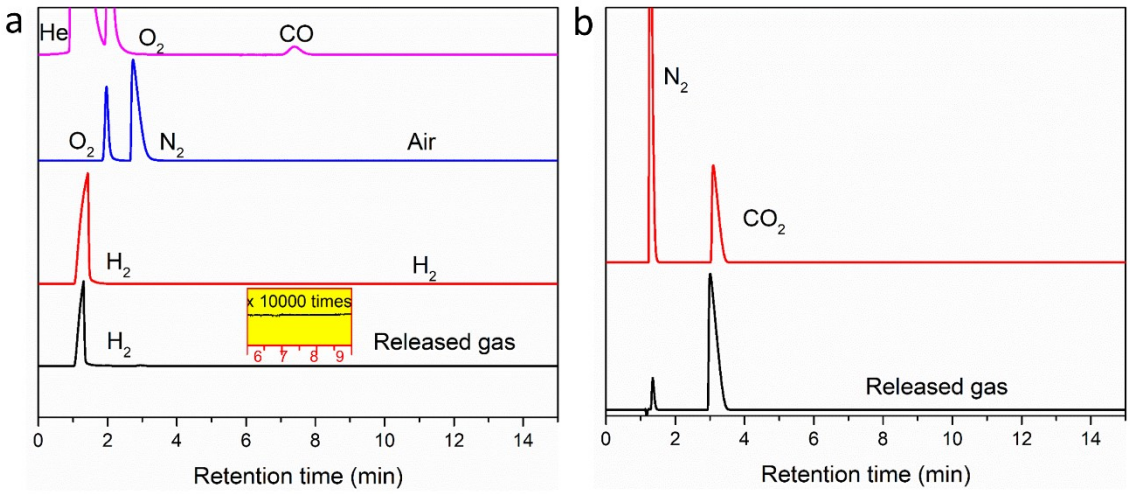

Figure 3.16. Gas chromatograms of the released gas from the decomposition of FA/SF in the presence of Au_2Pd_3@(P)N-C with (a) CO, air and H_2 and (b) CO_2 as reference gases (n_{Au+Pd}/n_{FA} = 0.017, n_{FA}/n_{SF} = 1/2.5, n_{FA} = 3 mmol, 30 °C), showing the presence of H_2 and CO_2, and the absence of CO at the detection limit of 10 ppm in the released gas.

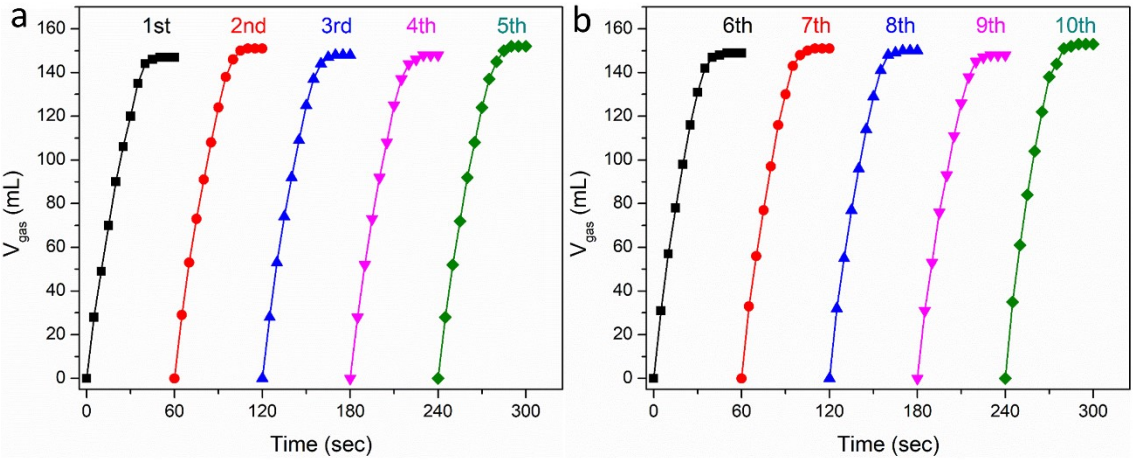

Figure 3.17. Durability test (10 cycles) for the dehydrogenation of FA/SF solutiom over Au_2Pd_3@(P)N-C (n_{Au+Pd}/n_{FA} = 0.017, n_{FA}/n_{SF} = 1/2.5, n_{FA} = 3 mmol, 30 °C)

The durability of the catalyst is vital in practical usage of fuel cells. Au_2Pd_3@(P)N-C was employed for FA dehydrogenation for 10 cycles and no activity loss was observed (Figure 3.17). Additionally, the particles sizes and morphology of AuPd NPs after 10

cycles are retained when examined by TEM and XRD analyses (Figure 3.18), suggesting that the Au_2Pd_3@(P)N-C catalyst possesses an excellent stability for FA dehydrogenation at current conditions.

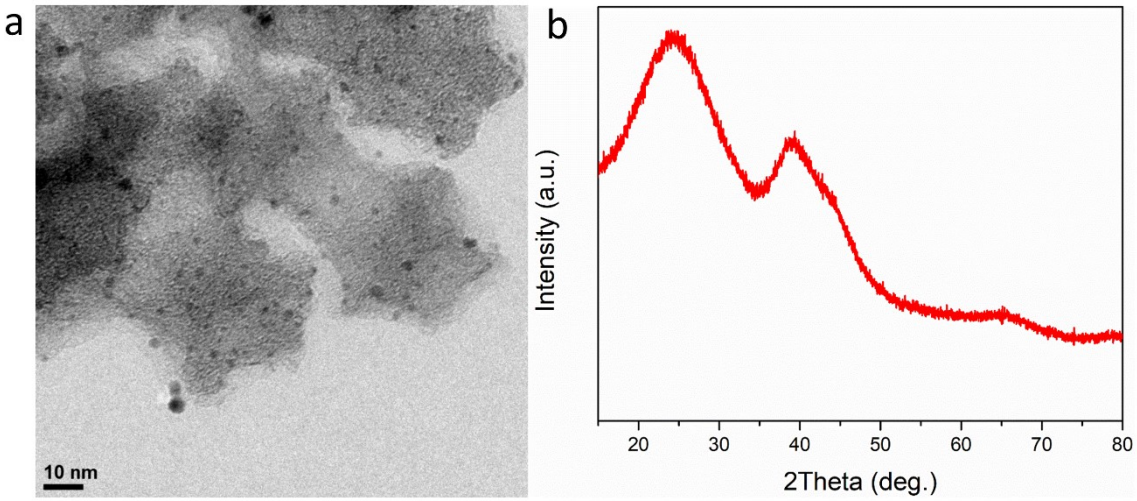

Figure 3.18. (a) TEM image and (b) XRD pattern of Au_2Pd_3@(P)N-C after 10 cycles of FA dehydrogenation at 30 °C (n_{Au+Pd}/n_{FA} = 0.017, n_{FA}/n_{SF} = 1/2.5, n_{FA} = 3 mmol).

On one hand, the excellent catalytic activity and stability of the catalyst are attributed to the uniform distribution of ultrafine AuPd NPs introduced by the phosphate-mediation approach as Au_2Pd_3@N-C shows a much lower catalytic activity with a TOF value of 1350 h^{-1} at 30 °C (n_{Au+Pd}/n_{FA} = 0.017, n_{FA}/n_{SF} = 1/2.5, n_{FA} = 3 mmol; Figure 3.18). To further evidence the influence of the phosphate-mediation approach, different P sources such as ammonium phosphate monobasic ($NH_4H_2PO_4$) (designated as PN-C1) and ammonium phosphate dibasic ($(NH_4)_2HPO_4$) (designated as PN-C2) were also employed instead of H_3PO_4. Both of PN-C1 and PN-C2 were successfully anchored by phosphate with P contents of 1.1 wt% and 0.52 wt%, repectively (Table 3.2). Unsurprisingly, the as-syntheized catalysts show enhanced catalytic activities than Au_2Pd_3@N-C, which is in accordance with the P contents on their supports (Figure 3.19) and their particle sizes of AuPd NPs are also smaller than Au_2Pd_3@N-C (Figure 3.20). By the way, phosphate were

removed successfully in the alkaline solution during the reduction of metal ions in both samples (Figure 3.21).

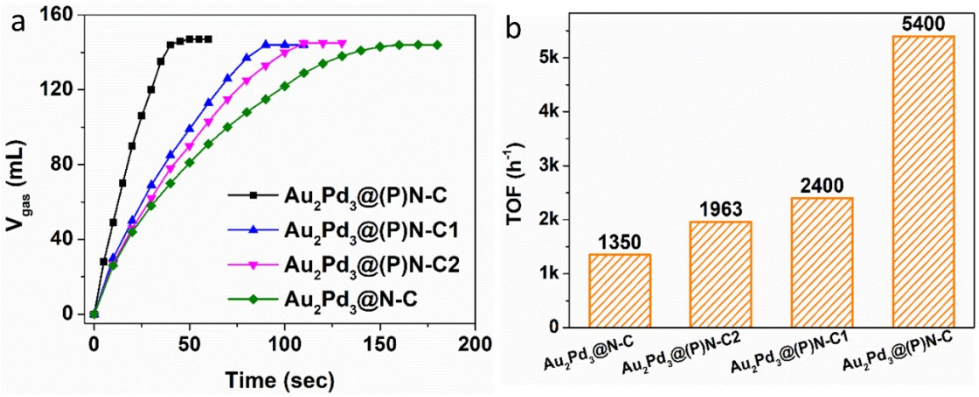

Figure 3.19. (a) Gas evolution from FA over AuPd NPs on N-C and its counterparts treated with different P sources, and (b) the corresponding TOF values (30 °C , n_{Au+Pd}/n_{FA} = 0.017, n_{FA}/n_{SF} = 1/2.5, n_{FA} = 3 mmol).

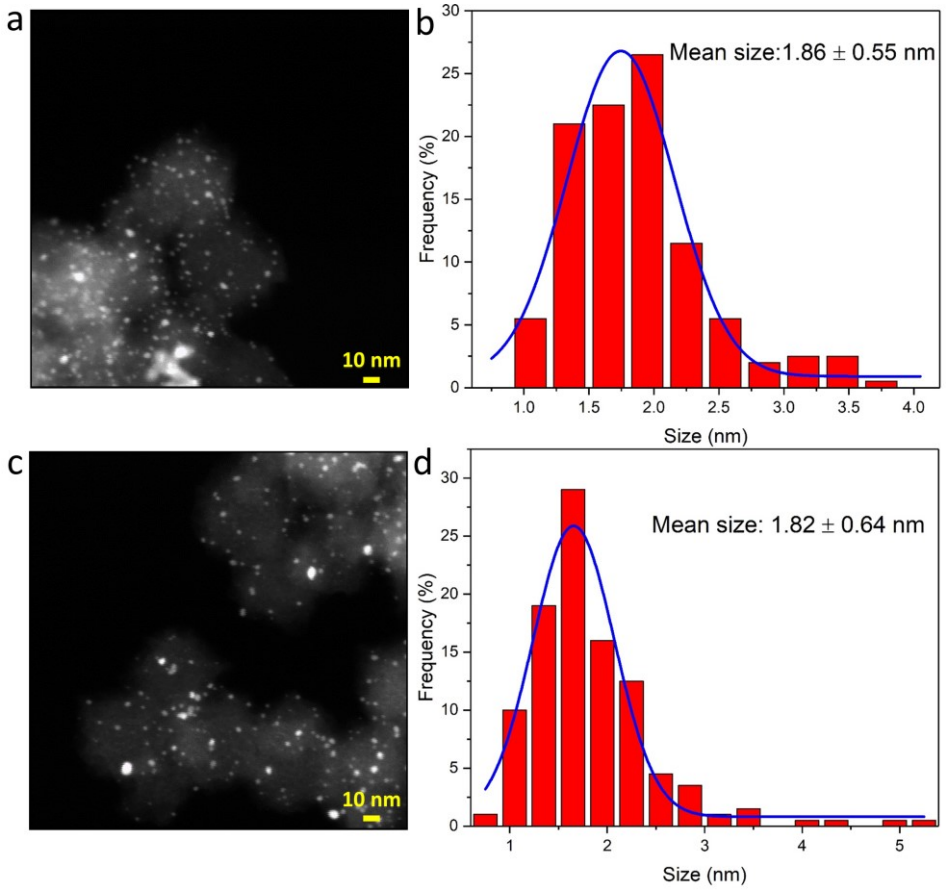

Figure 3.20. HAADF-STEM images and the corresponding particle size distributions of (a-b) Au_2Pd_3@(P)N-C1 and (c-d) Au_2Pd_3@(P)N-C2.

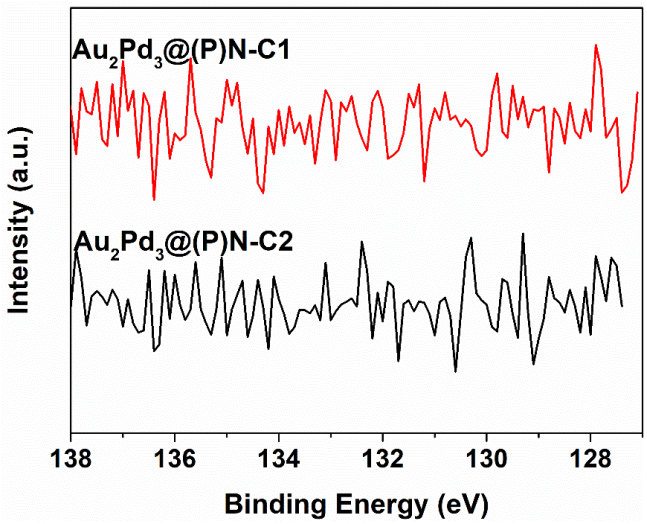

Figure 3.21. P 2p XPS spectra of Au_2Pd_3@(P)N-C1 and Au_2Pd_3@(P)N-C2.

On the other hand, it is considerded that the N doping also plays an important role in the activity enhancement due to the synergetic effect between N atoms and metal NPs.[12] Therefore, the commercial carbon MSP-20X without N (desingated as MSP) was used in place of N-C to prepare different supports for AuPd nanocatalysts. MSP and its N-, P- and P, N-functionalized counterparts were used as supports for AuPd nanocatalyst preparations, and the catalytic performances shown in Figure 3.22 demonstrate that single N doping or phosphate-mediation approach can double the catalytic activity while the combination of both can futher improve the catalytic performance. Obviously, N doping, especially combinied with the phosphate-mediation approach, can enhance the catalytic activity of AuPd nanocatalyst at low temperatures. Like Au_2Pd_3@(P)N-C, the P groups were successfully removed in the alkaline solution during the reduction of metal ions in Au_2Pd_3@(P)-MSP and Au_2Pd_3@(P)N-MSP (Figure 3.23).

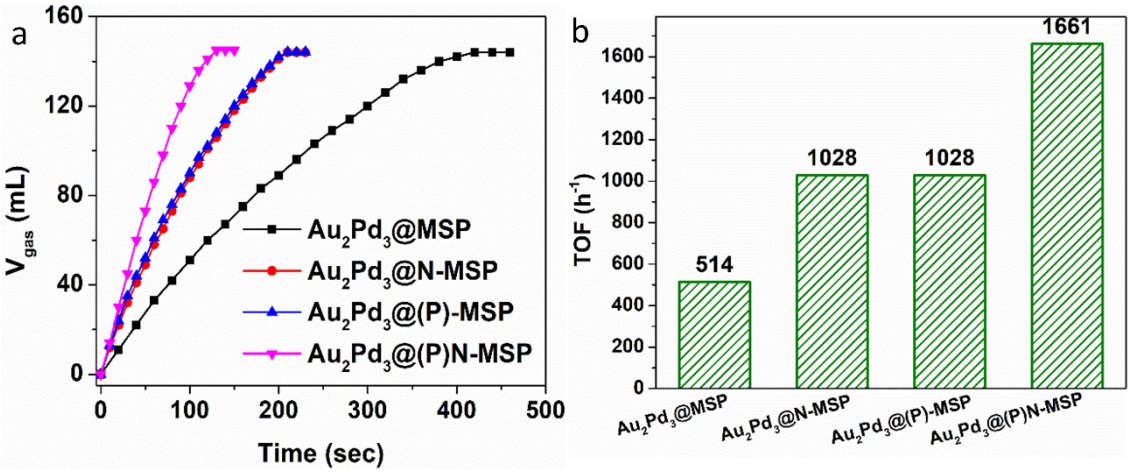

Figure 3.22. gas evolution from FA over AuPd NPs on MSP and its N-, P- and P, N-functionalized counterparts, the corresponding (h) TOF values (30 °C, n_{Au+Pd}/n_{FA} = 0.017, n_{FA}/n_{SF} = 1/2.5, n_{FA} = 3 mmol)

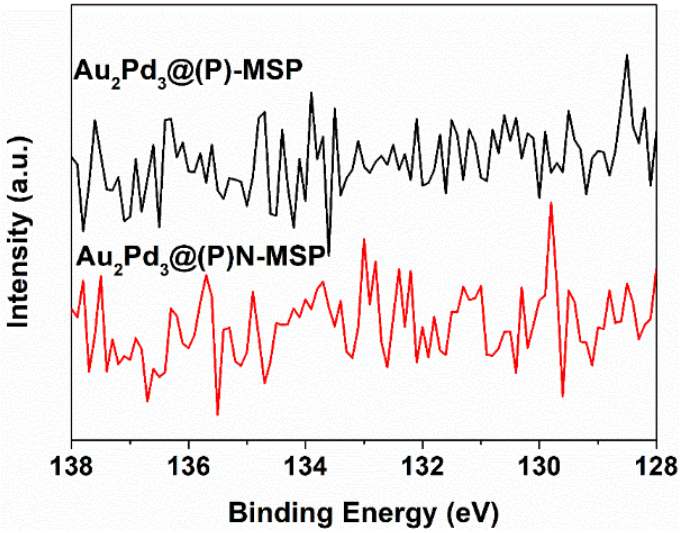

Figure 3.23. P 2p XPS spectra of Au_2Pd_3@(P)-MSP and Au_2Pd_3@(P)N-MSP.

The HAADF-STEM images (Figure 3.24) show that N doping or phosphate-mediation can downsize AuPd NPs and the combination of both gives the smallest AuPd NPs with the best catalytic performance.

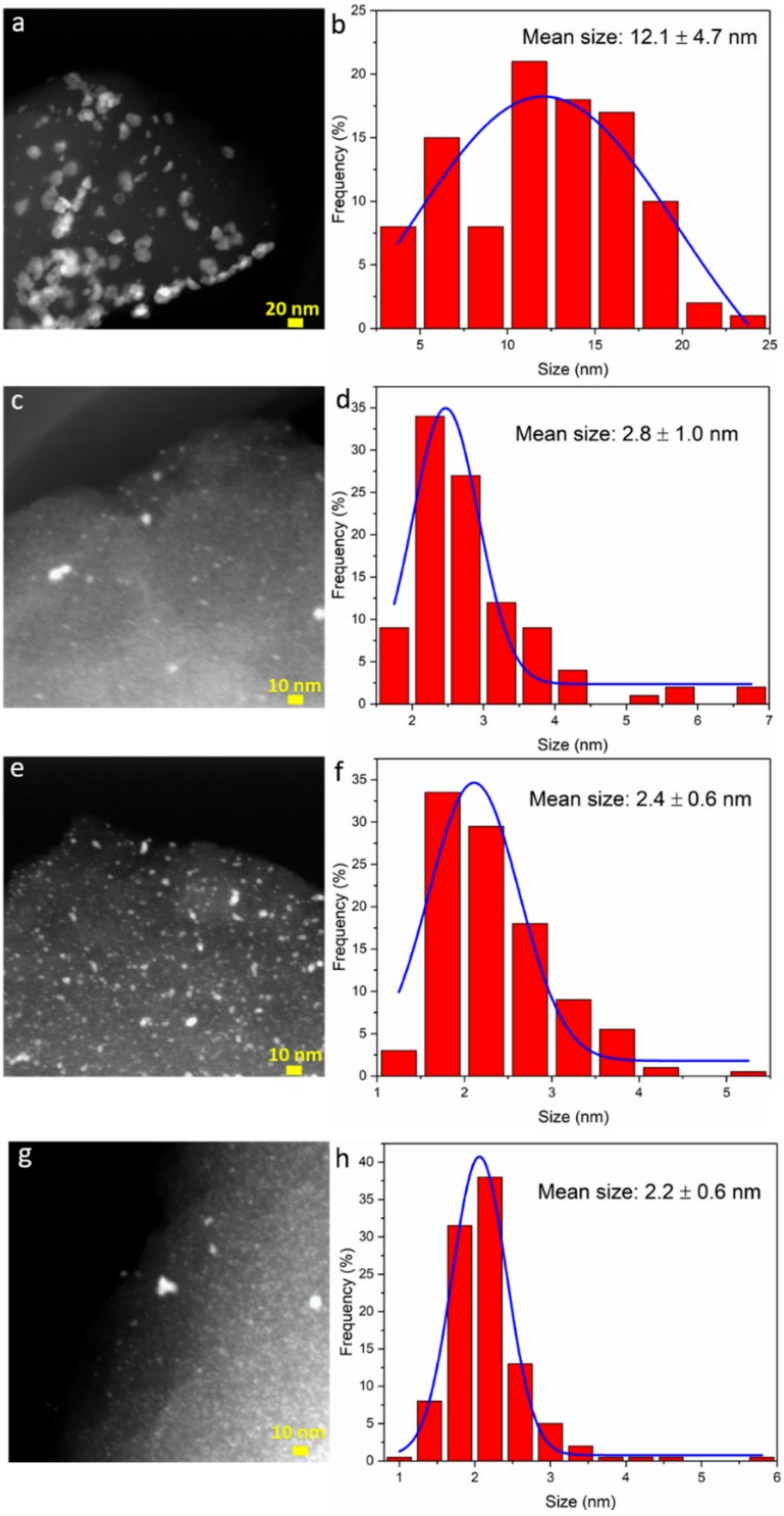

Figure 3.24. HAADF-STEM images and the corresponding particle size distributions of AuPd NPs of (a, b) Au_2Pd_3@MSP, (c, d) Au_2Pd_3@N-MSP, (e, f) Au_2Pd_3@(P)-MSP and (g, h) Au_2Pd_3@(P)N-MSP.

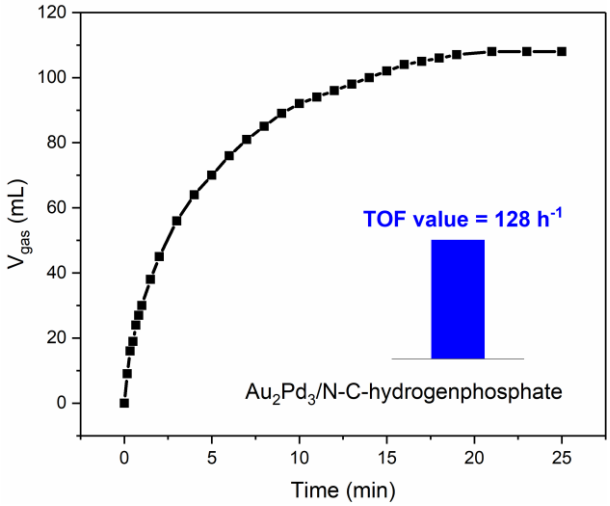

Figure 3.25. Volume of the generated gas (CO_2 + H_2) *versus* time for FA dehydrogenation over Au_2Pd_3/N-C-hydrogenphosphate (n_{Au+Pd}/n_{FA} = 0.017, n_{FA}/n_{SF} = 1/2.5, n_{FA} = 3 mmol, 30 °C).

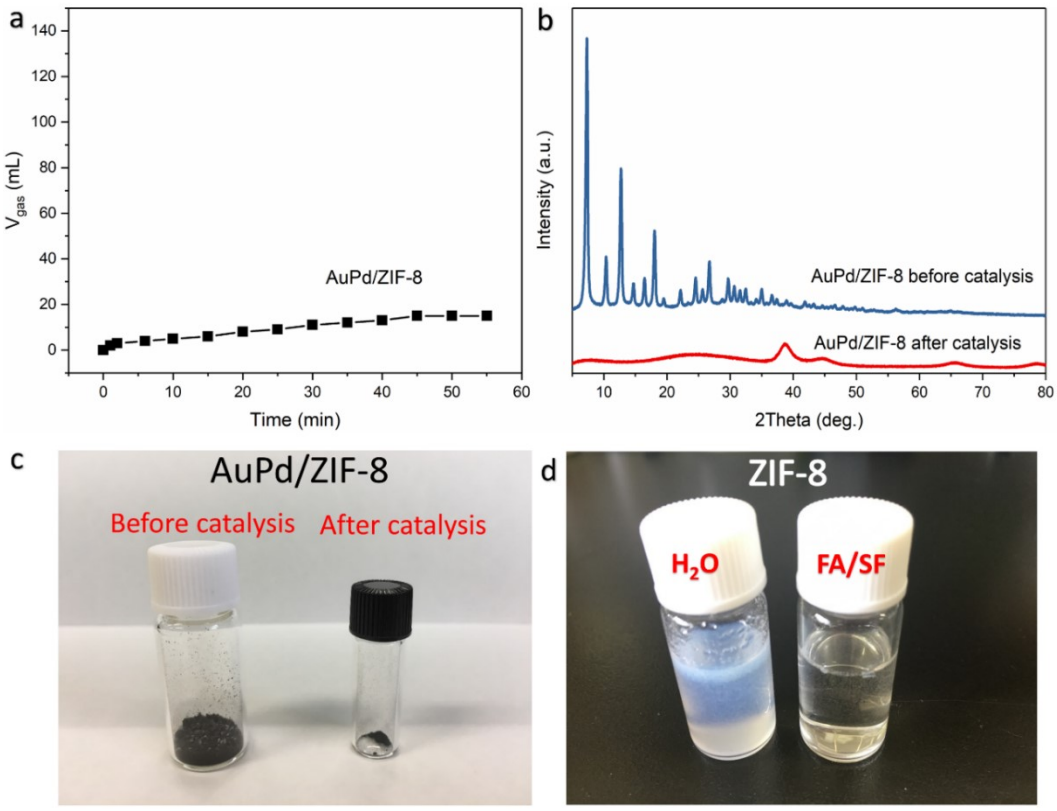

Figure 3.26. (a) Gas evolution from FA/SF solution over AuPd/ZIF-8 (30 °C, n_{Au+Pd}/n_{FA} = 0.017, n_{FA}/n_{SF} = 1/2.5, n_{FA} = 3 mmol), (b) XRD patterns and (c) photograph of AuPd/ZIF-8 before and after catalysis, and (d) photograph of ZIF-8 (100 mg) samples in 3 mL H_2O and 3 mL FA/SF solution (n_{FA}/n_{SF} = 1/2.5, n_{FA} = 3 mmol).

It has been reported that hydrogenphosphate ions act as a good stabilizing agent for the synthesis of colloidally stable metal NPs.[16] For comparison, we prepared the Au_2Pd_3/N-C-hydrogenphosphate, which showed only a TOF value of 128 h^{-1} for FA dehydrogenation (n_{Au+Pd}/n_{FA} = 0.017, n_{FA}/n_{SF} = 1/2.5, n_{FA} = 3 mmol, 30 °C) (Figure 3.25). The phosphate-mediation approach shows a better stabilizing effect for metal ions caused by the uniform phosphate anchoring on the carbon surface, which is more efficient than post-synthesis immobilization of colloidally stable metal NPs onto the carbon support. Besides, carbonization of ZIF-8 is essential for use to FA dehydrogenation since ZIF-8 is not stable in the acidic condition (pH < 6).[17] AuPd/ZIF-8 shows almost no activity for FA dehydrogenation since the ZIF-8 is totally decomposed in our FA/SF system (pH = 5), leaving unsupported AuPd particles in the catalysis system (Figure 3.26).

3.4 Conclusion

In summary, for the first time, a high-performance AuPd nanocatalyst has been synthesized via a phosphate-mediation approach which provides strong interactions with metal ions and results in the formation of well-dispersed ultrafine AuPd NPs. The as-synthesized Au_2Pd_3@(P)N-C exhibits an extremely high catalytic activity for FA dehydrogenation at low temperatures, showing a TOF value as high as 5400 h^{-1} at 30 °C and 1964 h^{-1} at 10 °C. The phosphate-mediation approach, especially combined with simultaneous N doping in carbons, is an effective methodology for preparation of highly active AuPd NPs. This work opens a new avenue to synthesize highly efficient metal nanocatalysts for applications in various catalytic fields.

References

[1] a) S. Enthaler, J. von Langermann, T. Schmidt, *Energy Environ. Sci.* **2010**, *3*, 1207; b) A. Boddien, F. Gärtner, C. Federsel, P. Sponholz, D. Mellmann, R. Jackstell, H. Junge, M. Beller, *Angew. Chem. Int. Ed.* **2011**, *50*, 6411; c) M. Grasemann, G. Laurenczy, *Energy Environ. Sci.* **2012**, *5*, 8171; d) M. Yadav, Q. Xu, *Energy Environ. Sci.* **2012**, *5*, 9698; e) Q.-L. Zhu, Q. Xu, *Energy Environ. Sci.* **2015**, *8*, 478; f) J. r. Eppinger, K.-W. Huang, *ACS Energy Lett.* **2016**, *2*, 188.

[2] a) B. Loges, A. Boddien, F. Gärtner, H. Junge, M. Beller, *Top. Catal.* **2010**, *53*, 902; b) Q.-L. Zhu, N. Tsumori, Q. Xu, *Chem. Sci.* **2014**, *5*, 195; c) Y. Chen, Q.-L. Zhu, N. Tsumori, Q. Xu, *J. Am. Chem. Soc.* **2015**, *137*, 106; d) C. Tang, A. E. Surkus, F. Chen, M. M. Pohl, G. Agostini, M. Schneider, H. Junge, M. Beller, *Angew. Chem.* **2017**, *129*, 16843.

[3] a) T. C. Johnson, D. J. Morris, M. Wills, *Chem. Soc. Rev.* **2010**, *39*, 81; b) A. Boddien, D. Mellmann, F. Gärtner, R. Jackstell, H. Junge, P. J. Dyson, G. Laurenczy, R. Ludwig, M. Beller, *Science* **2011**, *333*, 1733; c) J. F. Hull, Y. Himeda, W.-H. Wang, B. Hashiguchi, R. Periana, D. J. Szalda, J. T. Muckerman, E. Fujita, *Nat. Chem.* **2012**, *4*, 383; d) D. Mellmann, P. Sponholz, H. Junge, M. Beller, *Chem. Soc. Rev.* **2016**, *45*, 3954; e) K. Sordakis, C. Tang, L. K. Vogt, H. Junge, P. J. Dyson, M. Beller, G. Laurenczy, *Chem. Rev.* **2017**, *118*, 372; f) N. Onishi, G. Laurenczy, M. Beller, Y. Himeda, *Coord. Chem. Rev.* **2018**, *373*, 317.

[4] a) M. Zahmakıran, S. Özkar, *Nanoscale* **2011**, *3*, 3462; b) A. Dhakshinamoorthy, H. Garcia, *Chem. Soc. Rev.* **2012**, *41*, 5262; c) C. T. Campbell, *Acc. Chem. Res.* **2013**, *46*, 1712; d) H. R. Moon, D.-W. Lim, M. P. Suh, *Chem. Soc. Rev.* **2013**, *42*, 1807; e) Q.-L. Zhu, Q. Xu, *Chem* **2016**, *1*, 220; f) Z. Li, Q. Xu, *Acc. Chem. Res.* **2017**, *50*,

1449.

[5] a) K. Mori, M. Dojo, H. Yamashita, *ACS Catal.* **2013**, *3*, 1114; b) N. Wang, Q. Sun, R. Bai, X. Li, G. Guo, J. Yu, *J. Am. Chem. Soc.* **2016**, *138*, 7484; c) Q. Wang, N. Tsumori, M. Kitta, Q. Xu, *ACS Catal.* **2018**, *8*, 12041; d) Q.-L. Zhu, F.-Z. Song, Q.-J. Wang, N. Tsumori, Y. Himeda, T. Autrey, Q. Xu, *J. Mater. Chem. A* **2018**, *6*, 5544.

[6] a) M. Ojeda, E. Iglesia, *Angew. Chem.* **2009**, *121*, 4894; b) Q.-Y. Bi, X.-L. Du, Y.-M. Liu, Y. Cao, H.-Y. He, K.-N. Fan, *J. Am. Chem. Soc.* **2012**, *134*, 8926; c) Q. Liu, X. Yang, Y. Huang, S. Xu, X. Su, X. Pan, J. Xu, A. Wang, C. Liang, X. Wang, *Energy Environ. Sci.* **2015**, *8*, 3204.

[7] a) X. Gu, Z.-H. Lu, H.-L. Jiang, T. Akita, Q. Xu, *J. Am. Chem. Soc.* **2011**, *133*, 11822; b) Ö. Metin, X. Sun, S. Sun, *Nanoscale* **2013**, *5*, 910; c) J. M. Yan, Z. L. Wang, L. Gu, S. J. Li, H. L. Wang, W. T. Zheng, Q. Jiang, *Adv. Energy. Mater.* **2015**, *5*, 1500107; d) Z. Zheng, T. Tachikawa, T. Majima, *J. Am. Chem. Soc.* **2015**, *137*, 948; e) Y. Karatas, A. Bulut, M. Yurderi, I. E. Ertas, O. Alal, M. Gulcan, M. Celebi, H. Kivrak, M. Kaya, M. Zahmakirana, *Appl. Catal., B*. **2016**, *180,* 586.

[8] a) M. Yadav, T. Akita, N. Tsumori, Q. Xu, *J. Mater. Chem.* **2012**, *22*, 12582; b) Y. Y. Cai, X. H. Li, Y. N. Zhang, X. Wei, K. X. Wang, J. S. Chen, *Angew. Chem. Int. Ed.* **2013**, *52*, 11822; c) M. Yurderi, A. Bulut, M. Zahmakiran, M. Kaya, *Appl. Catal., B* **2014**, *160*, 514; d) L. Yang, W. Luo, G. Cheng, *Int. J. Hydrogen Energy* **2016**, *41*, 439; e) F. Z. Song, Q. L. Zhu, X. Yang, W. W. Zhan, P. Pachfule, N. Tsumori, Q. Xu, *Adv. Energy. Mater.* **2018**, *8*, 1701416.

[9] a) B. Liu, H. Shioyama, T. Akita, Q. Xu, *J. Am. Chem. Soc.* **2008**, *130*, 5390; b) W. Chaikittisilp, K. Ariga, Y. Yamauchi, *J. Mater. Chem. A* **2013**, *1*, 14; c) K. Shen, X. Chen, J. Chen, Y. Li, *ACS Catal.* **2016**, *6*, 5887; d) J. Tang, Y. Yamauchi, *Nat. Chem.*

2016, *8*, 638; e) S. Dang, Q.-L. Zhu, Q. Xu, *Nat. Rev. Mater.* **2018**, *3*, 17075; f) C. C. Hou, Q. Xu, *Adv. Energy. Mater.* **2018**, 1801307.

[10] a) K. Jiang, K. Xu, S. Zou, W.-B. Cai, *J. Am. Chem. Soc.* **2014**, *136*, 4861; b) Z. Li, X. Yang, N. Tsumori, Z. Liu, Y. Himeda, T. Autrey, Q. Xu, *ACS Catal.* **2017**, *7*, 2720; c) X. Ji, B. Liu, X. Ren, X. Shi, A. M. Asiri, X. Sun, *ACS Sustainable Chem. Eng.* **2018**, *6*, 4499.

[11] a) K. Jiang, A. Eitan, L. S. Schadler, P. M. Ajayan, R. W. Siegel, *Nano Lett.* **2003**, *3*, 275; b) D. H. Lee, J. A. Lee, W. J. Lee, D. S. Choi, W. J. Lee, S. O. Kim, *J. Phys. Chem. C* **2010,** *114,* 21184.

[12] a) R. Arrigo, M. E. Schuster, Z. Xie, Y. Yi, G. Wowsnick, L. L. Sun, K. E. Hermann, M. Friedrich, P. Kast, M. Hävecker, *ACS Catal.* **2015**, *5*, 2740; b) F.-Z. Song, Q.-L. Zhu, N. Tsumori, Q. Xu, *ACS Catal.* **2015**, *5*, 5141; c) Q. Y. Bi, J. D. Lin, Y. M. Liu, H. Y. He, F. Q. Huang, Y. Cao, *Angew. Chem. Int. Ed.* **2016**, *55*, 11849; d) L. He, F. Weniger, H. Neumann, M. Beller, *Angew. Chem. Int. Ed.* **2016**, *55*, 12582; e) J. M. Yan, S. J. Li, S. S. Yi, B. R. Wulan, W. T. Zheng, Q. Jiang, *Adv. Mater.* **2018**, *30*, 1703038.

[13] a) X. C. Huang, Y. Y. Lin, J. P. Zhang, X. M. Chen, *Angew. Chem. Int. Ed.* **2006**, *45*, 1557; b) K. S. Park, Z. Ni, A. P. Côté, J. Y. Choi, R. Huang, F. J. Uribe-Romo, H. K. Chae, M. O'Keeffe, O. M. Yaghi, *Proc. Natl. Acad. Sci. U.S.A.* **2006**, *103*, 10186.

[14] F. Suárez-García, A. Martínez-Alonso, J. M.D. Tascón, *Carbon* **2004**, *42*, 1419.

[15] a) H. Teng, T. S. Yeh, L. Y. Hsu, *Carbon* **1998**, *36*, 1387; b) A. Castro-Muñiz, F. Suárez-García, A. Martínez-Alonso, J. M.D. Tascón, *J Colloid Interf. Sci.* **2011**, *361*, 307; c) M. Q. Guo, J. Q. Huang, X. Y. Kong, H. J. Peng, H. Shui, F. Y. Qian, L. Zhu, W. C. Zhu, Q. Zhang, *New Carbon Mater.* **2016**, *31*, 352.

[16] S. Caliskan, M. Zahmakiran, F. Durap, S. Özkar, *Dalton Trans.* **2012**, *41*, 4976.

[17] M. Jiana, B. Liua, G. Zhang, R. Liu, X. Zhang, *Colloids and Surfaces A: Physicochem. Eng. Aspects* **2015**, *465*, 67.

Chapter 4

Copper Decorated Cobalt Oxide Nanoparticles from Bimetallic MOF-74 for Dehydrogenation of Ammonia Borane

In this work, copper decorated cobalt oxide nanoparticles were successfully prepared from a Cu-Co-MOF-74 by in-situ reduction during hydrogen evolution from aqueous ammonia borane. This Cu-Co-MOF-74 displays a much better catalytic activity than their monometallic MOF counterparts and even than the Cu@Co-MOF-74 prepared by a typical double solvents method. The in-situ reduction of bimetallic MOF strategy takes advantage of uniform metal component distributions in the MOF and meantime avoids the aggregation during traditional thermolysis syntheses of MOF-derived metal/metal oxides. The Cu-Co-MOF-74 shows a TOF value of 18.5 min^{-1} and a good durability for 5 cycles for hydrogen evolution from ammonia borane at 25 °C. Considering the diversification of MOFs, this strategy gives a possibility of tailoring MOFs for specific functional metal/metal oxides in area of energy storage and conversion.

4.1 Introduction

Facing the ever-increasing energy demand for on-board application, hydrogen became a rising star as an efficient energy carrier.[1] Safe storage and distribution are the key issues needed to be solved for practical utilization. Liquid-phase chemical hydrogen storage materials which store hydrogen in form of chemical bond have attracted tremendous attention due to their convenience and safe handling.[2] Ammonia borane (AB, NH_3BH_3), with a high hydrogen content of 19.6 wt%, has been widely studied. Aqueous AB is stable

under ambient conditions and can provide sustainable hydrogen stream for fuel cells at room temperature with assistant of proper catalysts.[3] Noble metal NPs are the most common heterogeneous catalysts for efficient AB dehydrogenation, such as Pt, Pd, Rh, and Ru NPs.[4] However, considering the cost, recent researches turned to focus on base metals, especially the first row transition metals, such as Fe, Ni, Co and Cu and their alloyed NPs which demonstrate impressive activities for AB dehydrogenation.[5]

Metal–organic frameworks (MOFs) are consisted of metal ions and organic ligands with tunable components and so far, about 2000 MOFs have been successfully synthesized. Due to their uniform distribution of metal and organic contents, MOFs are utilized as precursors for preparations of metal/metal oxides, porous carbons and their hybrids by heating treatment in specific atmospheres. As-prepared materials are extensively used in electrochemical catalysis, photo catalysis, sensing, hydrogen storage and related areas.[6] Usually, to achieve an active catalyst, additional noble metal precursors are introduced into MOF structure with precise control which is a key step for the whole synthesis process.[7] However, traditional thermolysis synthesis strategy usually leads to aggregation of metal/metal oxides and the component of metal or metal oxides cannot be controlled precisely.[8] Therefore, a simple but effective method without additional metal precursor is in urgent need.

Herein, for the first time, we report copper decorated cobalt oxide NPs prepared by in-situ wet chemical reduction from a Co-Cu-MOF-74 for AB dehydrogenation (Figure 4.1). With very small amount addition of Cu in the preparation of Co-MOF-74, the catalytic activity was enhanced dramatically for AB decomposition, showing a TOF value of 18.5 min^{-1} at 25 °C based on the total weight of original MOF. The spatial limitation provided by the MOF structure during in-situ wet chemical reduction is critical for the formation

of active copper species, leading to the high performance for AB dehydrogenation.

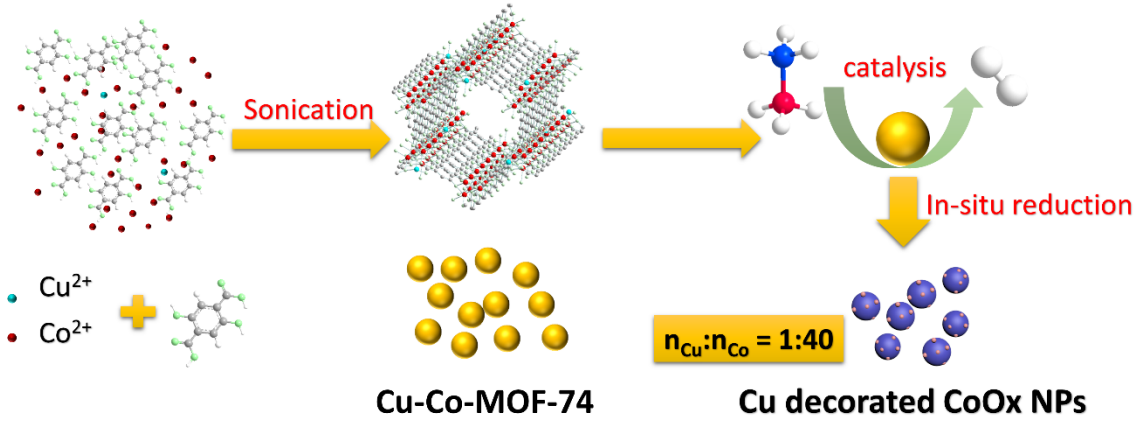

Figure 4.1. Schematic illustration of preparation of Cu-Co-MOF-74 nanocatalyst.

4.2 Experimental section

4.2.1 Materials

All chemicals were commercially available and used without further purification. 2,5-dihydroxyterephthalic acid (H_4DOBDC, Tokyo Chemical Industry Co., Ltd., ≥98.0%), cobalt (II) acetate 4-hydrate ($Co(CH_3COO)_2•4H_2O$, Kishida Chem. Co., 99%), copper(II) acetate 1-hydrate ($Cu(CH_3COO)_2•H_2O$, Kishida Chem. Co., 99%), methanol (Kishida Chem. Co., 99.8%), cobalt(II) nitrate hexahydrate ($Co(NO_3)_2•6H_2O$, Sigma-Aldrich, ≥98%), copper(II) nitrate 3-hydrate ($Cu(NO_3)_2•3H_2O$, Kishida Chem. Co., 99.5%), N, N-dimethylformamide (DMF, Tokyo Chemical Industry Co., Ltd., 99%), ammonia borane (AB, NH_3BH_3, JSC Aviabor, >97%), ethanol (C_2H_5OH, Kishida Chem. Co., >99.8%), and n-hexane (Kishida Chem. Co., 96%) were used as received. De-ionized (DI) water with a specific resistance of 18.2 MΩ·cm was obtained by reverse osmosis followed by ion-exchange and filtration (RFD 250NB, Toyo Seisakusho Kaisha, Ltd., Japan).

4.2.2 Syntheses of MOFs

(1) Co-MOF-74

50 mL methanol solution of H_4DOBDC (1.5 mmol) was added into 100 mL methanol solution of $Co(CH_3COO)_2$•$4H_2O$ (4 mmol) dropwise with sonication and kept for 2 h. Then the mixture was centrifuged and washed with fresh methanol for 2 times, and then soaked into fresh methanol for solvent exchange for 3 days. For each day, fresh methanol was changed.

(2) Cu-MOF-74

50 mL methanol solution of H_4DOBDC (1.5 mmol) was added into 100 mL methanol solution of $Cu(CH_3COO)_2$•H_2O (2 mmol) dropwise with sonication and kept for 2 h. Then the mixture was centrifuged and washed with fresh methanol for 2 times, and then soaked into fresh methanol for solvent exchange for 3 days. For each day, fresh methanol was changed.

(3) Cu-Co-MOF-74

The procedure of Cu-Co-MOF-74 was almost the same as Co-MOF-74 except additional 0.08 mmol $Cu(CH_3COO)_2$•H_2O was added into the methanol solution of $Co(CH_3COO)_2$•$4H_2O$ (4 mmol) during the preparation.

(4) Cu-Co-MOF-74-MB

Micro-block Cu-Co-MOF-74 (designated as Cu-Co-MOF-74-MB) was prepared as the following procedure: 0.75 mmol H_4DOBDC, 2 mmol $Co(NO_3)_2$•$6H_2O$ and 0.04 mmol $Cu(NO_3)_2$•$3H_2O$ were dissolved into a 60 mL mixture of DMF, ethanol and H_2O with volume ratio of 1:1:1 and stirred for 0.5 h. Then the mixture was transferred into 100 mL autoclave and heated at 100 °C for 24 h in a programming oven. After that, the mixture was centrifuged and washed by fresh methanol for 2 times, and then soaked into fresh methanol for solvent exchange for 3 days. Fresh methanol was changed for every day.

4.2.3 Syntheses of catalysts

(1) Cu-Co-MOF-74-*T* series catalysts

Cu-Co-MOF-74 (50 mg) was transferred into a programming furnace and heat to a preset temperature under argon atmosphere (designated as Cu-Co-MOF-74-*T*, *T* stands for temperature (°C), including room temperature (RT), 200, 350 and 650 °C) with a heating rate of 5 °C/min and kept at that temperature for 1h. After cooling down to room temperature naturally, the sample was used as catalyst for AB dehydrogenation directly.

(2) Control samples

a. The as-prepared Co-MOF-74, Cu-MOF-74 and Cu-Co-MOF-74-MB (50 mg) were used as catalysts for AB dehydrogenation at 25 °C for comparison.

b. Cu@Co-MOF-74

Cu@Co-MOF-74 was prepared by a double solvents method (DSM).[7a] 100 mg Co-MOF-74 (pretreated at 80 °C overnight) was dispersed into 50 mL n-hexane and 60 μL aqueous solution of $Cu(CH_3COO)_2 \bullet H_2O$ (n_{Cu} = 0.005 mmol) was added in 30 min. After stirring for 6 h, the sediment was dried at 80 °C in the vacuum oven overnight. The as-prepared sample (50 mg) was used for AB decomposition directly.

4.2.4 Catalytic activity characterization

4.2.4.1 Procedure for AB dehydrogenation

Reaction apparatus for measuring the H_2 evolution from AB is as the same as previously reported.[9] In general, 2 mL aqueous dispersion of as-prepared catalyst (original weight of MOF = 50 mg) was placed in 30 mL two-necked round-bottom flask which was placed in a water bath at a preset temperature (25, 30, 40, and 50 °C). A gas burette filled with water was connected to the reaction flask to measure the volume of released gas (temperature kept constant at 298 K during measurement). The reaction started when 1.0

mL aqueous AB solution (1 mmol) was injected into the system using a syringe. The volume of the evolved gas was monitored by recording the displacement of water in the gas burette.

4.2.4.2 Durability testing of Cu-Co-MOF-74

The durability testing of Cu-Co-MOF-74 was performed at 25 °C. The procedure was the same as described in 4.2.4.1. For each cycle, 1.0 mL aqueous AB solution (1 mmol) was injected to the catalytic system. The experiment was repeated for 5 times.

4.2.5 Calculation methods

The turnover frequency (TOF) reported here is an apparent TOF value based on the weight of catalyst, which is calculated from the equation as follow:

$$TOF = P_0V/(RTnt)$$

Where P_0 is the atmospheric pressure (101325 Pa), V is the final generated volume of (H_2) gas, R is the universal gas constant (8.3145 m^3 Pa mol^{-1} K^{-1}), T is the room temperature (298 K), n is total mole number of Co and Cu and t is the completion time of the reaction subtracted with the in-situ reduction time of catalyst in minute.

4.3 Results and discussion

Scanning transmission electron microscopy (SEM) images (Figure 4.2) show that ultrasonication synthesis at room temperature achieved Cu-Co-MOF-74 with sphere morphology. There's no morphology difference between Cu-Co-MOF-74 and Co-MOF-74, which means the addition of Cu in a small amount did not change the morphology of Co-MOF-74. According to the inductively coupled plasma-optical emission spectroscopy (ICP-OES) results, Cu-Co-MOF-74 possesses a Co content of 24.1 wt% and a Cu content

of 0.68 wt% (n_{Co} = 0.204 mmol; n_{Co} : n_{Cu} = 40 : 1), while the Co-MOF-74 has a Co content of 25.2 wt% (n_{Co} = 0.213 mmol). Besides, Cu-MOF-74 show totally different morphology with a high crystallinity. Of course, Co-MOF-74 show a uniform dispersion of Co component (Figure 4.3). What' more, Cu-Co-MOF-74 show uniform dispersion of both Cu and Co components (Figure 4.4).

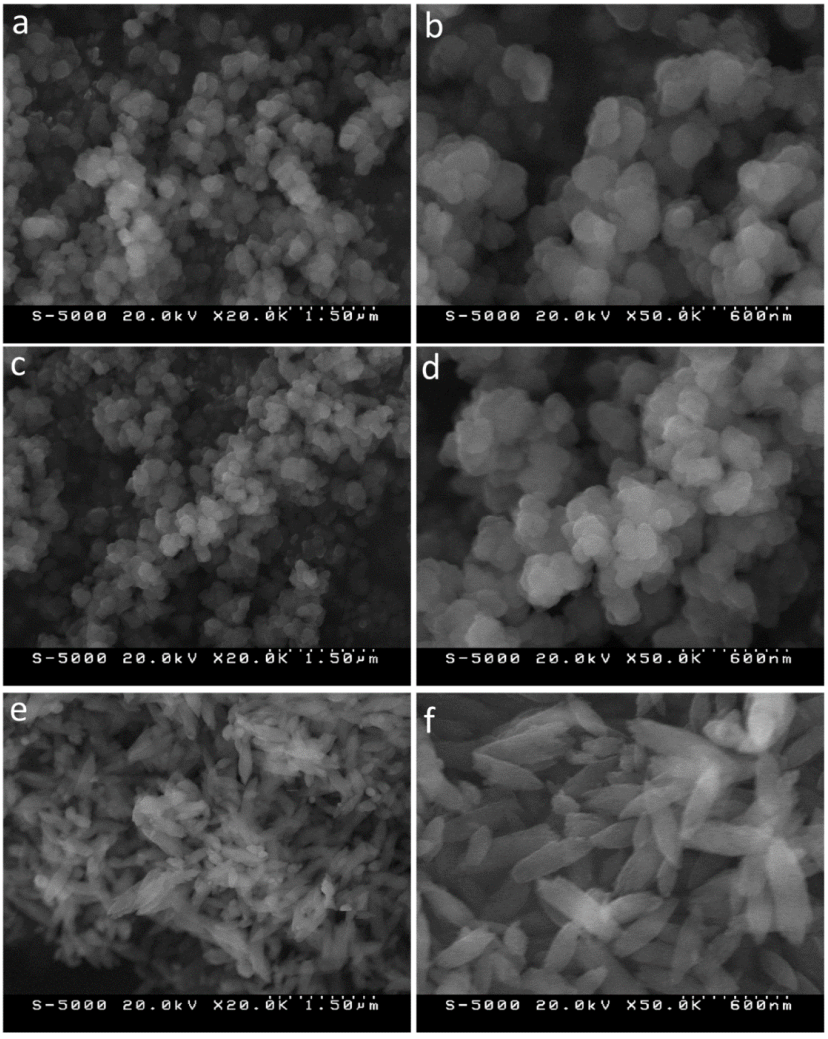

Figure 4.2. SEM images of (a, b) Cu-Co-MOF-74, (c, d) Co-MOF-74 and (e, f) Cu-MOF-74.

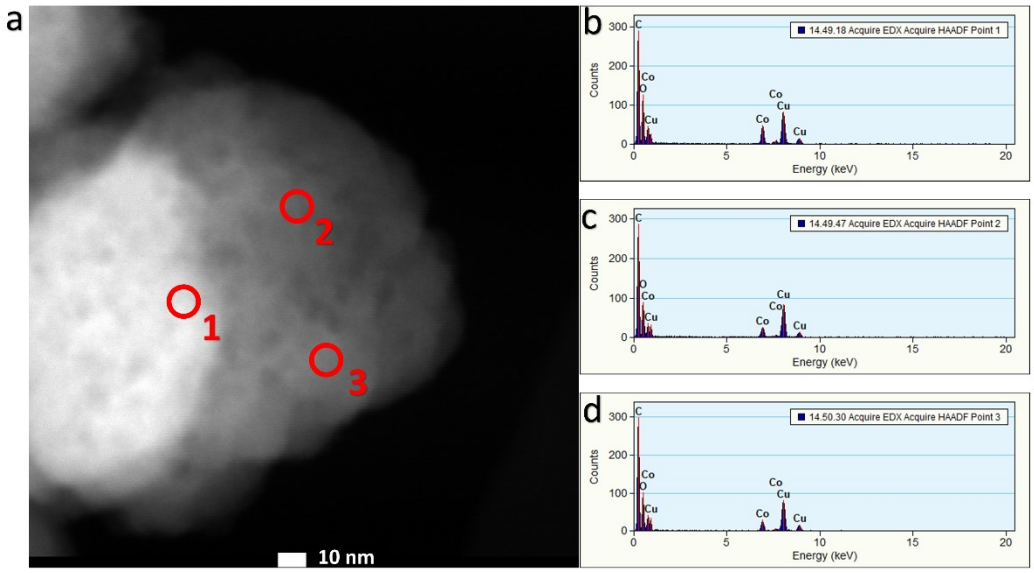

Figure 4.3 HAADF-STEM and corresponding EDS images of Co-MOF-74. (Cu TEM support grids used).

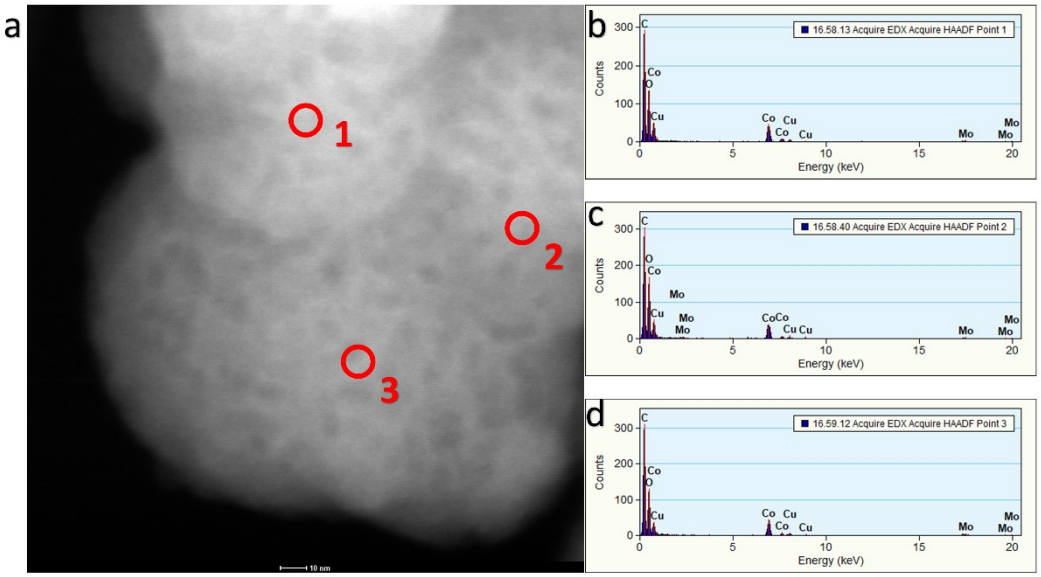

Figure 4.4 HAADF-STEM and corresponding EDS images of Cu-Co-MOF-74. (Mo TEM support grids used).

For comparison, the hydrothermal strategy produced Cu-Co-MOF-74 of micro-block morphology (designated as Cu-Co-MOF-74-MB, Figure 4.5a). Powder X-ray diffraction (PXRD) patterns (Figure 4.6) confirm the successful preparation of Cu-Co-MOF-74 since it shows similar XRD patterns with Cu-Co-MOF-74-MB.

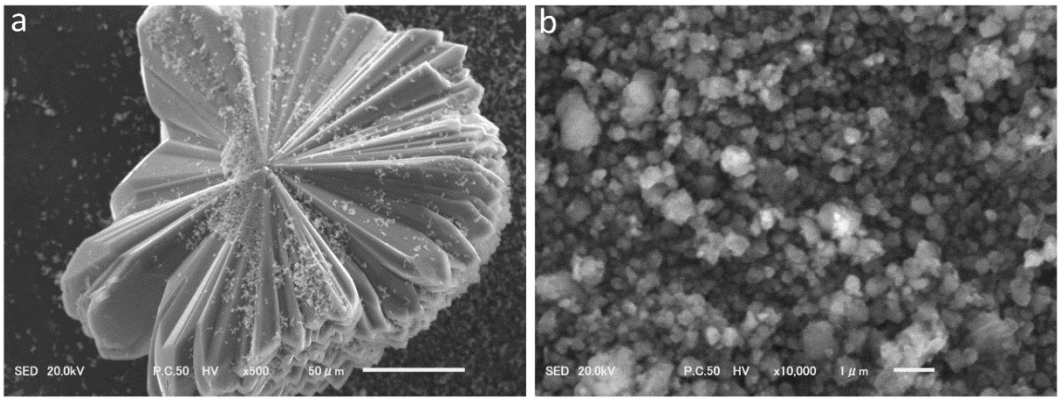

Figure 4.5. SEM images of (a) Cu-Co-MOF-74-MB and (b) Cu@Co-MOF-74.

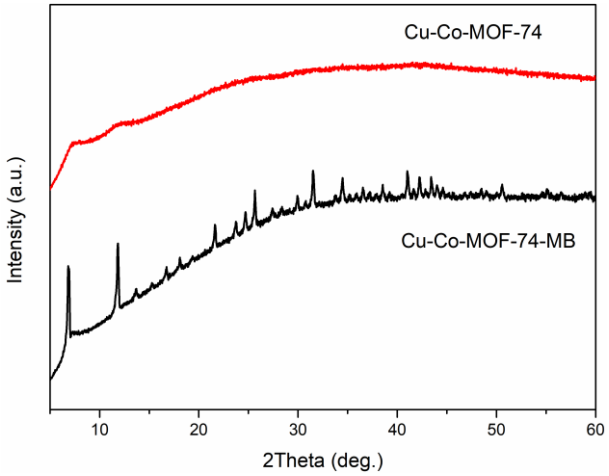

Figure 4.6. XRD patterns of Cu-Co-MOF-74-MB and Cu-Co-MOF-74.

The Cu-Co-MOF-74 was used as the catalyst for hydrogen evolution from AB directly (Figure 4.7). After addition of aqueous AB solution into the catalytic system, about 10 s, no gas was released but the color of the catalyst turned from brown to black. After 10 s, gas evolution begins and finally 62 mL H_2 was released in 40 s (25 °C, n_{Co} = 0.204 mmol, n_{Cu} = 0.005 mmol, n_{AB} = 1 mmol). It can be implied that, at the beginning of the catalytic process, with the addition of AB, Cu-Co-MOF-74 starts the in-situ reduction and as a result, metal NPs formed with consumption of parts of AB. From then on, the hydrogen evolution begins at the appearance of metal NPs and the remaining AB dehydrogenated. The durability test of Cu-Co-MOF-74 further confirm the hypothesis since from the

second cycle, the catalysts need no additional reduction time and the volume of H_2 raised to 72 mL. The Cu-Co-MOF-74 catalyst keep their activity for 5 cycles at current conditions.

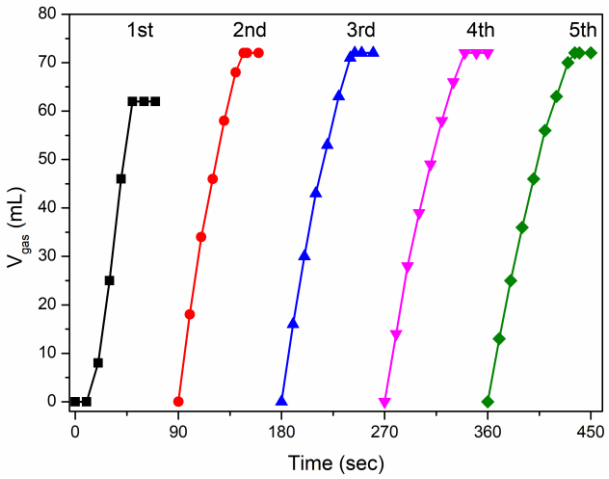

Figure 4.7. Durability of Cu-Co-MOF-74 for AB decomposition at 25 °C (n_{Co} = 0.204 mmol, n_{Cu} = 0.005 mmol, n_{AB} = 1 mmol)

Based on the results of X-ray photoelectron spectroscopy (XPS) analyses, after catalysis, the C1s peak at 288.5 eV decreased dramatically, suggesting the structure collapse of MOF-74 (Figure 4.8a). The XPS peaks of Co 2p become more intensive while the position has no obvious change, which means the Co formed CoOx and no Co^0 was reduced (Figure 4.8c). The position of Cu 2p peaks changed according to Figure 4.8d, implying the chemical state change of Cu^{2+} to Cu^0.

The HAADF-STEM and elemental and mapping images of Cu-Co-MOF-74 after AB dehydrogenation was shown in Figure 4.9. Obviously, after catalysis, the MOF structure was destroyed and Co was uniformly dispersed in the whole structure. Cu component was also uniformly dispersed except for some aggregations. The aggregation of Cu component meet with the chemical state of Cu^{2+} to Cu^0 from XPS measurement. The uniformly dispersion of Cu NPs is the key to the enhanced catalytic activity of Cu-Co-MOF-74.

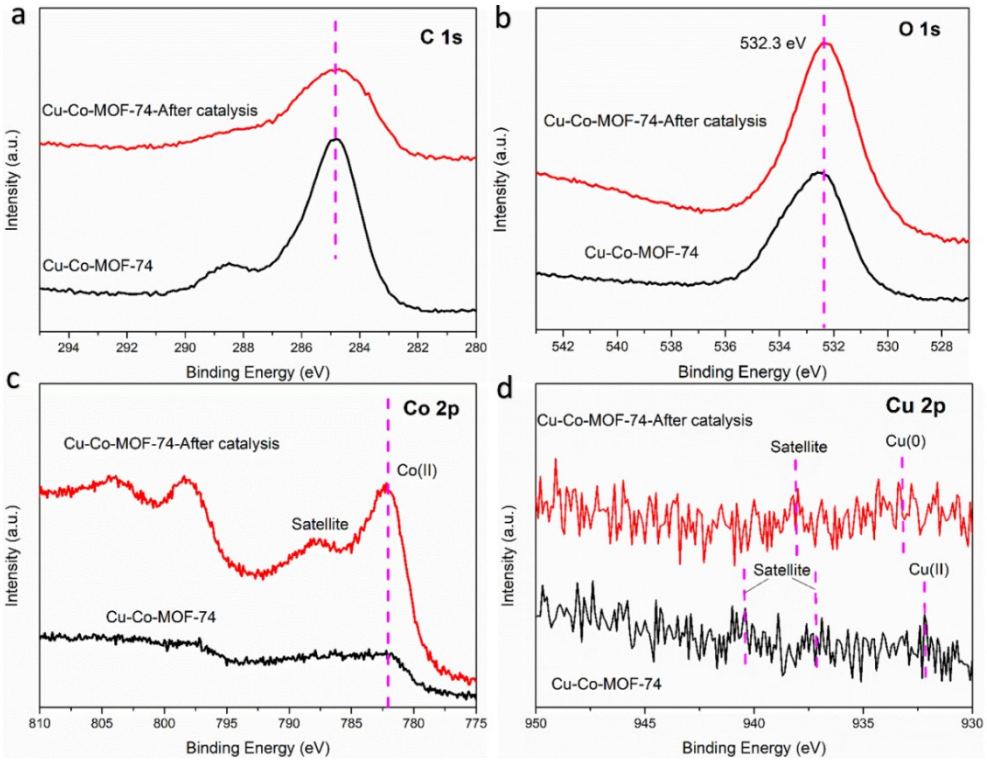

Figure 4.8 XPS spectra of (a) C 1s, (b) O 1s, (c) Co 2p and (d) Cu 2p of Cu-Co-MOF-74 and Cu-Co-MOF-74-After catalysis.

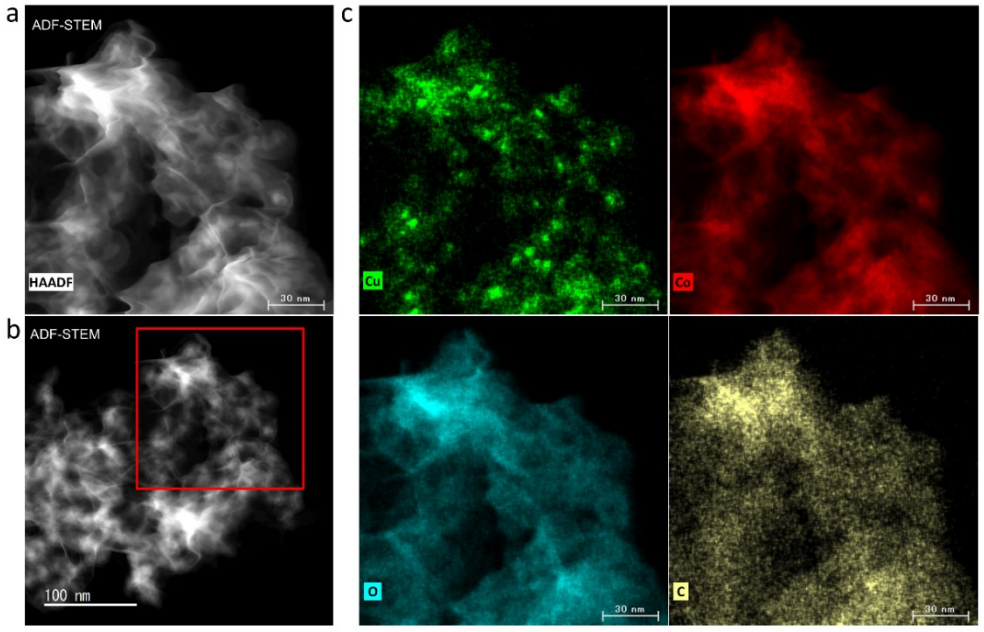

Figure 4.9 (a) and (b) HAADF-STEM, and (c) elemental mapping images of Cu-Co-MOF-74 after catalytic hydrogen evolution from ammonia borane. (Mo TEM support grids used).

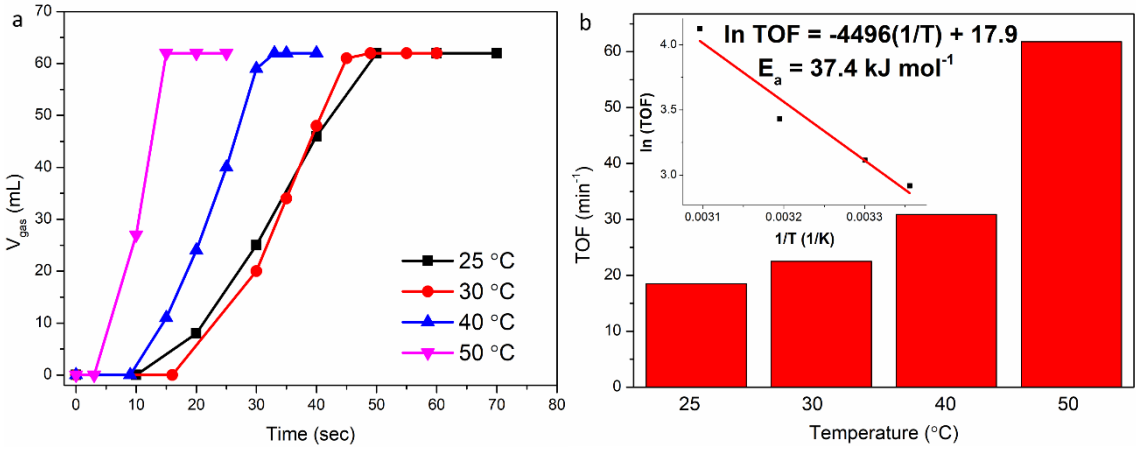

Figure 4.10 (a) Temperature dependence of gas evolution from AB over Cu-Co-MOF-74, and the corresponding TOF values (Inset in (b) is Arrhenius plot (lnTOF) *vs.* 1/T)) (n_{Co} = 0.204 mmol, n_{Cu} = 0.005 mmol, n_{AB} = 1 mmol).

Similar as other catalysts, the catalytic activity of Cu-Co-MOF-74 greatly depends on the reaction temperature. AB dehydrogenations at different temperatures were operated and the results are shown in Figure 4.10. TOF values were calculated based on the total reaction time subtracted with reduction time of catalysts and the total amount of Cu and Co. With the increase of temperature, the catalytic activity was improved dramatically and according to Arrhenius plot and an activation energy of 37.4 kJ mol^{-1} was obtained.

Usually MOF-derived metal/metal oxides were synthesized by thermolysis which is totally different to our work. Therefore, for comparison, we also prepared Cu-Co-MOF-74-*T* (*T* stands for temperature, °C) as catalysts for AB decomposition. Thermogravimetric analysis (TG) was employed, and based on the TG curve (Figure 4.11), typical samples carbonized at 200, 350 and 650 °C were prepared.

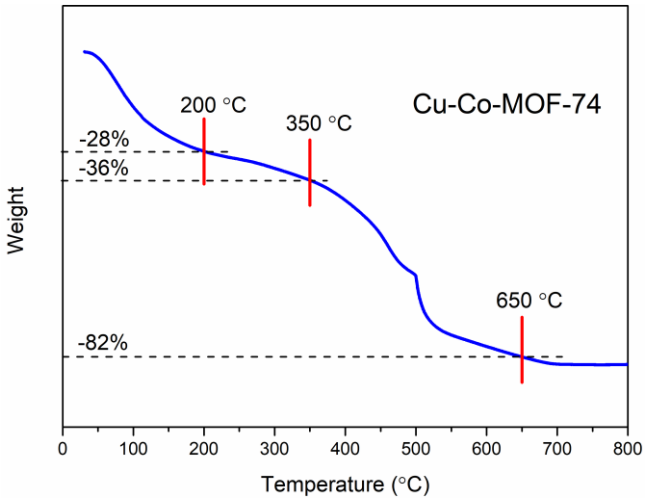

Figure 4.11. TG curve for Cu-Co-MOF-74 (with a heating rate of 10 °C/min from room temperature to 800°C under Ar atmosphere).

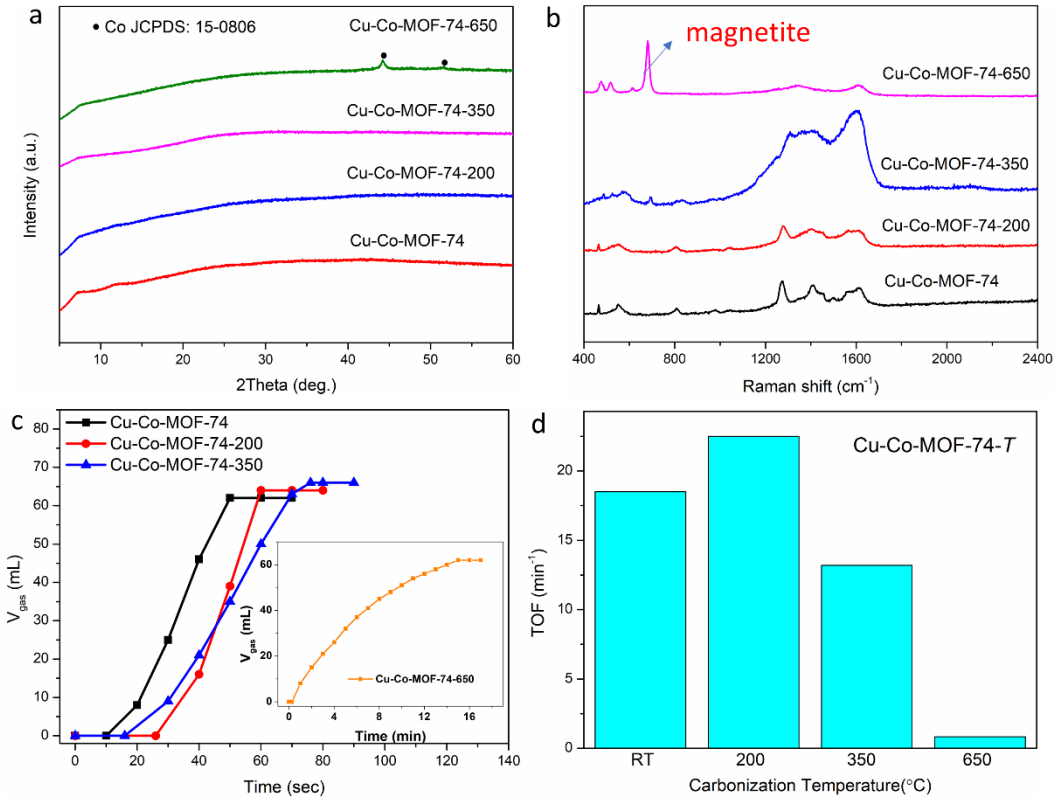

Figure 4.12. (a) XRD patterns, (b) Raman spectra, (c) gas evolution from aqueous AB and (d) the corresponding TOF values of Cu-Co-MOF-74-*T* catalysts (25 °C, n_{Co} = 0.204 mmol, n_{Cu} = 0.005 mmol, n_{AB} = 1 mmol).

The XRD patterns (Figure 4.12a) and Raman spectra (Figure 4.12b) show that when

temperature reached 350 °C, Cu-Co-MOF-74 start to break down. When it reached 650 °C, peaks of Co appeared in the XRD pattern and the Raman spectrum also show a typical peak at 680 cm^{-1} for magnetite. Their hydrogen evolutions from aqueous AB show that when temperature reached 350 °C, the catalytic activity decreased in some extent and when temperature reached 650 °C, the catalysts shows very poor activity (Figure 4.12c and d). The catalytic activities did not decrease when under thermolysis below 200 °C. This result suggest the advantage of direct in-situ reduction of bimetallic MOFs for AB dehydrogenation.

For comparison, we also investigate series of related catalysts including Co-MOF-74, Cu-MOF-74 and Cu-Co-MOF-74-MB. We further prepared Cu@MOF-74 samples using double solvents method (DSM) (Figure 4.5b). XRD patterns of all the samples are similar (Figure 4.13a).The catalytic results were shown in Figure 4.13b and obviously, the Cu-Co-MOF-74 possess unparalleled activity for AB dehydrogenation. Single metallic MOF-74 counterparts show poor activities, implying the strong interaction between Cu and CoOx in Cu-Co-MOF-74. Cu-Co-MOF-74-MB also shows a poor activity due to its solid micro-block structure which is hard to contact with the reactant. Even Cu@Co-MOF-74 is not as active as Cu-Co-MOF-74, suggesting that the uniform dispersion of Cu in bimetallic MOF-74 results in the highly-dispersed Cu component facilitating the catalytic process. After catalysis, the XRD pattern of the catalyst (Figure 4.14) showed no obvious peak of metals, meeting with the small sizes of the formed metal NPs observed by TEM measurement.

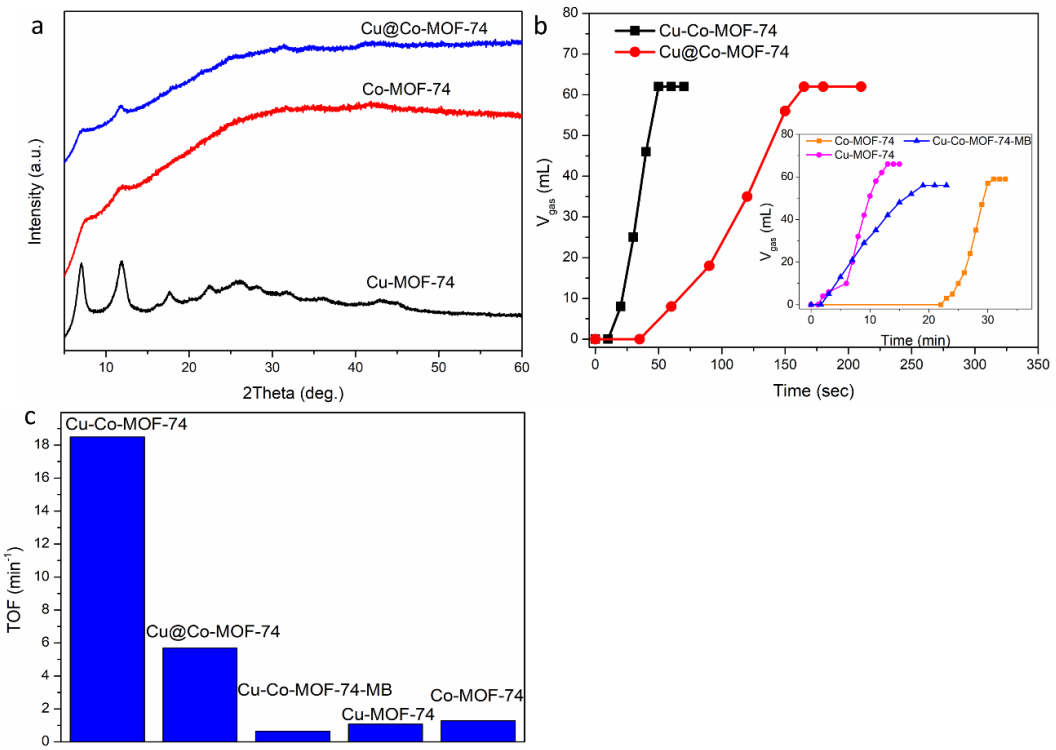

Figure 4.13. (a) XRD patterns，(b) hydrogen evolution and (c) the corresponding TOF values of different MOFs and MOF-composite (25 °C, n_{Co} = 0.204 mmol, n_{Cu} = 0.005 mmol, n_{AB} = 1 mmol).

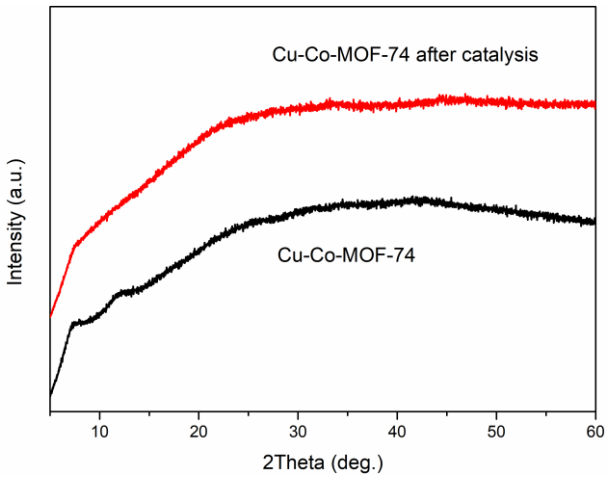

Figure 4.14. XRD patterns of Cu-Co-MOF-74 before and after catalysis (25 °C, n_{Co} = 0.204 mmol, n_{Cu} = 0.005 mmol, n_{AB} = 1 mmol).

4.4 Conclusion

In summary, for the first time, a bimetallic Cu-Co-MOF-74 was prepared and used as catalyst for AB dehydrogenation through an in-situ reduction. The catalyst shows a TOF value of 18.5 min^{-1} and a good durability for 5 cycles at 25 ℃. Compared with traditional thermolysis process, this in-situ reduction of bimetallic MOF is simple and the catalytic activity is prospective. Considering the diversification of MOFs, this work gives a possibility of tailoring MOFs for specific functional metal/metal oxides in area of energy storage and conversion.

References

1. (a) Dunn, S., *Int. J. Hydrogen Energy* **2002,** *27*, 235-264; (b) Momirlan, M.; Veziroglu, T., *Renewable Sustainable Energy Rev.* **2002,** *6*, 141-179; (c) Turner, J. A., *Science* **2004,** *305*, 972-974; (d) Momirlan, M.; Veziroglu, T. N., *Int. J. Hydrogen Energy* **2005,** *30*, 795-802.

2. (a) Züttel, A., *Mater. Today* **2003,** *6*, 24-33; (b) Biniwale, R. B.; Rayalu, S.; Devotta, S.; Ichikawa, M., *Int. J. Hydrogen Energy* **2008,** *33*, 360-365; (c) Yadav, M.; Xu, Q., *Energy Environ. Sci.* **2012,** *5*, 9698-9725.

3. (a) Stephens, F. H.; Pons, V.; Baker, R. T., *Dalton Trans.* **2007,** *25*, 2613-2626; (b) Peng, B.; Chen, J., *Energy Environ. Sci.* **2008,** *1*, 479-483; (c) Hamilton, C. W.; Baker, R. T.; Staubitz, A.; Manners, I., *Chem. Soc. Rev.* **2009,** *38*, 279-293; (d) Lan, R.; Irvine, J. T.; Tao, S., *Int. J. Hydrogen Energy* **2012,** *37*, 1482-1494.

4. (a) Durap, F.; Zahmakıran, M.; Özkar, S., *Appl. Catal., A* **2009,** *369*, 53-59; (b) Xi, P.; Chen, F.; Xie, G.; Ma, C.; Liu, H.; Shao, C.; Wang, J.; Xu, Z.; Xu, X.; Zeng, Z., *Nanoscale* **2012,** *4*, 5597-5601; (c) Chen, W.; Ji, J.; Duan, X.; Qian, G.; Li, P.; Zhou, X.; Chen, D.;

Yuan, W., *Chem. Commun.* **2014,** *50*, 2142-2144; (d) Yao, Q.; Shi, W.; Feng, G.; Lu, Z.-H.; Zhang, X.; Tao, D.; Kong, D.; Chen, X., *J. Power Sources* **2014,** *257*, 293-299; (e) Zhan, W.-W.; Zhu, Q.-L.; Xu, Q., *ACS Catal.* **2016,** *6*, 6892-6905.

5. (a) Keaton, R. J.; Blacquiere, J. M.; Baker, R. T., *J. Am. Chem. Soc.* **2007,** *129*, 1844-1845; (b) Yan, J. M.; Zhang, X. B.; Han, S.; Shioyama, H.; Xu, Q., *Angew. Chem., Int. Ed.* **2008,** *47*, 2287-2289; (c) Yan, J.-M.; Zhang, X.-B.; Shioyama, H.; Xu, Q., *J. Power Sources* **2010,** *195*, 1091-1094; (d) Yang, Y.; Lu, Z.-H.; Hu, Y.; Zhang, Z.; Shi, W.; Chen, X.; Wang, T., *RSC Adv.* **2014,** *4*, 13749-13752.

6. (a) Yang, S. J.; Kim, T.; Im, J. H.; Kim, Y. S.; Lee, K.; Jung, H.; Park, C. R., *Chem. Mater.* **2012,** *24*, 464-470; (b) Chaikittisilp, W.; Ariga, K.; Yamauchi, Y., *J. Mater. Chem. A* **2013,** *1*, 14-19; (c) Shen, K.; Chen, X.; Chen, J.; Li, Y., *ACS Catal.* **2016,** *6*, 5887-5903; (d) Tang, J.; Yamauchi, Y., *Nat. Chem.* **2016,** *8*, 638.

7. (a) Aijaz, A.; Karkamkar, A.; Choi, Y. J.; Tsumori, N.; Rönnebro, E.; Autrey, T.; Shioyama, H.; Xu, Q., *J. Am. Chem. Soc.* **2012,** *134*, 13926-13929; (b) Wang, C.; DeKrafft, K. E.; Lin, W., *J. Am. Chem. Soc.* **2012,** *134*, 7211-7214; (c) Du, N.; Wang, C.; Long, R.; Xiong, Y., *Nano Res.* **2017,** *10*, 3228-3237; (d) Song, F. Z.; Zhu, Q. L.; Yang, X.; Zhan, W. W.; Pachfule, P.; Tsumori, N.; Xu, Q., *Adv. Energy Mater.* **2018,** *8*, 1770139.

8. (a) Zheng, F.; Yin, Z.; Xia, H.; Zhang, Y., *Mater. Lett.* **2017,** *197*, 188-191; (b) Liu, S.; Deng, T.; Hu, X.; Shi, X.; Wang, H.; Qin, T.; Zhang, X.; Qi, J.; Zhang, W.; Zheng, W., *Electrochim. Acta* **2018,** *289*, 319-323; (c) Ma, Y.; He, J.; Kou, Z.; Elshahawy, A. M.; Hu, Y.; Guan, C.; Li, X.; Wang, J., *Adv. Mater. Interfaces* **2018,** *5*, 1800222.

9. Chandra, M.; Xu, Q., *J. Power Sources* **2006,** *156*, 190-194.

Chapter 5

Conclusion

MOF-derived materials have been widely used as supports or precusors in syntheses of catalysts. The purpose of this dissertation is to prepare active MNPs based on MOF-derived materials for efficent catalytic hydrogen generation from liquid-phase chemical hydrogen storage materials such as formic acid and aqueous ammonia borane. Ultrafine Pd NPs was firstly immobilzed on activated hierarchically porous carbon derived from a nitrogen containing MOF for fast dehydrogenation of formic acid. Then highly active AuPd NPs were immobilized on a N-doped carbon from MOF with a phosphate-mediation approach for boosting hydrogen evolution from formic acid at room temperature. Finally, non-noble Cu decorated CoOx NPs from bimetallic MOFs were prepared by a direct in-situ reduction for hydrogen evolution from aqueous AB. The main reasearch results of this disseration are summarized as follows:

(i) Fast Dehydrogenation of Formic Acid over Palladium Nanoparticles Immobilized in Nitrogen-Doped Hierarchically Porous Carbon

A hierarchically porous carbon was prepared from Al-MIL-101-NH_2 via carbonization, followed by activation under ultrasonication in aq. KOH. Highly dispersed ultrafine Pd NPs (1.1 ± 0.2 nm) have been successfully synthesized. By virtue of ultrafine Pd NPs, efficient mass transport brought by rich mesoporosity and the synergistic effect between the doped N in the support and the Pd NPs, the catalyst (Pd@CN900K) exhibits an extremely high catalytic activity with a TOF value of 14400 h^{-1} (60 °C), a good durability and a 100 % H_2 selectivity for dehydrogenation

of FA. This activation approach of carbon opens an avenue for the syntheses of highly active supported ultrafine MNPs for catalysis.

(ii) Phosphate-Mediated Immobilization of High-Performance AuPd Nanoparticles for Dehydrogenation of Formic Acid at Room Temperature

A high-performance AuPd nanocatalyst has been synthesized via a phosphate-mediation approach which provides strong interactions with metal ions and results in the formation of well-dispersed ultrafine AuPd NPs. The as-synthesized Au_2Pd_3@(P)N-C exhibits an extremely high catalytic activity for FA dehydrogenation at low temperatures, showing a TOF value as high as 5400 h^{-1} at 30 °C and 1964 h^{-1} at 10 °C. The phosphate-mediation approach, especially combined with simultaneous N doping in carbons, is an effective methodology for preparation of highly active AuPd NPs. This work opens a new avenue to synthesize highly efficient metal nanocatalysts for applications in various catalytic fields.

(iii) Copper Decorated Cobalt Oxides Nanoparticles from Bimetallic MOF-74 for Dehydrogenation of Ammonia Borane

A bimetallic Cu-Co-MOF-74 was prepared and used as catalyst for AB dehydrogenation through an in-situ reduction. The catalyst shows a TOF value of 18.5 min^{-1} and a good durability for 5 cycles at 25 ℃. Compared with traditional thermolysis process, this in-situ reduction of bimetallic MOF is simple and the catalytic activity is prospective. Considering the diversification of MOFs, this work gives a possibility of tailoring MOFs for specific functional metal/metal oxides in area of storage and conversion.

In summary, this dissertation focuses on the syntheses of active ultrafine MNPs by taking advantage of MOF-derived materials, whose applications in hydrogen

evolution from liquid-phase chemical hydrogen storage materials are promising for future fuel cell industry. The method of post-functionalization of MOF-derived carbons and the direct in-situ reduction strategy of MOFs to specific metal/metal oxides mentioned in this dissertation may inspire researchers to investigate the potential of MOFs in use of energy storage and conversion.

List of publications

Journal Publications

1. Fast Dehydrogenation of Formic Acid over Palladium Nanoparticles Immobilized in Nitrogen-Doped Hierarchically Porous Carbon.

   Qiuju Wang, Nobuko Tsumori, Mitsunori Kitta and Qiang Xu*

   ACS Catalysis, **2018**, *8*, 12041-12045.

2. Phosphate-Mediated Immobilization of High-Performance AuPd Nanoparticles for Dehydrogenation of Formic Acid at Room Temperature

   Qiuju Wang, Liyu Chen, Zheng Liu, Nobuko Tsumori, Mitsunori Kitta and Qiang Xu*

   Accepted by *Advanced Functional Materials*.

3. Copper Decorated Cobalt Oxide Nanoparticles from Bimetallic MOF-74 for Dehydrogenation of Ammonia Borane

   Qiuju Wang, Noboru Taguchi and Qiang Xu*

   In preparation.

Doctoral Dissertation, Kobe University
"Study of Metal Nanoparticle Catalysts for High-Performance Hydrogen Generation from Chemical Hydrides", 98 pages
Submitted on July, 19th, 2019
The date of publication is printed in cover of repository version published in Kobe University Repository Kernel.